




8-2021

Experimental and computational study of determining mass transport parameters in vanadium redox flow batteries

Tugrul Y. Ertugrul

University of Tennessee, Knoxville, tertugru@vols.utk.edu

Follow this and additional works at: https://trace.tennessee.edu/utk_graddiss

 Part of the [Energy Systems Commons](#), [Other Mechanical Engineering Commons](#), and the [Transport Phenomena Commons](#)

Recommended Citation

Ertugrul, Tugrul Y., "Experimental and computational study of determining mass transport parameters in vanadium redox flow batteries. " PhD diss., University of Tennessee, 2021.
https://trace.tennessee.edu/utk_graddiss/6510

This Dissertation is brought to you for free and open access by the Graduate School at TRACE: Tennessee Research and Creative Exchange. It has been accepted for inclusion in Doctoral Dissertations by an authorized administrator of TRACE: Tennessee Research and Creative Exchange. For more information, please contact trace@utk.edu.

To the Graduate Council:

I am submitting herewith a dissertation written by Tugrul Y. Ertugrul entitled "Experimental and computational study of determining mass transport parameters in vanadium redox flow batteries." I have examined the final electronic copy of this dissertation for form and content and recommend that it be accepted in partial fulfillment of the requirements for the degree of Doctor of Philosophy, with a major in Mechanical Engineering.

Matthew M. Mench, Major Professor

We have read this dissertation and recommend its acceptance:

Kenneth Kihm, Feng Y. Zhang, David Keffer, Douglas Aaron

Accepted for the Council:

Dixie L. Thompson

Vice Provost and Dean of the Graduate School

(Original signatures are on file with official student records.)

**Experimental and computational study of determining mass transport
parameters in vanadium redox flow batteries**

**A Dissertation Presented for the
Doctor of Philosophy
Degree
The University of Tennessee, Knoxville**

**Tugrul Yavuz Ertugrul
August 2021**

Copyright © 2021 by Tugrul Yavuz Ertugrul
All rights reserved.

DEDICATION

To my mother, for instilling a love of reading and learning from my early age.
To my father, for teaching me honesty, integrity, and fairness.
To my sister, for supporting and encouraging me all the time.

ACKNOWLEDGEMENTS

Throughout my graduate studies and the writing of this dissertation I have received a great deal of support and assistance.

First, I would like to express my sincere gratitude to my advisor, Dr. Matthew Mench for his mentoring and continued support of my PhD study. I am thankful for his patience and flexibility that allows me to pursue research that I find interesting. The research environment he created and the opportunities he provided at the University of Tennessee have made my graduate studies pleasant and enjoyable academic experience.

I cannot begin to express my thanks to Dr. Doug Aaron who provided exceptional guidance and assistance throughout the duration of this journey. I am truly grateful for his invaluable contribution to the research in this dissertation. I learned a lot from his constructive feedback and ingenious suggestions. I really enjoyed talking science and having fruitful research discussions with him.

Many thanks to my lab mates both past and present in the Electrochemical Energy Storage and Conversion Laboratory. It was a great pleasure working with such a brilliant group of engineers and scientists. Special thanks to Jason Clement for teaching me in-situ current distribution diagnostic and machining as well as giving me guidance and advice in my early graduate career. Thanks should also go to Michael Cyrus Daugherty for helping me to improve my programming skills and giving invaluable insight into my mathematical modelling efforts throughout the course of my PhD. Working alongside him has truly been a pleasure.

I would like to thank Dr. Kenneth Kihm, Dr. Feng-Yuan Zhang, Dr. David Keffer, and Dr. Doug Aaron for serving on my dissertation committee and for their helpful comments and suggestions.

I would like to acknowledge the Ministry of Education of Turkey for financially supporting and the University of Tennessee for providing Chancellor's Graduate Fellowship support.

I reserve a special thanks to my parents, Talip and Ayse Ertugrul and my sister, Tuba Ertugrul. Words cannot express my gratitude for their unwavering love, patience, encouragement, and support through the years.

ABSTRACT

Vanadium redox flow batteries are a promising large-scale energy storage technology, but a number of challenges must be overcome for commercial implementation. At the cell level, mass transport contributes significantly to performance losses, limiting VRFB performance. Therefore, understanding mass transport mechanisms in the electrode is a critical step to mitigating such losses and optimizing VRFBs.

In this study, mass transport mechanisms (e.g. convection, diffusion) are investigated in a VRFB test bed using a strip cell architecture, having 1 cm² active area. It is found that diffusion-dominated cells have large current gradients; convection-dominated cells have relatively uniform current distribution from inlet to outlet under a mass transport limited condition. This behavior is attributed to convective mass transport in the electrode.

Computational flow simulation is utilized to assess velocity and pressure distributions; experimentally measured in-situ current distribution is quantified for the cell. CFD simulation has shown that the total current in the cell is directly proportional to electrolyte velocity in the electrode. However, maximum achievable current is limited by diffusion mass transport resistance between the liquid electrolyte and the electrode surfaces. The pressure drop arising due to any fluid path outside the channel-electrode region is found to be ineffective and must be minimized to improve overall system efficiency of the VRFB.

A three-dimensional, steady-state multiphysics model for VRFB strip cell architecture is further developed to investigate mass transport more fundamentally. Numerical predictions are validated by experimental measurements (polarization curve and current distribution). Diffusion coefficient of the vanadium active species and electrode

permeability are found to be the most important parameters affecting electrochemical performance and performance distribution.

Carbon paper electrode permeability is investigated both computationally and experimentally. While three-dimensional pore-level Lattice Boltzmann model is adopted to predict electrode permeability, a permeability cell experimental setup is designed to measure carbon paper electrode permeability under different compressions. It is found that permeability is directly proportional to the electrode porosity. While a simulated solid domain considering only the fibers does not predict experimentally measured permeabilities for higher electrode porosities, a composite domain considering both fibers and filler material successfully simulates carbon paper electrode macropore structure.

TABLE OF CONTENTS

Chapter 1 Introduction	1
1.1 Motivation.....	2
1.2 Mass transport in vanadium redox flow battery	2
1.3 In-situ localized current distribution measurements	4
1.4 VRFB mathematical models.....	5
1.4.1 Lattice Boltzmann model.....	6
1.4.2 Cell level modelling.....	7
1.5 Objectives	9
Chapter 2 In-Situ Current Distribution and Mass Transport Analysis via Strip Cell Architecture for a Vanadium Redox Flow Battery	11
Abstract.....	12
2.1 Introduction.....	13
2.2 Materials and methods	14
2.2.1 Experimental setup and strip cell architecture	14
2.2.2 Electrolyte solution preparation.....	15
2.2.3 Polarization curves and in-situ localized current distribution measurements..	17
2.2.4 Crossover measurements	17
2.2.5 Pressure drop measurements.....	18
2.3 Results and discussions.....	19
2.5 Conclusions.....	33
Chapter 3 Computational and Experimental Study of Convection in a Vanadium Redox Flow Battery Strip Cell Architecture	35
Abstract.....	36
3.1 Introduction.....	37
3.2 Materials and methods	38
3.2.1 Polarization curves and in-situ current distribution measurements	39
3.2.2 Computational fluid dynamics.....	40
3.2.3 Power analysis	43
3.3 Results and discussion	43
3.4 Conclusions.....	61
Chapter 4 Vanadium Flow Battery Electrochemistry and Fluid Dynamics Model in-situ Current Distribution Validation	63
Abstract.....	64
4.1 Introduction.....	64
4.2 Materials and methods	65
4.2.1 Experimental	65
4.2.2 Multiphysics model.....	65
4.3 Results and discussion	70
4.4 Conclusions.....	78
Chapter 5 In-plane Liquid Electrolyte Permeability of Porous Electrode in Vanadium Flow Battery.....	81
Abstract.....	82

5.1 Introduction.....	82
5.2 Materials and methods	83
5.2.1 Lattice Boltzmann model (LBM).....	83
5.2.2 In-plane permeability experimental setup.....	87
5.3 Results and discussion	93
5.4 Conclusions.....	100
Chapter 6 Conclusion and recommendations	102
6.1 Conclusions.....	103
6.2 Intellectual merit and broader impacts of the work	106
6.3 Recommendations.....	108
References.....	110
VITA.....	122

LIST OF TABLES

Table 2.1 Summary of operating conditions.....	32
Table 3.1 Simulation parameters	42
Table 3.2 Selected parameters for the range of channel depths and flow rates considered in this work. Limiting current is the current achieved at 0.2 V discharge for a 50% SOC electrolyte.....	50
Table 3.3 Calculated pump power input and cell power output for all strip cell configurations.	59
Table 4.1 Geometric, material, and kinetic properties.....	74
Table 4.2 Electrolyte properties.....	75
Table 5.1 Electrode thicknesses during compression and corresponding porosities	90

LIST OF FIGURES

Figure 2.1 Exploded view of VRFB strip cell (a) and (b) strip cell segmented flow plate.	16
Figure 2.2 Experimentally-measured crossover for four different channel depths.	20
Figure 2.3 Polarization curves for all channel depths at 50% SOC, 30 mL min ⁻¹	22
Figure 2.4 Normalized current distributions for various points on the polarization curve at 50% SOC, 30mL min ⁻¹ for channel depths (a) 2.50 mm (b) 1 mm (c) 0.5 mm (d) 0.25 mm.	23
Figure 2.5 Normalized current (a) and (b) local current distribution comparisons for four different depth channels at 50% SOC, 30 mL min ⁻¹ , 0.2 V hold.....	25
Figure 2.6 Experimentally-measured pressure drop data for four different channel depths.	27
Figure 2.7 Impact of flow rate on the local current at 50% SOC, 0.2 V hold (a) and (b) for 2.5 mm and 1mm depth channels, respectively; (c) and (d) normalized current distributions for 2.5 mm and 1 mm depth channels, respectively.	29
Figure 2.8 Impact of flow rate on the local current at 50% SOC 0.2V hold (a) and (b) 0.5mm and 0.25 mm depth channels, respectively; (c) and (d) normalized current distributions for 0.5 mm and 0.25 mm depth channels, respectively.	30
Figure 3.1 Simulation domains with channel and electrode [3]	41
Figure 3.2 Computationally predicted and experimentally measured pressure drops through the strip cell, including inlet and outlet manifold pipes. Error bars reflect both pulsing from the peristaltic pump and experimental variability.	45
Figure 3.3 Predicted electrolyte velocity distribution at a cut line in the center of the electrode and channel domain (a) 2.5 mm (b) 1 mm (c) 0.50 mm (d) 0.25 mm and (e) correlation between average channel velocity and measured limiting currents. .	46
Figure 3.4 Magnified view of predicted electrolyte velocity distribution in the electrode (a) 2.50 mm (b) 1.00 mm (c) 0.50 mm (d) 0.25 mm and (e) correlation between average electrode velocity and measured limiting currents.....	49
Figure 3.5 Measured local current (a) and (b) normalized current distribution comparisons at 50% SOC, 30mL/min, 0.2V hold.	52
Figure 3.6 Predicted electrolyte velocity distribution at a cut plane through the electrode domain for all channel depths at 30 ml min ⁻¹ flow rate.	53
Figure 3.7 Predicted pressure drop distribution for (a) complex and (b) simplified geometries.	56
Figure 3.8 Correlations between (a) local pressure drop and average channel velocity (b) Cell power output and pump power input comparison for all strip cell configurations.	58
Figure 3.9 Correlations between (a) local pressure drop and average electrode velocity (b) average local pressure drop and limiting current (c) overall pressure drop and limiting current.....	60
Figure 4.1 Simulation domains with channels, electrodes, and membrane	67
Figure 4.2 The comparison of experimentally measured and computationally predicted open circuit voltage (OCV) for	71

Figure 4.3 Experimentally measured and computationally predicted Polarization curves for 1 mm depth channel strip cell configuration at 50% SOC and 30 mL min ⁻¹ flow rate.....	73
Figure 4.4 Electrode permeability parameter impact on computationally predicted (a) Polarization curves and (b) current distributions for 1 mm depth channel strip cell configuration at 50% SOC and 30 mL min ⁻¹ flow rate.....	77
Figure 4.5 Diffusion coefficient of vanadium active species' impact on computationally predicted (a) Polarization curves and (b) current distributions for 1 mm depth channel strip cell configuration at 50% SOC and 30 mL min ⁻¹ flow rate.....	79
Figure 5.1 Carbon paper electrode macropore structure artificially generated in Python (a) r =2 lu, Number of cylinders = 188, (b) r = 3 lu, Number of cylinders = 76, (c) r = 4 lu, Number of cylinders = 39, (d) r = 5 lu, Number of cylinders = 27	84
Figure 5.2 Randomly-generated carbon paper macropore structures with different porosities (a) 89% porosity, (b) 82.7 % porosity, (c) 69.7 % porosity.	85
Figure 5.3 D3Q19 x, y, and z velocity components.....	88
Figure 5.4 Exploded view of in-plane permeability measurement experimental setup....	91
Figure 5.5 An image of carbon paper electrode macropore structure under optical microscope	92
Figure 5.6 Pressure drop per length as a function of flow rate for various carbon paper electrode porosities showing experimental data and fitting using the Darcy's equation.....	94
Figure 5.7 Experimentally measured permeabilities vs. Computationally predicted permeabilities as a function porosity for various fiber radiuses.	95
Figure 5.8 Experimentally measured permeabilities vs. Computationally predicted permeabilities as a function porosity for various lattice resolutions.....	97
Figure 5.9 (a) An image of carbon paper electrode macropore structure under optical microscope and randomly generated composite domain (b) 70% fiber, 30% filler (c) 50% fiber, 50% filler (d) 30% fiber, 70% filler.....	98
Figure 5.10 Experimentally measured permeabilities vs. Computationally predicted permeabilities as a function porosity for various composite domains.....	99

Chapter 1 Introduction

This chapter is revised based on the published papers and proceedings [1–4]

Ertugrul, T. Y., Clement, J. T., Gandomi, Y. A., Aaron, D. S., and Mench, M. M. “**In-Situ Current Distribution and Mass Transport Analysis via Strip Cell Architecture for a Vanadium Redox Flow Battery**” *Journal of Power Sources* 437, (2019): 226920. doi:10.1016/j.jpowsour.2019.226920

Ertugrul, T. Y., Clement, J. T., Gandomi, Y. A., and Aaron, D. “**Isolation of Mass Transport and Current Distribution in Vanadium Flow Batteries Via Segmented Strip Cell**” *ECS Meeting Abstracts* (2019): 10–13. doi:10.1149/ma201

Ertugrul, T. Y., Daugherty, M. C., Houser, J. R., Aaron, D. S., and Mench, M. M. “**Computational and Experimental Study of Convection in a Vanadium Redox Flow Battery Strip Cell Architecture**” *Energies* 13, no. 18 (2020): 4767. doi:10.3390/en13184767

T.Y. Ertugrul, J.R. Houser, M.C. Daugherty, D.S. Aaron and M.M. Mench. “**Understanding the Interplay between Electrolyte Velocity Distribution and Current Distribution in Vanadium Flow Battery Electrode**” *ECS Meeting Abstracts* (2019): doi:10.1149/ma2019-02/1/14

1.1 Motivation

The National Renewable Energy Laboratory (NREL) estimates that renewable energy sources (solar, wind power and hydropower) could be responsible of 70%-75% total electricity generation in the United States by 2050 [5]. Due to the intermittent nature of renewable energies, large-scale energy storage technologies are indispensable for high penetration of variable electricity generation to the power grid. Energy storage technologies can address several challenges: electricity service stability, flexibility, reliability, and resilience on the power grid. Among energy storage systems, vanadium redox flow batteries (VRFBs) have been pursued due to their flexibility and scalability, high coulombic efficiency, and long cycle life. However, widespread commercialization of VRFBs suffers from high system capital cost. The US Department of Energy (DOE) proposed a target system capital cost under 150 \$/kWh for commercialization of energy storage systems [6]. To achieve this goal, VRFB cell component costs (membranes and chemicals), which dominate overall system costs, need to be reduced [7,8]. Improving electrolyte utilization and overall system efficiency are the most viable approaches to reduce overall system costs. Recent efforts include increasing solubility of the four vanadium species in the solvent [9–12], enhancing separators to be more ionically conductive, alleviating crossover [13–21], facilitating electrochemical kinetics [22–25], improving mass transport, and reducing parasitic pump losses [26–29].

1.2 Mass transport in vanadium redox flow battery

In VRFB cells, transport of active species to/from electrode reaction surfaces is critically important. Insufficient active species transport leads to concentration

overpotential, also known as mass transport polarization, due to reactant depletion and/or product accumulation at electrode surfaces. Increased overpotential results in decreased voltage efficiency, reduced accessible state of charge (SOC), and reduced effective energy capacity of the battery. One of the most straightforward approaches to mitigate mass transport losses is increasing vanadium concentration in the solvent. It has been shown that vanadium concentration in the solvent can be increased (maximum 3 M vanadium electrolyte was achieved) by using mixed acid solution [9] and additives [10]. Despite these improvements, vanadium species solubility in the solvent is still limited compared to organic systems [30]. Increasing flow rate is another simple approach frequently found to enhance convective mass transport in the electrode [31–36]. However, due to parasitic pumping losses, increasing the flow rate becomes an optimization problem highly sensitive to other system parameters. Common flow field designs, including flow-through (aspect ratio and equal path length) and flow-by (e.g. parallel, interdigitated and serpentine) have been widely investigated in VRFB literature [26,27,37–45]. It has been also reported that channel geometry (channel height, channel width, channel length, and land or rib width) influences electrochemical performance [40,43,46,47]. In addition to flow field impacts, the electrode is one of the most critical components since electrochemical reactions occur on the electrode surface. Many studies have attempted to improve ion transport by modifying electrode structure (thickness, porosity, and tortuosity) [39,48–52]. However, there is a sensitive balance between permeability and electrochemical surface area in the electrode; in general, higher permeability is achieved at the cost of reduced active surface

area. Thus, optimization in VRFBs is not straightforward. Such optimization requires localized, real-time information within the cell.

1.3 In-situ localized current distribution measurements

In-plane current measurement is a diagnostic technique that has been used for fuel cells [53] and then adapted to VRFBs [54]. This technique assesses distributed cell performance by discretizing cell current into in-plane segments. Electronic insulation must persist through cell components: flow plates, and current collectors. Overall cell performance can be evaluated by monitoring each segment's current. Several approaches have been developed and implemented to measure localized current in electrochemical cells: resistor networks [55–57], potential probes [58], and the printed circuit board (PCB) [54,59,60] have all been demonstrated successfully. The PCB technique is employed in this study due to the high spatial resolution and adaptability to different flow plate designs.

The PCB technique is pioneered in fuel cells [53] and then adapted to VRFBs [54]. The basic premise of this technique relies on measuring voltage drop across shunt resistors in each segment. Via Ohm's law, corresponding currents can be calculated. The PCB technique does require segmentation of current collectors and flow fields. Segmentation electronically isolates segments for corresponding current/voltage collection. Recent studies have shown that employing both segmented current collectors and flow fields is essential for accuracy of the current measurement [54,57]. Partially segmented or unsegmented flow components allow significant lateral current spread. This phenomenon is demonstrated both experimentally [61] and computationally [62]. Some studies attempted electrode segmentation due to current spread [63]. Since this approach would

disturb the true current density distribution that occurs in operating systems and current spread in the electrode is minimal, it is rarely employed.

Clement et al. employed in-plane current distribution measurement to investigate mass transport for a range of cell and operating parameters [61]. Houser and co-workers revealed contributions from the two dominating mass transport mechanisms by comparing current distributions for interdigitated and serpentine flow field designs [26]. In published work [1,4], we implemented current distribution measurement for a single channel (“strip cell”) architecture to isolate diffusion and convection mass transport mechanisms. Enhanced electrochemical performance and relatively uniform current density distribution were attributed to increased convective flow in the porous electrode [3]. However, the VRFB is a complex system with multiple interrelated parameters (e.g. mass transport and electrochemical reactions) affecting electrochemical cell performance; experimentally disentangling these interrelated parameters is very challenging. Additionally, while experimental investigation often provides quantitative measurements of VRFB behavior, it is relatively costly, slow, and limited by available equipment. Computational analysis through first-principles-based modeling is a complementary approach with unique benefits discussed in the following paragraphs. Thus, a comprehensive and properly validated computational simulation is essential to understand physicochemical processes in VRFBs.

1.4 VRFB mathematical models

Mathematical modeling efforts have been reported for mature electrochemical devices like fuel cells and lithium-ion batteries. Although VRFBs are an emerging new technology, a variety of modeling efforts have already been reported. Zheng et al. [64]

reviewed mathematical models for VRFBs in terms of two categories: spatial scale (macro, micro, and molecular/atomic efforts) and topical focus (economics, stack/system behavior, individual cells, and material properties). Cost modeling, stack/system phenomena, and cell modeling are typically approached at the macroscale. Monte Carlo (MC) and equivalent circuit modeling are common macroscale approaches utilized for cost and VRFB stack/system modeling, respectively. Microscale models describe phenomena occurring at the transition between macro- and molecular/atomic scales; cell and material property modeling are examples of this category. Molecular/atomic approaches are designed to simulate physicochemical phenomena at a fundamental level. The most popular molecular/atomic approach is Lattice Boltzmann model (LBM) [65].

1.4.1 Lattice Boltzmann model

Lattice Boltzmann models (LBMs) are a class of numerical methods which can be used to simulate fluid flows, mass transfer, heat transfer and many relevant physical phenomena which occur in these fields. LBM is an explicit method based on the lattice gas automata (LGA). Unlike the conventional numerical methods which solve conservation equations, LBM simulates microscopic particle distribution in the flow domain. The governing equation for the LBM is derived from the Boltzmann transport equation discretizing velocity, space, and time. Depending on the discretized domain (1D, 2D, 3D) and desired accuracy, different discrete velocity sets (D1Q3, D2Q9, D3Q15, D3Q19 and D3Q27) are employed. One of the most prominent advantages of LBM is the ease of implementing boundary conditions to complex systems such as porous media [66]. The Bounce-back boundary condition which is the most popular boundary condition represents

no-slip boundary condition is the in LBM. Periodic boundary condition is the simplest boundary condition used for open ends or infinite domains. While the Dirichlet boundary condition constrains a density/pressure, the Von-Neumann boundary condition imposes a flux at the boundary. Lattice Boltzmann equation consists of two steps: streaming (propagation) and collision (relaxation). In the first step, particles move to the neighboring positions from their initial positions. Next, they collide according to the chosen collision operator. These steps are completed in a one-step time. Bhatnagar–Gross–Krook (BGK) single relaxation time and the multi-relaxation-time (MRT) are the most common approximations for the collision step [66].

1.4.2 Cell level modelling

Among VRFB models, cell-level modeling is the most common. The objective of cell modeling is to simulate physicochemical phenomena inside the unit cell. In general, the simulation domain includes cell components: membrane, electrolyte, electrodes, flow plates and current collectors. Depending on the complexity of the model, continuum equations may be employed: conservation of mass, momentum, species, charge, and energy equations. However, including and solving all relevant continuum equations in the simulation domain is computationally expensive due to the presence of highly nonlinear terms and coefficients in the partial differential equations. Therefore, certain simplified assumptions are employed to obtain effective and quick solutions. Commonly-adopted assumptions include: dilute solution, laminar and incompressible fluid flow, isotropic and homogeneous physical properties for cell components, simplified redox half-reactions, no side reactions (hydrogen and oxygen/carbon dioxide evolution), isothermal conditions, no

crossover (i.e. membrane is impermeable to all ions except protons), no ionic interactions in the electrolyte, and no effect of gravity. Further simplifications include steady state behavior, though transient models have been described. System geometry can range from zero to three dimensions [66,67].

A zero-dimensional, transient VRFB cell model has predicted dynamic VRFB behavior based on physical phenomena and chemical reactions. [68]. Two-dimensional transient models have been developed based on conservation of mass, momentum, and charge [69,70]. Other works include an energy balance and the effect of temperature during charging/discharging [71–73]. Models including side reactions, e.g. hydrogen evolution [74] and oxygen evolution [75] have been reported. To provide more detail on mass transport mechanisms and electrochemical processes, three-dimensional models [76–79] are proposed. A modified Nernst equation for the VRFB predicts open circuit potential more accurately [80]. More complicated models have included ionic crossover through the membrane, offering more realistic simulation [18,81,82]. To address the computational demand of those realistic models, an asymptotic method is proposed to decrease computation cost while retaining acceptable accuracy [83,84].

Maximum electrolyte utilization and uniform current density distribution are directly influenced by electrolyte distribution in VRFBs; this distribution is highly dependent on electrolyte flow behavior at the transition between flow field channels and electrode porous media. Computational fluid dynamics (CFD) is a well-developed, robust numerical simulation of fluid flow that is commonly utilized in VRFB literature. Ke et al. showed that the limiting current can be predicted by calculating the electrolyte penetration

to the electrode: increased convection in the porous layer yielded improved performance [41,44,85]. Houser et al. achieved higher electrode velocity via equal path length (EPL) and aspect ratio (AR) flow field designs that show superior electrochemical performance [27]. Maurya et al. investigated different flow field designs where enhanced electrochemical performance was attributed to the increased electrode flow velocity [45]. More sophisticated models that include electrochemical reactions have also been developed to explore electrolyte velocity impact. You et al. investigated the correlation between mass transfer coefficient and electrolyte velocity by measuring limiting currents [86]. Kok et al. extensively studied the impact of electrode morphology and cell architecture on electrochemical performance. Increased electrolyte velocity in the electrode improves mass transport losses by reducing diffusion path length [49]. Other works have also reported the convection impact on electrochemical performance [28,37,43,87,88].

1.5 Objectives

The objectives of this work are explained in the chapters listed below:

Chapter 2 identifies bulk motion and concentration-driven mass transport mechanisms in the electrode and describes investigation of their individual impacts on electrochemical performance and distribution.

Chapter 3 elucidates the relationship between the convection in the electrode (electrolyte velocity) and electrochemical performance and distribution.

Chapter 4 demonstrates the most influential mass transport parameters (electrode permeability and diffusion coefficient of vanadium active species) and their impacts on the electrochemical performance and distribution.

Chapter 5 demonstrates that the in-plane electrolyte permeability of electrodes can be determined both experimentally and computationally.

Chapter 2 In-Situ Current Distribution and Mass Transport Analysis via Strip Cell Architecture for a Vanadium Redox Flow Battery

This chapter is revised based on the published papers [1,4]

Ertugrul, T. Y., Clement, J. T., Gandomi, Y. A., Aaron, D. S., and Mench, M. M. “**In-Situ Current Distribution and Mass Transport Analysis via Strip Cell Architecture for a Vanadium Redox Flow Battery**” *Journal of Power Sources* 437, (2019): 226920. doi:10.1016/j.jpowsour.2019.226920

Ertugrul, T. Y., Clement, J. T., Gandomi, Y. A., and Aaron, D. “**Isolation of Mass Transport and Current Distribution in Vanadium Flow Batteries Via Segmented Strip Cell**” *ECS Meeting Abstracts* (2019): 10–13. doi:10.1149/ma201

My contributions to this work were collection, reduction, and analysis of data as well as composition of the manuscript. Clement and Gandomi assisted with data collection. Aaron and Mench assisted in analysis of data and composition of the manuscript.

Abstract

In this chapter, diffusion and convection are experimentally investigated in a VRFB test bed using a strip cell architecture, having only one straight channel and 1 cm² active area. To study diffusion and convection-dominated mass transport regimes, various channel depths (0.25, 0.5, 1, 2.5 mm) are employed. The diffusion-dominated condition is imposed with deeper channel depths while convection-dominated conditions are achieved with shallower channel depths. It is found that diffusion-dominated cells have large current gradients; convection-dominated cells have relatively uniform current distribution from inlet to outlet under a mass transport limited condition. Although increasing flow rate is frequently found to improve electrochemical performance, it is observed that there is no discernible change in current distribution when increasing flow rate in diffusion-dominated VRFB cells. Pressure drop tests also show that superior electrochemical performance can

be achieved with reduced relative pressure drop in convection-dominated cells. In light of such findings, an optimization point is proposed for the strip cell architecture; such a point will vary with any other architecture and system, but this approach can be applied to any flowing system.

2.1 Introduction

The motion of electroactive species under dilute-solution theory assumptions in the electrode is described using the Nernst-Planck equation. The theory includes three mass transport mechanisms: migration, diffusion, and convection [89]. Isolating mass transport mechanisms and understanding their effects can help to mitigate mass transport losses, improve the cell design, and subsequently reduce undesired parasitic losses. Mass transport mechanisms in flowing electrochemical systems have been investigated extensively in the proton exchange membrane fuel cell literature. LaManna et al. utilized high resolution neutron imaging to isolate convection- and diffusion-driven mass transport mechanisms [90]. In redox flow battery literature, mass transport mechanisms have been computationally investigated in a Nafion® membrane [91–93]. Mass transport mechanisms in the electrode have been investigated in terms of contribution to crossover [92]. Some other studies quantified mass transport rates (diffusion coefficient, mass transport coefficient) in redox flow batteries [86,94,95]. However, these studies have often been conducted on relatively complex flow fields (e.g. serpentine, interdigitated, and parallel). Computational fluid dynamics simulation and current distribution measurements have shown that multiple mass transport mechanisms influence electrochemical performance in these designs due to the local electrolyte velocity and pressure drop

variations along the channel [26,54]. Therefore, capturing the impact of individual mass transport mechanisms is quite challenging. Additionally, electrochemical reactions and mass transport phenomena occur simultaneously in VRFBs; these interrelated parameters are difficult to disentangle experimentally. Consequently, limited studies have investigated transport mechanisms on such a focused level in the VRFB literature. A comprehensive and suitably validated mathematical simulation is required to understand physicochemical processes in VRFBs.

Motivated by this gap in the VRFB literature, our goal in this study is to investigate the impact of diffusion and convection mass transport mechanisms by employing in-situ current distribution diagnostics. The effects of migration are conventionally neglected in the literature due to relatively small effect in the electrode [15]. A strip cell architecture with only one straight channel and 1 cm² active area is implemented to achieve relatively uniform electrolyte velocity along the channel. Four different channel depth configurations, 0.25, 0.5, 1, and 2.5 mm, are employed to characterize the mass transport mechanisms in the strip cell. The 1-D strip cells developed for this study effectively eliminate higher-dimensional behaviors (e.g. channel hopping, bypass at channel switchbacks, and potential fluid short circuits), providing straightforward systems for phenomenological as well as comparative and detailed model validation studies.

2.2 Materials and methods

2.2.1 Experimental setup and strip cell architecture

The strip cell experimental test system includes a membrane, electrodes, gaskets, flow plates, current collectors, the printed circuit board (PCB), and compression plates as

shown in Figure 2.1. Nafion® 117 membranes (DuPont™, Wilmington, DE, USA) and carbon paper electrodes (39AA, SGL Group; 280 μm nominal uncompressed thickness) were employed in all tests. Because carbon paper electrodes were used, a zero-depth channel was not practical due to high pressure drop through the cell. Fully segmented strip cell flow plates with 1 cm^2 active area (5 cm long, 0.2 cm wide) and varying depths (0.25, 0.5, 1, and 2.5 mm) were made in-house. As shown in Figure 2.1b, a side inlet and outlet flow plate design was required due to the presence of the PCB. Flow plates were made of BMC 940 (Bulk Molding Compounds, Inc.), impermeable to liquids after curing. The channels which separate segments were machined to mirror the spacing on the PCB and then filled with thermoset resin (EpoMet., Buehler) to provide electronic isolation. The PCB, consisting of 4.5 mm by 4.5 mm segments with 0.5 mm spacing, was placed between the segmented flow plate and the current collector.

2.2.2 Electrolyte solution preparation

Tests were conducted with 1.5 M vanadyl sulfate (Alfa Aesar, 99.9%) in 3.3 M sulfuric acid electrolyte (Alfa Aesar, ACS grade). Initially, charging began with 100 mL and 50 mL electrolyte on the positive and negative sides, respectively. The electrolyte was potentiostatically charged at 1.7 V until a cut off current of 50 mA cm^{-2} was reached. Then half of the positive electrolyte was removed to obtain equal volumes of charged electrolyte. Finally, the electrolyte was galvanostatically discharged to 50% state of charge (SOC). Nitrogen was continuously bubbled in the negative electrolyte to prevent oxidation of vanadium species (V(II)).

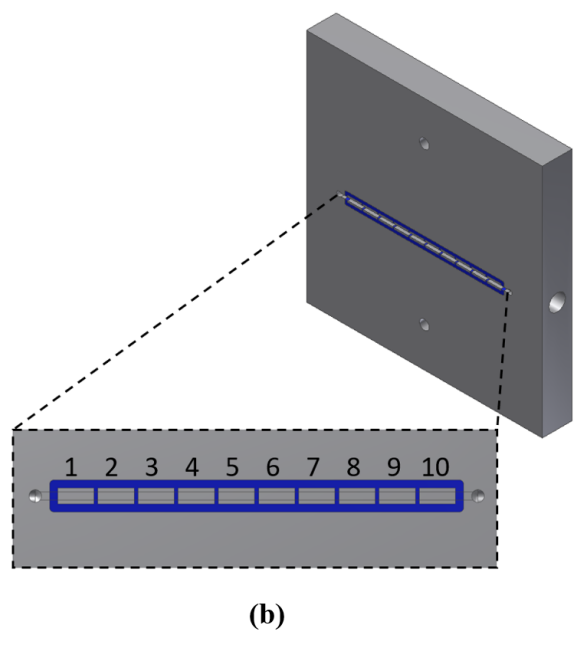
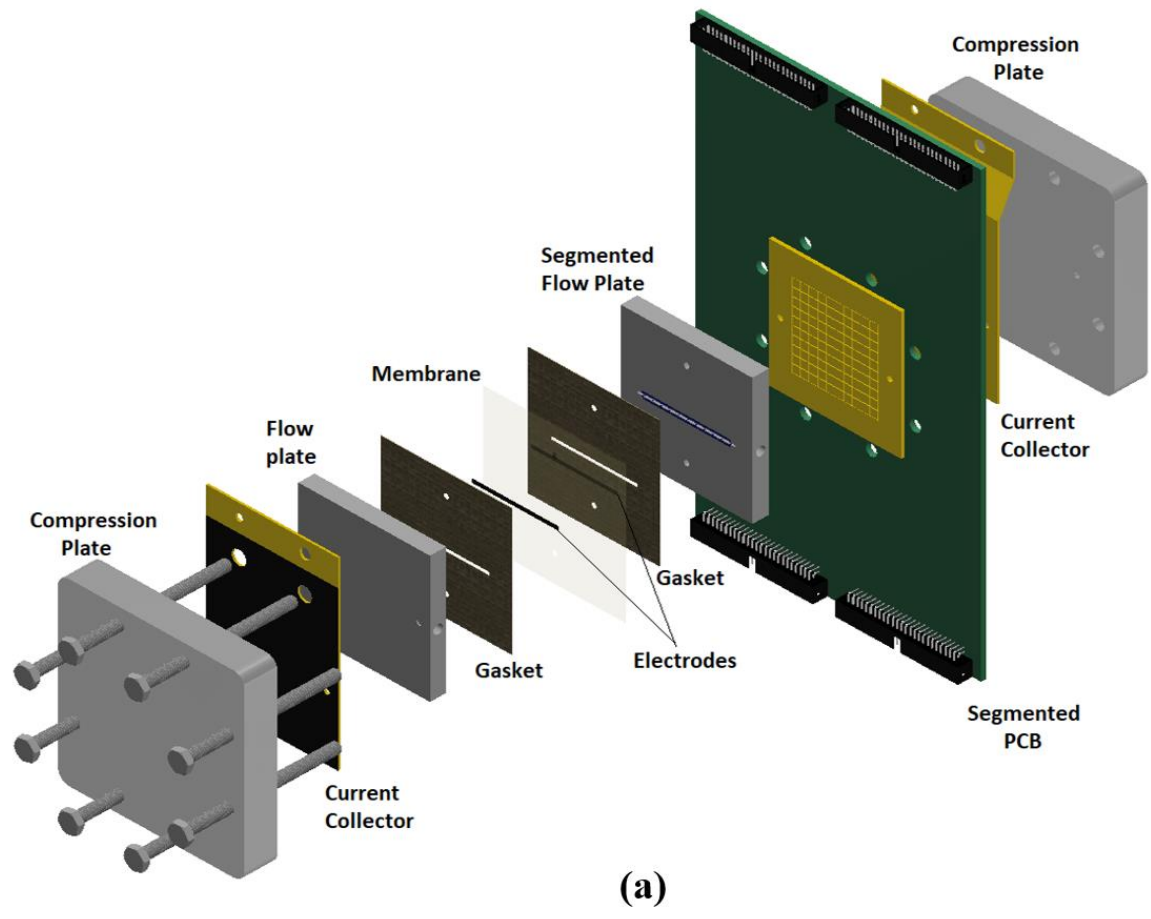


Figure 2.1 Exploded view of VRFB strip cell (a) and (b) strip cell segmented flow plate.

2.2.3 Polarization curves and in-situ localized current distribution measurements

Polarization curves and in-situ localized current distribution measurements were performed for all channel depth designs at the flow rates of 10-50 mL min⁻¹ at 50% SOC; since the channel area was 1.0 cm², all flow rates reported here were also area-specific flow rates. Constant SOC at the cell inlet was ensured by performing single-pass polarization curves. This approach utilizes two reservoirs on each side, one for each cell inlet and outlet, to prevent any recirculation of electrolyte. All cells were controlled potentiostatically from 1.7 V to 0.2 V in equally-spaced increments. Corresponding current was recorded at each steady-state voltage step. Measured maximum current for each cell (at 0.2 V) is considered the limiting current for the corresponding cell. While a multichannel potentiostat/galvanostat (Arbin Instruments, College Station, TX) was used for polarization curves, a National Instruments data acquisition system with a custom LabVIEW program collected data from the PCB in real time. Distributed data for each segment were collected every second and averaged over 6 seconds. Averaged data were presented as local current density distribution and a percent deviation of distribution. Percent deviation of distribution was presented as either contour or line/scatter plots. Experimental error for current distribution measurements was assessed via repeated testing and found to be small (maximum $\pm 5\%$). Details of the technique were provided in previous work [54].

2.2.4 Crossover measurements

To conduct crossover experiments, an experimental test system including flow cells, peristaltic pumps (Cole Parmer, Masterflex L/S, Vernon Hills, IL, USA), external

reservoirs, light sources (Ocean-Optics, Dunedin, FL, USA) as well as ultraviolet/visible (UV-Vis) spectrometers (THORLABS, Newton, NJ, USA) was utilized. A full description of the set-up was provided in previous publications from this group [3, 4]. Two different electrolyte solutions (vanadium-enriched and vanadium-deficient electrolytes) were used to assess the rate of crossover for different configurations. Vanadium-enriched electrolyte was 1.5 M $\text{VOSO}_4 \cdot x\text{H}_2\text{O}$ (Alfa Aesar, USA) and 3.3 M sulfuric acid (Alfa Aesar, USA); whereas the vanadium-deficient side was 4.8 M aqueous sulfuric acid. The vanadium-enriched and vanadium-deficient solutions were circulated through the strip cell using a two-channel peristaltic pump at volumetric flow rate of 30 mL/min. The solutions were subsequently directed to UV-Vis flow cells to quantify the composition of the vanadium-deficient side's electrolyte in real time. The total time of electrolyte circulation was ~48 hours while real-time spectroscopic data were recorded at ~ 12 hours intervals. Spectroscopic data were used to quantify the vanadium ion concentration in the vanadium-deficient electrolyte. A similar experimental procedure was repeated for various configurations of the strip cell.

2.2.5 Pressure drop measurements

Pressure drop inside the strip cell is investigated experimentally via two PTFE pressure transducers (TemTech) with a pressure range from 0 to 344.7 kPa (± 0.7 kPa). Transducers are located at the strip cell inlet and outlet. Pressure drop data are obtained for a range of flow rates from 10 mL/min up to 50 mL/min. The error associated with experimental measurement is shown with an error bar.

2.3 Results and discussions

The in-plane current distribution for an operating cell is a strong function of dominant transport mechanism in the electrodes [26,54]. However, crossover of vanadium ions through the membrane can also affect the in-plane current distribution if the membrane is highly permeable to the redox active species. To test this, current density distributions were measured for strip cells with N117 and N211 membranes; with all other conditions identical, no impact of membrane thickness on current density distribution was observed. In this work, major driving forces affecting the transport of vanadium ions from the flow field through the electrodes are explored using current distribution diagnostics. A series of vanadium crossover experiments with varying cell configuration (channel depth: 0.25, 0.5, 1, and 2.5 mm) were conducted to measure the permeability of ion-exchange membranes to vanadium ions. Figure 2.2 includes the concentration of vanadium ions (V(IV)) within the vanadium-deficient electrolytes for various cell configurations. As shown in Figure 2.2, the concentration of diffused vanadium ions increased for decreased channel depth. The major contributor for increased vanadium crossover is increased convective flow and relative pressure difference within the electrodes as a function of decreased channel depth. According to Figure 2.2, the concentration of diffused vanadium ions within the vanadium-deficient electrolyte at the end of 48-hour experiment varied in the range of $\sim 0.003 - 0.023$ M for various configurations. Therefore, considering the timescale for conducting current distribution measurements (5 min), it was assumed that the impacts of crossover flux on the real-time and in-plane current density measurements were insignificant factors for the measured results for various configurations of the strip cell considered in this work.

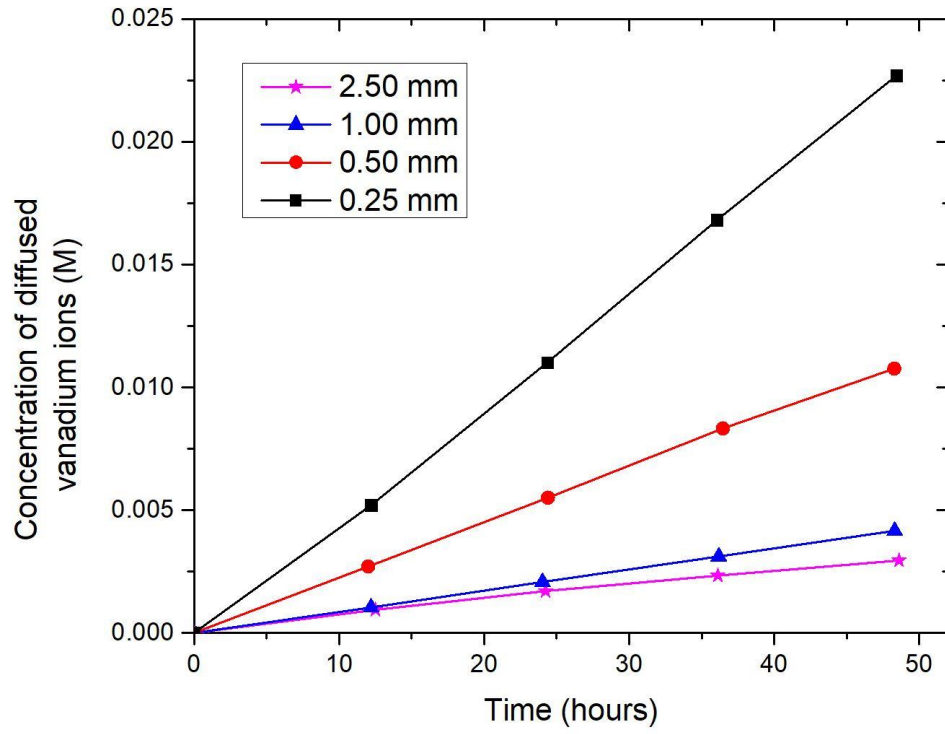


Figure 2.2 Experimentally-measured crossover for four different channel depths.

Polarization curve analysis is a common method to evaluate cell performance in electrochemical devices. It can also provide useful insight for identifying dominant performance limitations. Figure 2.3 shows charge-discharge polarization curves for all strip cell configurations at 50% SOC, 30 ml min⁻¹ flow rate. It is clearly seen that the channel depth (and thus local concentration and pressure gradients) strongly influences VRFB electrochemical performance. As the channel depth decreases, overall cell performance increases. During discharge, limiting current densities (at 0.2 V) are 0.17, 0.26, 0.56, 1.48 A cm⁻² respectively. This improvement is attributed to increased convective mass transport in the electrode. It is also evident that, while the deeper channels (2.5, 1, and 0.5 mm) exhibit mass transport limitation, there is no discernible mass transport limitation for the 0.25 mm cell configuration. Mass transport limitation is indicated by a steep, nonlinear slope to the polarization curve at high current [40]. While the three deeper channels reach the mass transport-limited region around 0.8 V, the 0.25 mm cell continued to provide increasing current over the entire voltage range. The impact of operation voltage on the current density distribution for all cell configurations is investigated later in this work.

Localized current data are presented in two ways: measured current distribution and as a percent deviation from the average current distribution as calculated in Eq. (2.1):

$$\text{Deviation from average(\%)} = \frac{\text{segment actual CD} - \text{cell average CD}}{\text{cell average CD}} \times 100 \quad (2.1)$$

Normalized current distribution enables comparative quantification of current deviation from inlet to outlet. The flow direction is from left (the cell inlet at segment 1) to right (the cell outlet at segment 10). Figure 2.4 includes down-the-channel normalized current distribution data for all strip cell configurations at 50% SOC, 30 ml min⁻¹ flow rate,

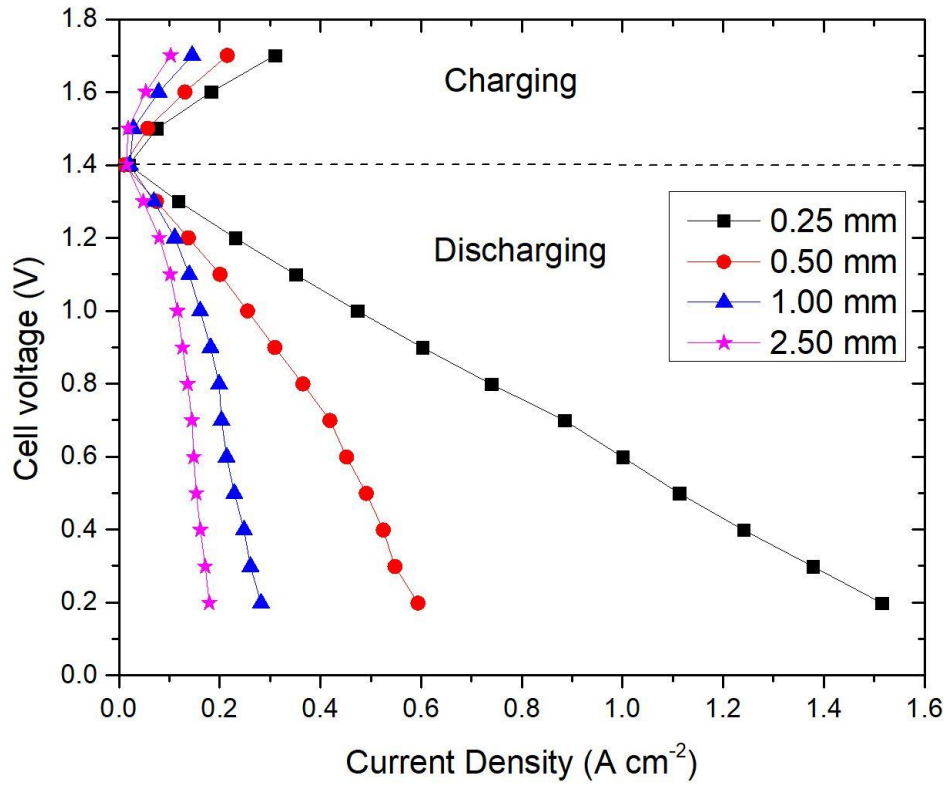


Figure 2.3 Polarization curves for all channel depths at 50% SOC, 30 mL min⁻¹.

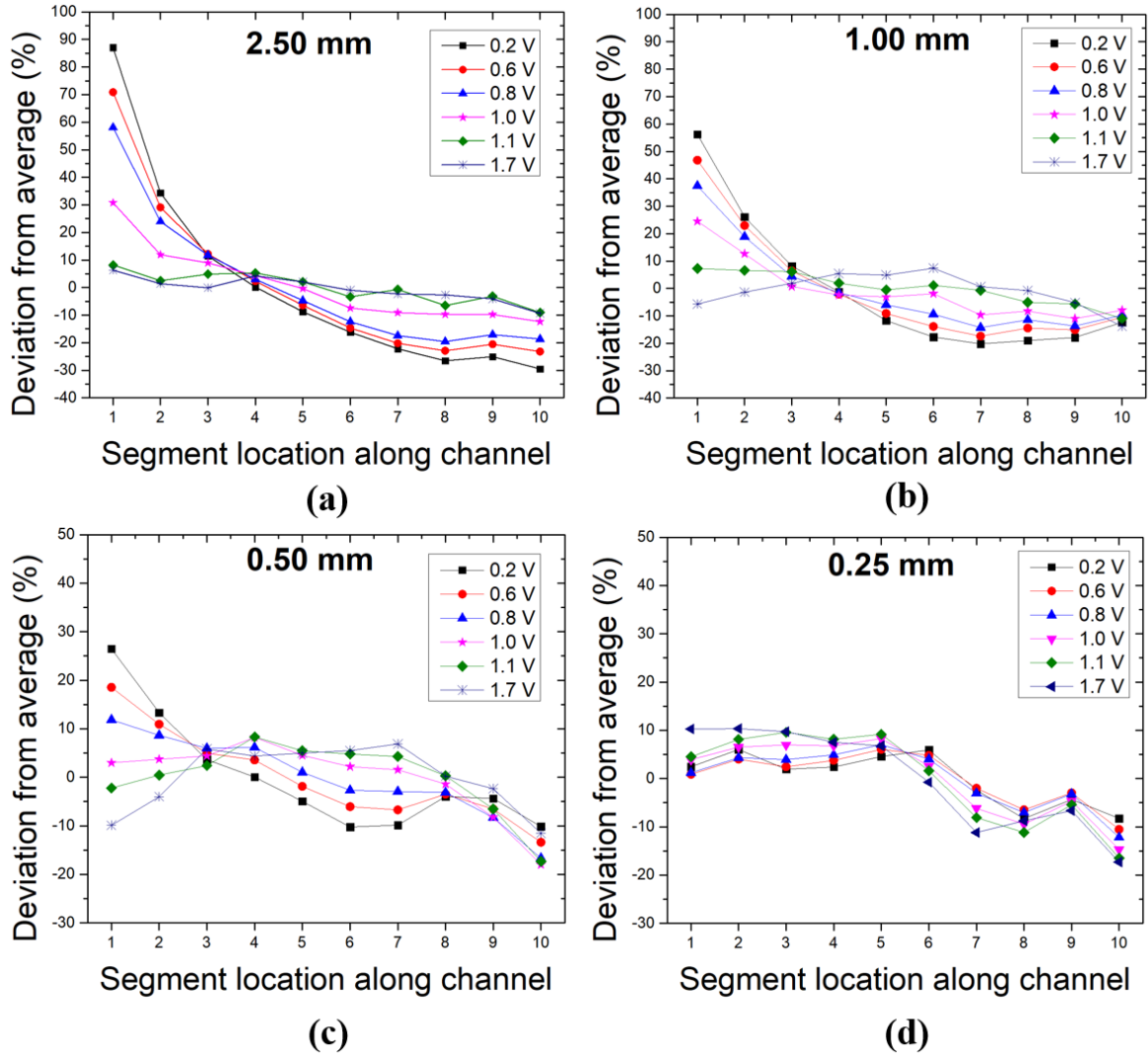
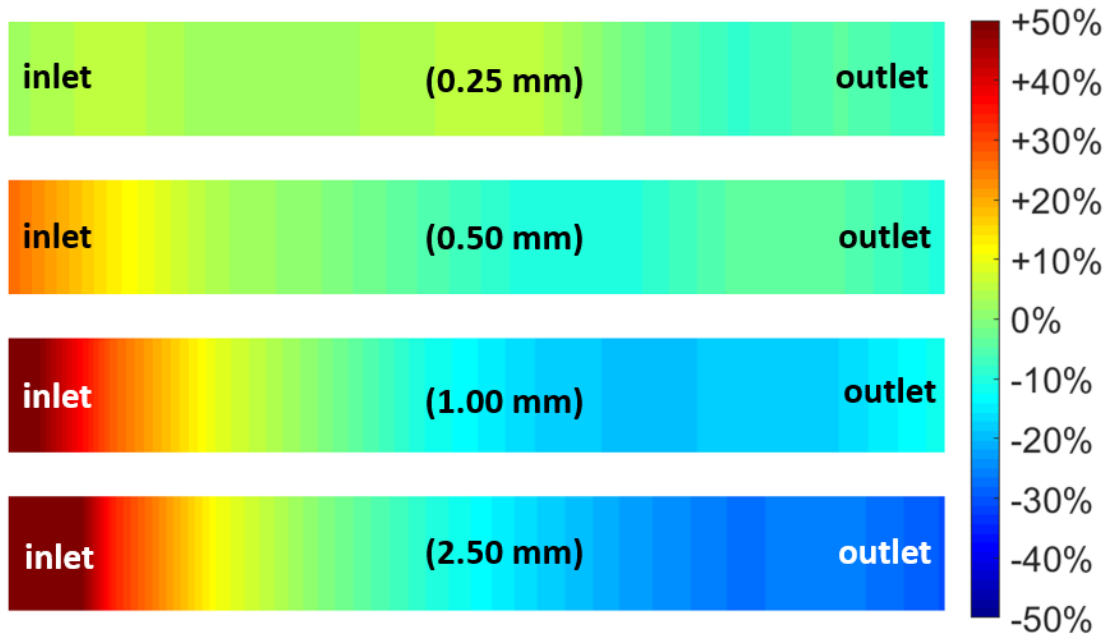


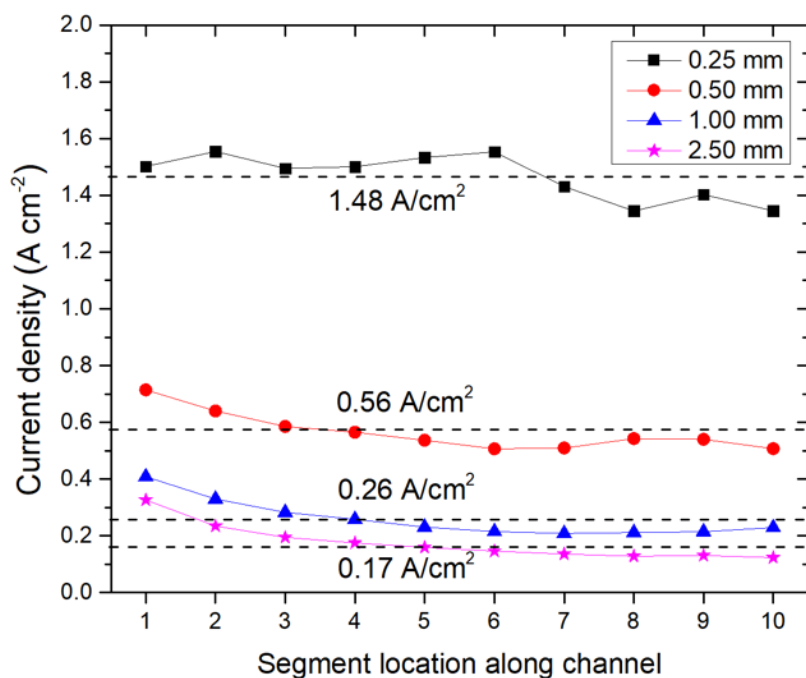
Figure 2.4 Normalized current distributions for various points on the polarization curve at 50% SOC, 30 mL min⁻¹ for channel depths (a) 2.50 mm (b) 1 mm (c) 0.5 mm (d) 0.25 mm.

and various voltages on the polarization curves. As seen in Figures 2.4a-d during charging (1.7 V) current distributions are similar and relatively uniform from inlet to outlet for all cell configurations. Uniform current distribution is an indicator of sufficient electroactive species transport in the electrode. Thus, it can be concluded that charging under these conditions is not a mass transport-limited process for VRFBs. Similarly, during discharge at low-to-moderate current density, current distributions do not change significantly. However, when the mass transport limiting region is reached, currents deviate drastically from the average down-the-channel, as shown in Figures 2.4a-c; cell configuration 0.25 mm shown in Figure 2.4d is an exception here since it is not a mass transport limited cell. It is clearly seen that the highest current deviations are obtained at the limiting current condition (0.2 V). Therefore, the impact of channel depth and flow rate on the current density distribution is investigated at limiting current in the following sections.

Figure 2.5 compares the impact of channel depth and concomitant gradients on the current distribution at 50% SOC, 30 ml min⁻¹ flow rate, and limiting current condition. The normalized current distribution is presented as a contour plot in Figure 2.5a and actual current distribution is presented as a scatter plot in Figure 2.5b. As shown in Figure 2.5a, all cell configurations except 0.25 mm depth have similar behavior with large current gradients from inlet to outlet. Conversely, the 0.25 mm depth channel shows relatively homogeneous distribution. While the lowest current deviation from inlet to outlet is obtained (+2% to -8%) for the shallowest channel (0.25 mm), the highest current deviation is observed (+88% to -30%) for the deepest channel (2.5 mm). These two different current deviation patterns can be attributed to convection-dominated and diffusion-limited mass



(a)



(b)

Figure 2.5 Normalized current (a) and (b) local current distribution comparisons for four different depth channels at 50% SOC, 30 mL min⁻¹, 0.2 V hold.

transport mechanisms in the electrode. As channel depth decreases, channel velocity increases and more electrolyte is forced to flow through the electrode so that the convective flow in the electrode increases; accordingly, current distribution approaches uniformity from the inlet to outlet. Conversely, as channel depth increases, electrolyte penetration in the electrode decreases due to the lower channel velocity and pressure drop; diffusion then is the major transport mechanism of reactant into the electrode. At a mass-limiting current condition, active species are consumed very rapidly in the electrode surface to maintain high current. As a result, local concentration drastically drops.

Increased convective flow can explain the measured current density distribution shown in Figure 2.5b. Decreasing channel depth by a factor of two led to doubled average current for 1.0 mm to 0.5 mm depth. A maximum current density of 1.48 A cm^{-2} is achieved with the shallowest channel depth (0.25 mm) configuration. However, shallower channel depth induces greater pressure drop inside the cell. Figure 2.6 shows experimentally-measured pressure drop results for all cell configurations for flow rates ranging from 10 mL min^{-1} to 50 mL min^{-1} . It is seen that the pressure drop increases significantly as the channel depth decreases. Pressure drop for the 0.25 mm channel depth reaches a maximum value of $1.23 \times 10^5 \text{ Pa}$ at 30 mL min^{-1} flow rate.

It is shown in the previous section that decreasing channel depth increases local channel velocity and convective flow in the electrode, minimizing current deviation. Convective flow can also be improved simply by increasing flow rate for any channel depth. Figures 2.7 and 8 summarize the flow rate effect on current distribution for all cell configurations at 0.2 V and 50% SOC. Three flow rates, 10 ml min^{-1} , 30 ml min^{-1} ,

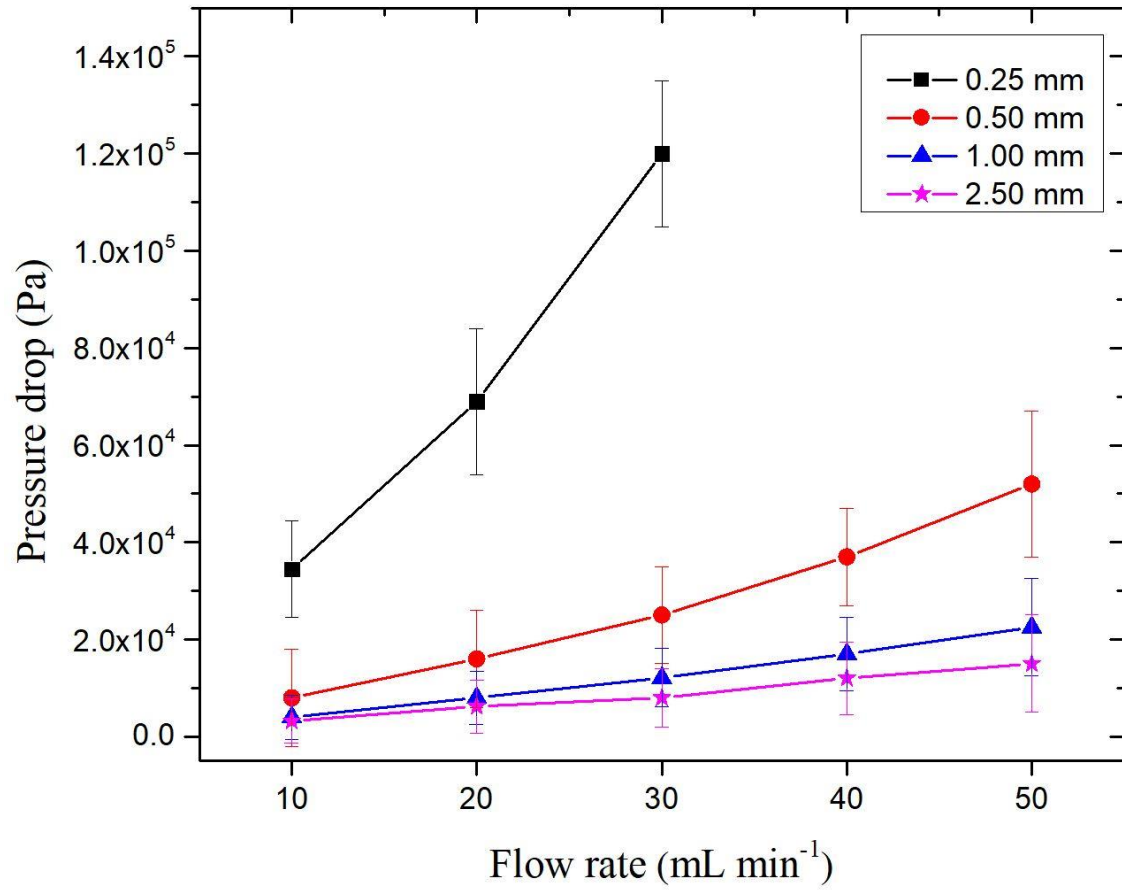


Figure 2.6 Experimentally-measured pressure drop data for four different channel depths.

50 ml min⁻¹, were selected to investigate the impact of flow rate. Testing 50 ml min⁻¹ flow rate with 0.25 mm channel depth was not possible due to excessive pressure drop. Figure 2.7 shows current distribution results for channel depths of 2.5 mm and 1 mm. As seen in figure 2.7a and 2.7b, increasing flow rate increases the overall cell performance (parallel current shifting). However, as seen in figure 2.7c and 2.7d, normalized currents are not affected by the flow rate change: all show high current deviation at the inlet and low current deviation at the outlet. Increasing flow rate improves absolute current density but does not influence the qualitative change in current distribution; such behavior is a distinct characteristic of diffusion-dominated mass transport in the electrode. Deep channels and concomitantly low flow rates and pressure differences limit convective mass transport into the porous electrode even at higher flow rates. It is also seen in the pressure drop tests (Figure 2.6) that increasing flow rate does not induce considerable pressure drop in the deep-channel strip cells. Consequently, there is no discernible benefit to increasing flow rate in diffusion-dominated VRFB cells for the range of flow rate considered here (based on the literature, 50 ml min⁻¹cm⁻² is exceptionally high). On the other hand, increasing flow rate in shallower-channel cells (0.5 mm and 0.25 mm), as shown in Figure 2.8, not only increases the average current density but also changes the current distribution pattern: current distributions become more uniform as flow rate increases. For the 0.5 mm channel depth, normalized current at the inlet (segment #1) decreased from +53% to +12% as flow rate increased from 10 ml min⁻¹ to 50 ml min⁻¹. Similarly, for the 0.25 mm channel depth, normalized current decreased from +22% to +2% at the inlet (segment #1) as flow rate increased from 10 ml min⁻¹ to 30 ml min⁻¹. These results imply that increasing flow rate

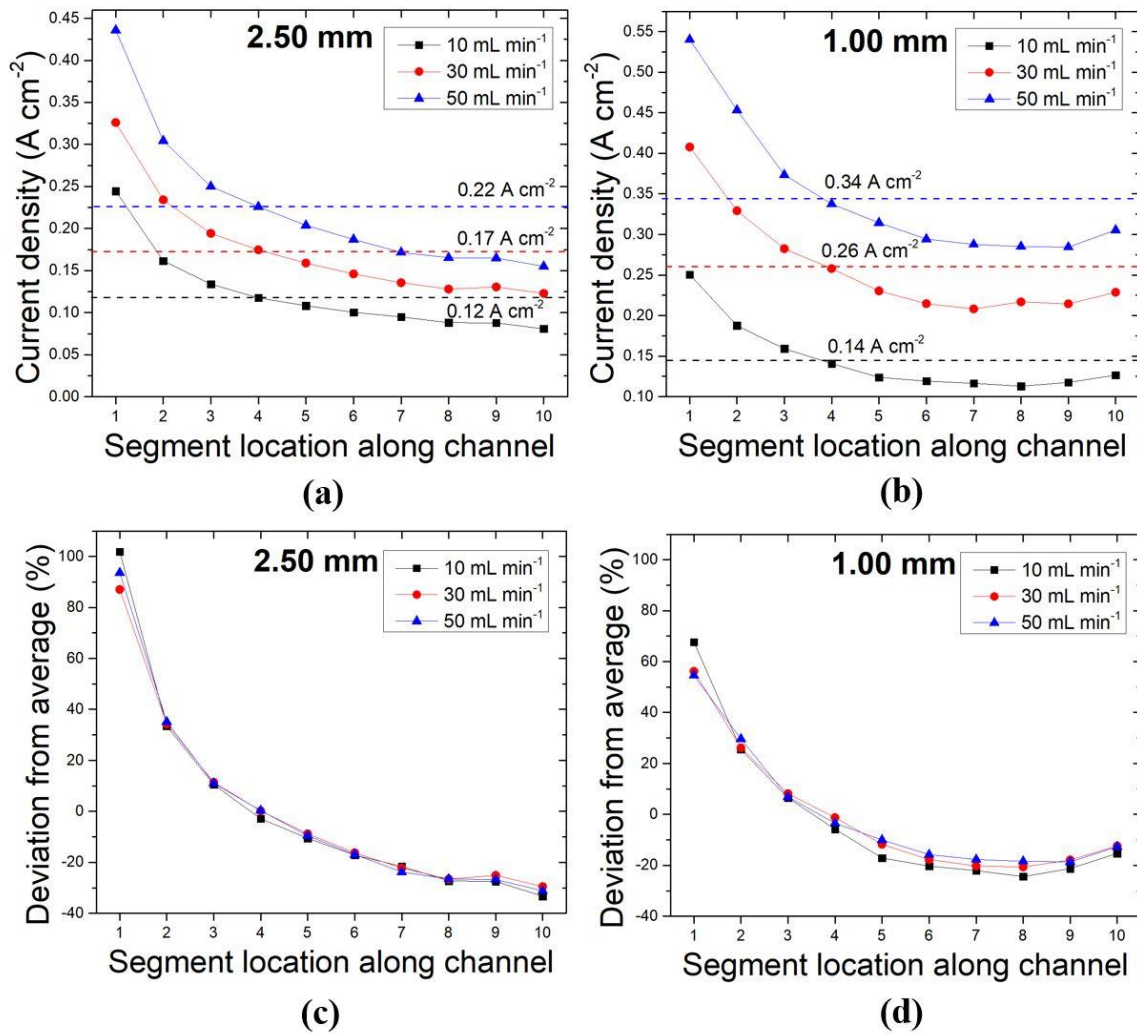


Figure 2.7 Impact of flow rate on the local current at 50% SOC, 0.2 V hold (a) and (b) for 2.5 mm and 1mm depth channels, respectively; (c) and (d) normalized current distributions for 2.5 mm and 1 mm depth channels, respectively.

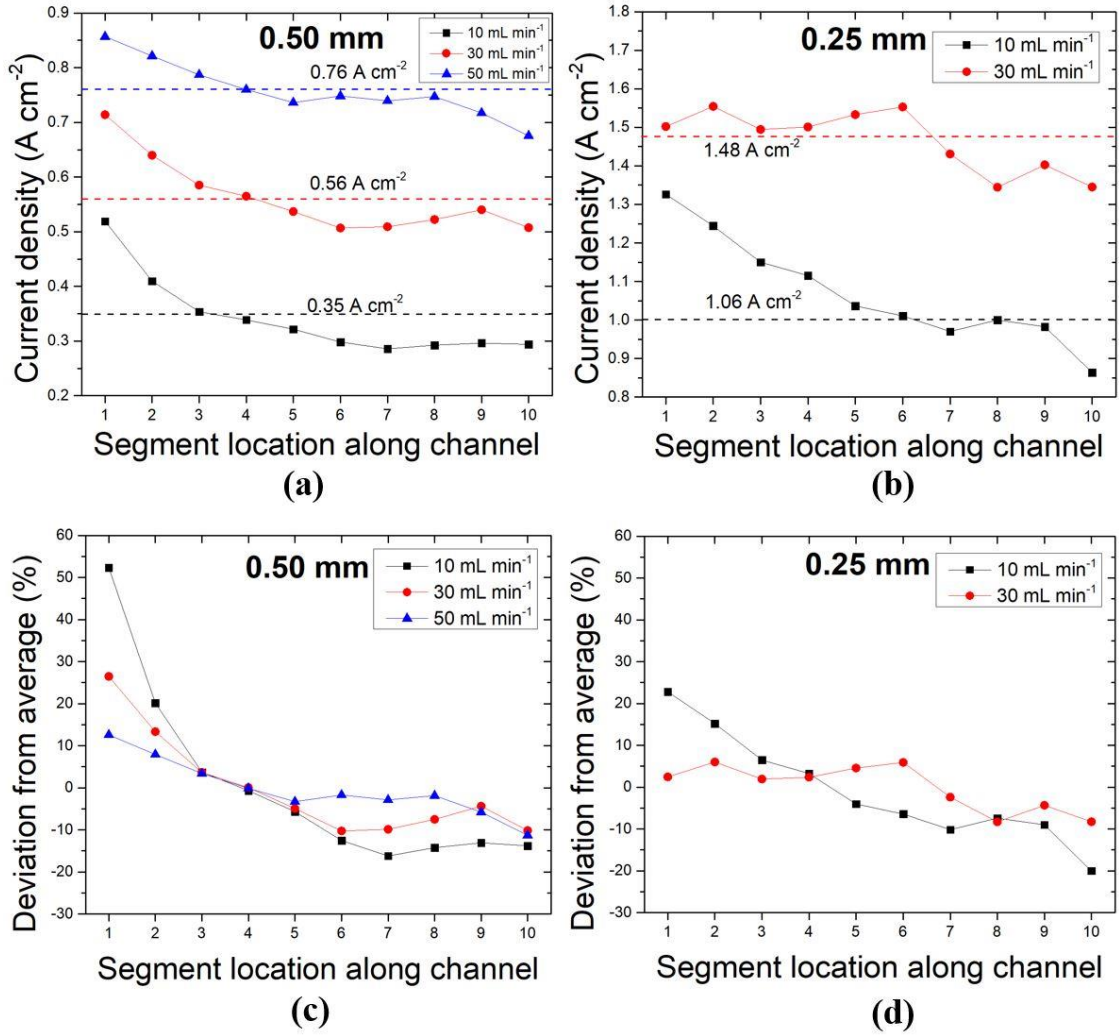


Figure 2.8 Impact of flow rate on the local current at 50% SOC 0.2V hold (a) and (b) 0.5mm and 0.25 mm depth channels, respectively; (c) and (d) normalized current distributions for 0.5 mm and 0.25 mm depth channels, respectively.

considerably improves electrochemical performance via increased convective flow in the electrodes. Thus, the dramatic pressure drop increase in these convection-dominated cells is attributed to convective-flow enhancement.

It is clear that increased pressure drop is an inevitable consequence of improved convective mass transport; also, increased convective flow usually enhances the electrochemical performance. Increased pressure drop correlates with pumping power requirements, which has a negative impact on system energy efficiency. Thus, it is essential to identify an optimum balance between pumping power and electrochemical performance to maximize net system efficiency. However, increased pressure drop and performance are not linearly related, complicating such optimization efforts. Motivated by this viewpoint, convection-dominated and diffusion-dominated cells were compared. Table 2.1 summarizes measured average current densities and pressure drops for all flow rates and cell configurations. As seen in Table 2.1, pressure drop for a cell configuration with 0.5 mm channel depth and 10 ml min⁻¹ flow rate is slightly lower than the cell configuration with 2.5 mm depth and 1 mm at 50 ml min⁻¹ flow rate. However, the cell configuration with 0.5 mm depth outperforms both cell configurations with 2.5 mm and 1 mm depths in terms of average current density. Similarly, although pressure drop for 0.25 mm depth at 10 ml min⁻¹ is lower than pressure drop for 0.5 mm depth at 50 ml min⁻¹, electrochemical performance is much better for 0.25 mm depth. So, equivalent electrochemical performance occurring with lower pressure drop is an example of an optimization point. A more efficient approach to identifying such a point, for any cell design, should be the subject of a simulation-focused effort. Additionally, a robust simulation would also enable

Table 2.1 Summary of operating conditions.

Flow rate (mL min⁻¹)		Channel depth (mm)			
		2.50	1.00	0.50	0.25
10	Current density (A cm ⁻²)	0.12	0.14	0.35	1.06
	Pressure drop (Pa)	3.2 x10 ³	4.0 x10 ³	8.10 x10 ³	3.45x10 ⁴
30	Current density (A cm ⁻²)	0.17	0.26	0.56	1.48
	Pressure drop (Pa)	8.0 x10 ³	1.21 x10 ⁴	2.5 x10 ⁴	1.23 x10 ⁵
50	Current density (A cm ⁻²)	0.22	0.34	0.76	-
	Pressure drop (Pa)	1.5 x10 ⁴	2.25 x10 ⁴	5.10 x10 ⁴	-

understanding of active species concentration distributions throughout the electrode volume. The strip cell geometry is suitable for validation of such a modelling approach, which is the subject of ongoing work.

2.5 Conclusions

In VRFBs, isolation, identification, and control of mass transport losses is critically important. The simple strip cell design allows isolation of mass transport mechanisms by suppressing higher-dimensional behaviors (e.g. channel hopping, bypass at channel switchbacks, and potential fluid short circuits). Thus, the effect of individual transport mechanisms can be investigated. The PCB technique, along with fully-segmented flow plates, enables high spatial resolution and is employed to obtain localized current distribution. Vanadium crossover was experimentally measured for all cell configurations (0.25, 0.5, 1, 2.5 mm channel depths), and its contribution to current distribution was found to be insignificant for strip cell architecture. Major parameters affecting current distribution considered in this work include operating voltage, channel depth, and flow rate. While charging is generally not a mass transport limited process, nonuniform current distributions are observed once the mass transport limited region is reached during discharge. The highest current deviation from inlet to outlet is observed for the deepest channel (2.5 mm) cell configuration, where channel velocity is lowest, and diffusion dominated flux to the electrode is dominant is an indicator of concentration gradient driven mass transport mechanism presence in the electrode. As channel depth decreases, current distribution approaches uniformity as a result of increased electrolyte velocity in the channel and correspondingly increased velocity in the electrode. It is also observed that the flow rate

contribution for improving bulk motion of the active species in the electrode is more distinct in convection-dominated cells (i.e. strip cells with channel depth of 0.25 and, 0.5 mm) than diffusion-limited cells (2.5 mm, 1 mm). This observation informs the conclusion that increased flow rate yields negligible benefit in diffusion-limited cells. While the conditions that result in diffusion limitation are particular to a cell design, this work shows that diffusion limitation is not readily alleviated solely by increasing electrolyte flow rate. Pressure drop tests reveal that it is possible to achieve better electrochemical performance with lower pressure drop in convection-dominated cells. Based on this finding, it is evident that there is a trade-off between pumping power requirement and electrochemical performance in VRFBs. A more practical optimization for VRFB can be achieved via comprehensive and suitably validated.

Chapter 3 Computational and Experimental Study of Convection in a Vanadium Redox Flow Battery Strip Cell Architecture

This chapter is revised based on the published papers [2,3]

Ertugrul, T. Y., Daugherty, M. C., Houser, J. R., Aaron, D. S., and Mench, M. M.
“Computational and Experimental Study of Convection in a Vanadium Redox Flow Battery Strip Cell Architecture” *Energies* 13, no. 18 (2020): 4767.
doi:10.3390/en13184767

T.Y. Ertugrul, J.R. Houser, M.C. Daugherty, D.S. Aaron and M.M. Mench.
“Understanding the Interplay between Electrolyte Velocity Distribution and Current Distribution in Vanadium Flow Battery Electrode” *ECS Meeting Abstracts* (2019): doi:10.1149/ma2019-02/1/14

My contributions to this work were, collection, reduction, and analysis of data as well as composition of the manuscript. Daugherty and Houser assisted with data collection. Aaron and Mench assisted in analysis of data and composition of the manuscript.

Abstract

The impact of convection on electrochemical performance, performance distribution, and local pressure drop is investigated via simple strip cell architecture, a cell with a single straight channel. Various channel depths (0.25, 0.5, 1, 2.5 mm) and flow rates ($10\text{-}50\text{ mL min}^{-1}\text{cm}^{-2}$) are employed to induce a wide range of electrolyte velocities within the channel and electrode. Computational flow simulation is utilized to assess velocity and pressure distributions; experimentally measured in-situ current distribution is quantified for the cell. Although the total current in the cell is directly proportional to electrolyte velocity in the electrode, there is no correlation detected between electrolyte velocity in the channel and the total current. It is found that maximum achievable current is limited by diffusion mass transport resistance between the liquid electrolyte and the electrode surfaces

at the pore level. Low electrolyte velocity induces large current gradients from inlet to outlet; conversely, high electrolyte velocity exhibits relatively uniform current distribution down the channel. Large current gradients are attributed to local concentration depletion in the electrode since the velocity distribution down the channel is uniform. Shallow channel configurations are observed to successfully compromise between convective flow in the electrode and the overall pressure drop.

3.1 Introduction

The goal in this study is to more directly measure the impact of convection on VRFB electrochemical performance. To achieve this, a computational fluid dynamics (CFD) model using COMSOL Multiphysics[®] software along with experimental, in-situ, localized current distribution diagnostics are utilized. Pressure drop analysis is also employed to support the conclusions and validate the modeling results. The CFD analysis used in this study reveals key hydrodynamic relations both in the channel and electrode so that the convection transport mechanism and its impact on electrochemical performance (both overall and distribution) is investigated more fundamentally. Experiments and numerical simulations were conducted for a strip cell architecture which has a simplified geometry with one straight channel and 1 cm² active area. A one-dimensional strip cell architecture eliminates complicated flow behaviors (e.g. potential fluid short circuits, bypass at channel switchbacks, and channel hopping) and minimizes local pressure drop variations in the channel. For these reasons, the strip cell is well-suited for phenomenological, comparative, and detailed model validation studies.

3.2 Materials and methods

In this study, a strip cell architecture, having only one straight channel and 1 cm² active area (5 cm long, 0.2 cm wide) was employed as introduced in previous work [1,4]. Simulations and experiments were conducted on varying channel depth designs (0.25, 0.5, 1, and 2.5 mm) at flow rates from 10-50 mL min⁻¹. A zero-depth channel was not possible for strip cell architecture due to the excessive pressure drop. While enhanced convection is achieved with the shallower channel depths (0.25, 0.5 mm), the deeper channel depths (1, 2.5 mm.) were employed to impose a diffusion limited condition in the electrode. Diffusion limitation is conventionally alleviated by increased flow rate; the conditions considered in this work span from 10 to 50 mL min⁻¹cm⁻². These area-specific flow rates ranged from conventional to very high. All tests were performed with Nafion® 117 membranes (DuPont™, Wilmington, DE, USA) and carbon paper electrodes (39AA, SGL Group; 280 μm nominal, uncompressed thickness). Flow plates were constructed of BMC 940 (Bulk Molding Compounds, Inc.), impermeable to liquids after curing. All channel depth configurations and segmentations were machined in-house.

An electrolyte solution of 1.5 M vanadyl sulfate (Alfa Aesar, 99.9%) in 3.3 M sulfuric acid (Alfa Aesar, ACS grade) was used to perform all tests. Initially, positive and negative side electrolytes (100 mL and 50 mL respectively) were charged at 1.7 V. Cutoff current during charging was 50 mA cm⁻². To achieve equal volumes of electrolyte, half of the positive electrolyte was removed. Lastly, the electrolyte was galvanostatically discharged to 50% SOC. Electrolyte reservoirs were continuously purged with nitrogen to prevent oxidation of vanadium species (V(II)).

Sensitivity analysis was conducted for various key parameters such as electrolyte density and viscosity, electrode porosity, and permeability. Electrode permeability is found to be the most significant parameter affecting electrolyte velocity distribution in the electrode. However, since it was employed a consistent electrode (carbon paper) and electrolyte composition (1.5 M vanadyl sulfate, 3.3 M sulfuric acid) for all tests, those parameters including permeability are identical for all simulations.

3.2.1 Polarization curves and in-situ current distribution measurements

All electrochemical measurements (polarization curves and in-situ localized current distribution measurements) were executed over the flow rate range of 10-50 mL min⁻¹; all reported flow rates can be considered area-specific flow rates since the active area was 1 cm². Single-pass polarization curves ensured a constant 50% SOC at the cell inlet. All experiments were conducted potentiostatically by sweeping cell voltage from 1.7 V to 0.2 V in equal increments and recording the current at each step. The maximum current for each cell (at 0.2 V) is considered here as the limiting current. Further details on the hardware, distributed current diagnostic equipment, and other experimental features can be found in previous work [1,54]. Experimental error for current distribution measurements was evaluated via repeated testing and found to be small (maximum $\pm 5\%$). It was shown in our previous study that lateral current between segments is insignificant [54]. However, it should be noted that the measurement technique is not capable of detecting current spread through the electrolyte due to potential gradients between segments. Details of the technique were provided previously [1].

3.2.2 Computational fluid dynamics

Predictions of the electrolyte flow distribution in the strip cell were obtained using COMSOL Multiphysics[®] software with a free and porous media flow module [96]. The simulation domain included a channel and porous electrode constructed in three dimensions, as shown in Figure 3.1. Conservation of mass and momentum were solved to obtain velocity and pressure distributions under the following assumptions: steady state, laminar and incompressible fluid flow, isotropic and homogeneous physical properties. While the fast flow profile in the channel is represented by the Navier-Stokes equations, the Brinkman equations [97] were used to model the comparatively slower flow in porous media (Eqs. 1 and 2),

$$\rho(u \cdot \nabla)u = \nabla \cdot [-pI + \mu(\nabla u + (\nabla u)^T)] + F \quad (3.1)$$

$$\rho \nabla \cdot u = 0$$

$$\rho(u \cdot \nabla)u = \nabla \cdot \left[-pI + \frac{\mu}{\varepsilon_p}(\nabla u + (\nabla u)^T) \right] - \left(\frac{\mu}{\kappa_{br}} + \beta_F |u| \right) u + F \quad (3.2)$$

$$\rho \nabla \cdot u = Q_m$$

where u is the superficial velocity, p is the pressure, ρ is the density, μ is the dynamic viscosity, ε_p is the porosity of the porous media, κ_{br} is the permeability of the porous media, Q_m is the mass source, F is the body forces acting upon the fluid, and β_F is the Forchheimer drag coefficient. Physical properties for the electrolyte and electrode as well as the other input parameters used for simulation are tabulated in Table 3.1. The flow field and the electrode dimensions were selected based on the 1 cm² strip cell architecture used

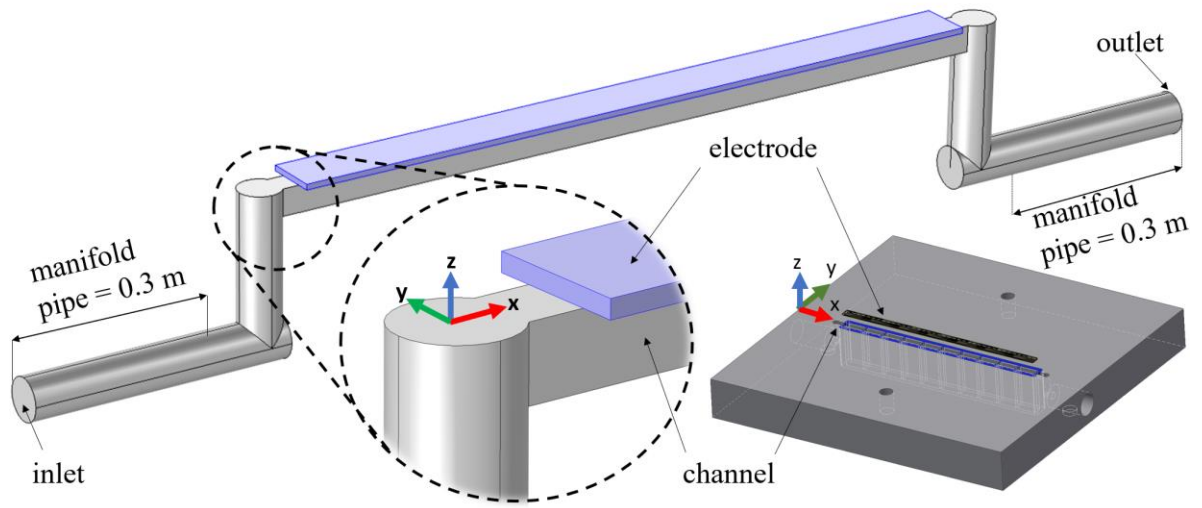


Figure 3.1 Simulation domains with channel and electrode [3]

Table 3.1 Simulation parameters

Parameter	Value	Reference
Channel and electrode length (mm)	50	Chosen
Channel width/land (mm)	1	Chosen
Channel depth (mm)	0.25, 0.50,1.00,2.50	Chosen
Electrode width (mm)	2	Chosen
Uncompressed electrode porosity (%)	89	SGL [98]
Compressed electrode porosity (%)	85	[99]
Electrode permeability x 10 ¹¹ (m ²)	1.1	SGL [98]
Electrolyte density (kg m ⁻³)	1350	[39,100]
Electrolyte viscosity x 1000 (Pa s)	2.5	[39,100]

in experiments. The electrode porosity and the permeability values for 39AA carbon paper were taken from the manufacturer (SGL) [98]. Considering the compression in the cell, porosity was adjusted to a value of 85% [99]. Electrolyte density and viscosity values were taken from the literature [39,100]. No-slip boundary conditions were assigned for both channel and porous media walls. While the outlet boundary was held 0 kPa, a mass flow rate was specified (\dot{m}_{in}) at the inlet. The accuracy of the simulation results is limited by numerical errors due to the discretization of space grids, employed simplifications and assumptions, and imprecision of input parameters. However, the mathematical model predicts experimental data, with a maximum error of 4%.

3.2.3 Power analysis

Power analysis for strip cell is conducted comparing the current at 0.2 V (i_{lim}) and pressure drop on a power basis. Cell power and pump power are calculated using equations 3.3 and 3.4 for all strip cell configurations:

$$P_{cell} = i_{lim} \times V_{@i_{lim}} \times A \quad (3.3)$$

$$P_{pump} = \Delta P \times V_f \quad (3.4)$$

where i_{lim} is limiting current, $V_{@i_{lim}}$ is voltage at limiting current, A is active area, ΔP is pressure drop, V_f is volumetric flow rate. Table 3.2 includes the data used for this analysis.

3.3 Results and discussion

Although CFD is a well-developed, robust numerical simulation of fluid flow, it still relies on experimental validation. Pressure drop measurement is a straightforward verification and has often been used for partial model verification. However, pressure drop

discrepancy between experiments and models is a common issue as has been reported in many studies in VRFB literature [26,101]. Kumar et al. attributed this discrepancy to carbon felt electrode intrusion into the channel volume due to compression [101]. However, for the relatively thin carbon paper electrode employed in this work, such intrusion can be considered insignificant. It was observed that non-negligible pressure drop was present in the inlet and outlet tubes located between pressure transducers and the VRFB cell. This pressure drop caused a significant discrepancy between experimental results and the model. To clarify and overcome this issue, inlet and outlet manifold tubes (0.3 m) were included in the simulation domain as seen in Figure 3.1. The pressure drop due to elbows in the inlet and outlet was also considered even though their contribution was small. Thus, the model accurately represents the entire experimental system. The pressure drop measured across the entire physical domain is defined as overall pressure drop. Computationally predicted and experimentally measured overall pressure drops [1,4] were compared for all strip cell configurations (0.25, 0.50, 1.00, and 2.50 mm) and a range of flow rates from 10 mL min⁻¹ up to 50 mL min⁻¹ in Figure 3.2. Good agreement has been achieved between the numerical predictions and the experimental measurements with maximum error of 4%. It has been reported in previous work that enhanced electrochemical performance and relatively uniform current density distribution can be attributed to increased convective flow in the porous electrode [1]. Figure 3.3a-d shows predicted electrolyte velocities at the midline of a channel and adjacent electrode for all strip cell configurations (0.25, 0.50, 1.00, and 2.50 mm depth) and flow rates (10, 20, 30,

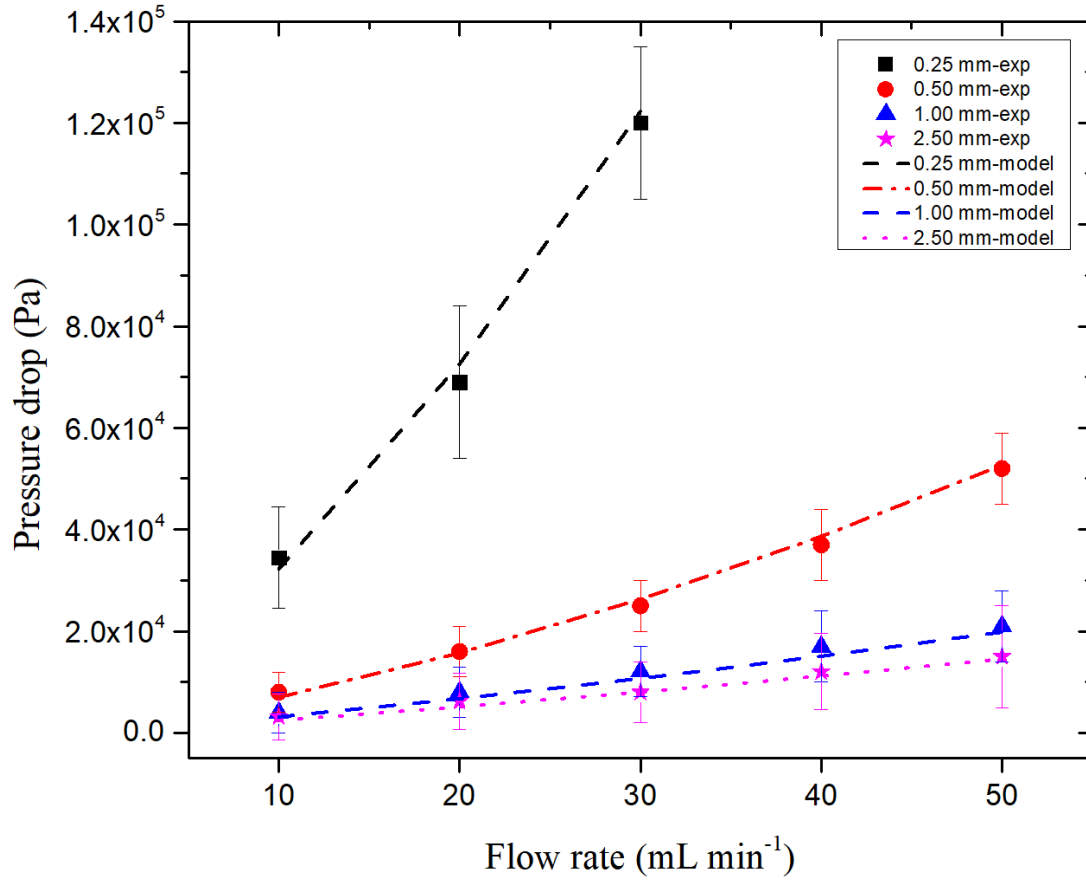


Figure 3.2 Computationally predicted and experimentally measured pressure drops through the strip cell, including inlet and outlet manifold pipes. Error bars reflect both pulsing from the peristaltic pump and experimental variability.

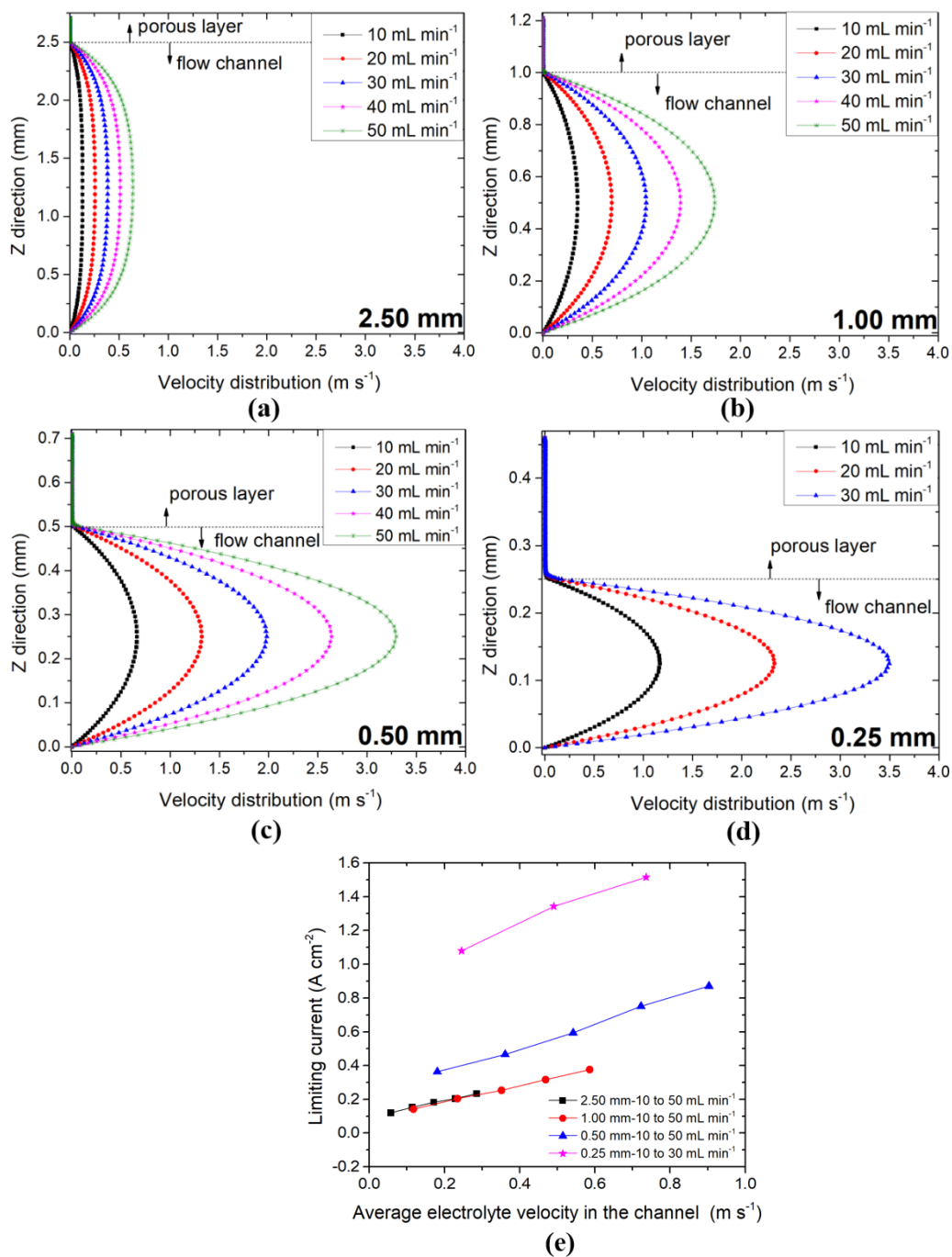


Figure 3.3 Predicted electrolyte velocity distribution at a cut line in the center of the electrode and channel domain (a) 2.5 mm (b) 1 mm (c) 0.50 mm (d) 0.25 mm and (e) correlation between average channel velocity and measured limiting currents.

40, 50 mL min⁻¹). Since velocity in the electrode was much smaller than in the channel, a magnified view of the fluid velocity in the porous layer is included in Figure 3.4a-d. It is clear that electrolyte velocities both in the channel and electrode change as a function of channel depth and flow rate; more shallow cell configurations at elevated flow rates have the highest average velocities. Computationally predicted average electrolyte velocities both in channel and electrode are tabulated in Table 3.2. These velocities were obtained by averaging the surface on the midplane of a channel and adjacent electrode.

In addition to electrolyte flow results, Table 3.2 also shows experimentally measured maximum current densities at 0.2 V hold. While the electrochemical performance of the cell was directly proportional to the electrolyte velocity in the electrode, there was no detectable, direct correlation between electrolyte velocity in the channel and electrochemical performance. Figure 3.3e and Figure 3.4e show the average channel velocity/maximum current density and average electrode velocity/maximum current density correlations respectively. Even though the electrolyte velocities in the electrode were much smaller than the velocities in the channel, a small enhancement of velocity in the electrode yielded significant electrochemical performance improvement. According to Faraday's second law of consumption and production of species, the quantity of reactant consumed is directly proportional to the charged passed [99]. In VRFB literature, volumetric electrolyte penetration into the electrode is usually assumed as an amount of reactant consumed under limiting conditions [41,44,85]. Thus, greater electrolyte penetration into the electrode corresponds to greater electrolyte velocity in the electrode; higher current is generated in the cell as a result. This effect occurs because increased

velocity in the electrode reduces the diffusion boundary layer thickness around the fiber surfaces, enhancing maximum transport rates to the reaction surface [49]. Rapidly replenished fresh electrolyte also lowers concentration polarization in the electrode. This allows cells to operate at a higher current density with more uniform current distribution. However, mass transport in the electrode is limited by the diffusion resistance between the liquid electrolyte and the fiber surfaces at the pore level, even at very high electrolyte velocity in the electrode; this resistance can be mitigated but never completely removed. Figure 3.4e illustrates that, as electrolyte velocity in the electrode increases, the relative increase in current density attenuates, and the rate of increase in limiting current gradually flattens out. Additional data were not possible for higher velocities or shallower channels due to excessive pressure drop; but it is clear that maximum limiting current is a direct function of electrolyte velocity in the electrode (e.g. reactant convection). Up to that maximum current, however, increased electrolyte velocity in the electrode improves the electrochemical performance; the current distribution also becomes more uniform, an indicator of sufficient mass transport to the electrode surfaces.

Figure 3.5 shows the impact of electrolyte velocity on the current distribution at 50% SOC for selected flow rate/channel depth configurations. These configurations were chosen among eighteen different flow rate/channel depth combinations to demonstrate current distribution variations more clearly. Figure 3.5a shows absolute local current distribution as a scatter plot, while the contour plots in Figure 3.5b show percent deviation from the average current. Although the impact of increased electrolyte velocity on measured local current is apparent in Figure 3.5a, relative differences in current down the

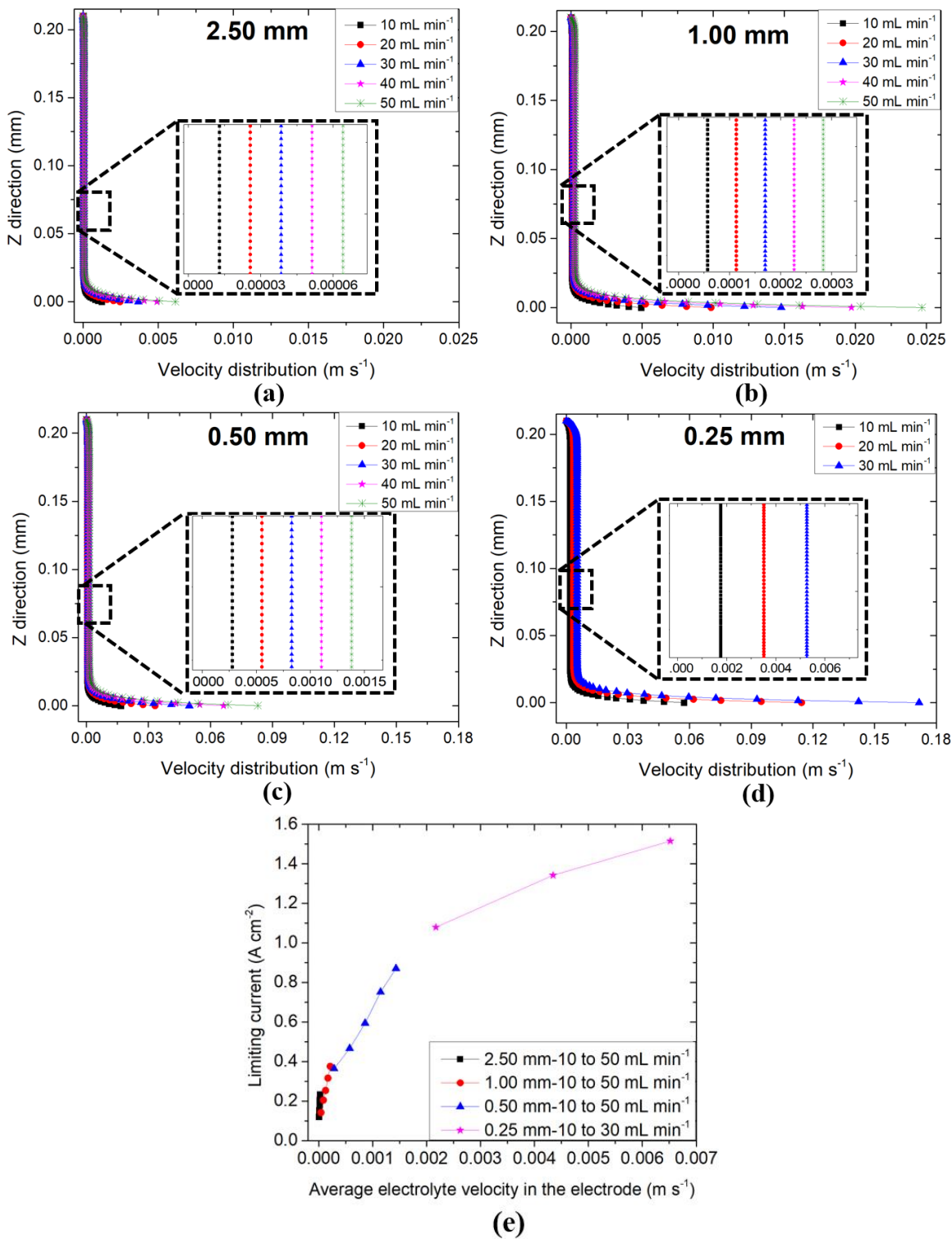


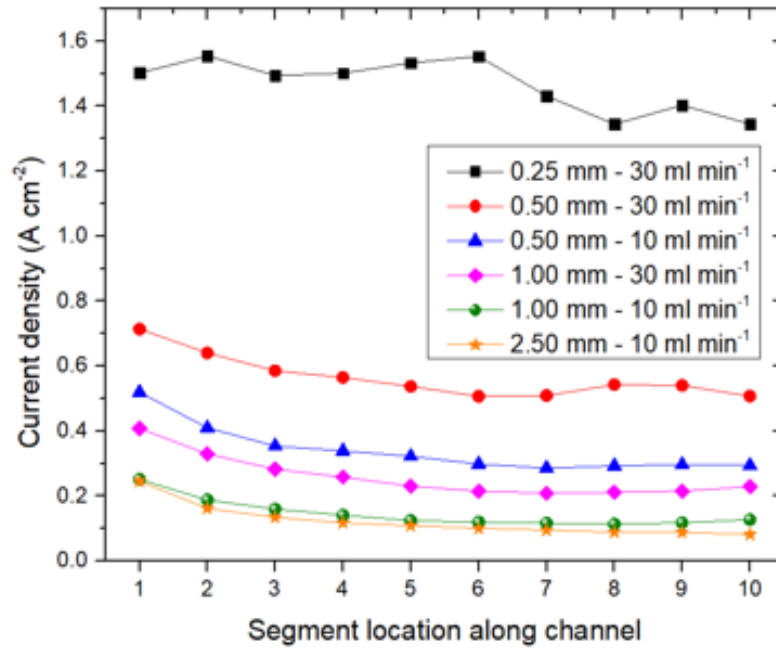
Figure 3.4 Magnified view of predicted electrolyte velocity distribution in the electrode (a) 2.50 mm (b) 1.00 mm (c) 0.50 mm (d) 0.25 mm and (e) correlation between average electrode velocity and measured limiting currents.

Table 3.2 Selected parameters for the range of channel depths and flow rates considered in this work. Limiting current is the current achieved at 0.2 V discharge for a 50% SOC electrolyte.

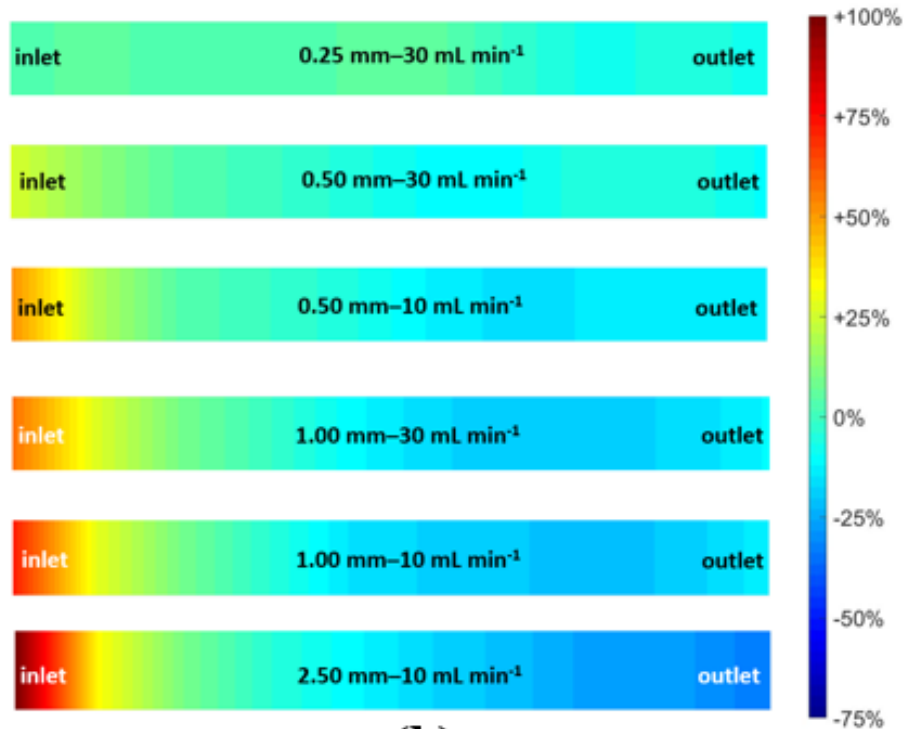
Channel depth (mm)	Flow rate (mL min ⁻¹)	Average velocity in the channel (m s ⁻¹)	Average velocity in the electrode (m s ⁻¹)	Limiting current (A cm ⁻²)	Average local pressure drop (Pa)	Overall pressure drop (Pa)
2.5	10	0.057013	4.85x10 ⁻⁶	0.1291	18.8	2433
	20	0.11402	9.71 x10 ⁻⁶	0.1528	37.7	5114
	30	0.17104	1.45 x10 ⁻⁵	0.1825	56.6	8029
	40	0.22805	1.94 x10 ⁻⁵	0.2044	75.5	11167
	50	0.28505	2.42 x10 ⁻⁵	0.2337	94.4	14510
1.00	10	0.11723	4.27 x10 ⁻⁵	0.1419	82.8	3157
	20	0.23446	8.55 x10 ⁻⁴	0.2044	165.6	6726
	30	0.35169	1.28 x10 ⁻⁴	0.2633	248.3	10693
	40	0.46892	1.71 x10 ⁻⁴	0.3161	331.1	15065
	50	0.58612	2.14 x10 ⁻⁴	0.3754	414.1	19838
0.50	10	0.18066	2.86 x10 ⁻⁴	0.3638	402.3	6992
	20	0.36131	5.73 x10 ⁻⁴	0.5424	803.8	15725
	30	0.54197	8.60x10 ⁻⁴	0.5939	1205.5	26307
	40	0.72263	1.15x10 ⁻³	0.7513	1607.4	38666
	50	0.90325	1.43 x10 ⁻³	0.8704	2010.2	52679
0.25	10	0.24549	2.17 x10 ⁻³	1.0791	2537.1	32264
	20	0.49097	4.35 x10 ⁻³	1.342	5071.1	72569
	30	0.73646	6.52 x10 ⁻³	1.5150	6340.3	122290

channel are less clear due to the different current scales. Thus, current measured in each segment was normalized to the average current for any configuration to quantify current distribution down the channel. It is clearly seen in Figure 3.5b that the current distribution down the channel became relatively uniform as electrolyte velocity in the electrode increased. While the lowest predicted velocity in the electrode (2.5 mm channel depth at 10 mL min⁻¹) had the largest current deviation (+102% to -33%), the highest predicted velocity in the electrode (0.25 mm channel depth at 30 mL min⁻¹) had the lowest current deviation (+2% to -8%) from inlet to outlet. Nonuniform current distribution has been reported in recent studies in VRFB literature. Houser et al. attributed different current distribution patterns for serpentine and interdigitated flow field designs to disparate velocity gradients in the electrode [26]. However, variations in the electrolyte velocity in the electrode for a strip cell are negligibly small; thus, the velocity gradients in Houser et al [21] can be attributed to higher order behaviors not present in the 1-D strip cell. Figure 3.6 shows predicted velocity distribution in the electrode for all channel depths (0.25, 0.50, 1.00, and 2.50 mm) at 30 mL min⁻¹ flow rate. Velocity distributions down the channel for all channel depths were highly uniform. Thus, the large current gradients for experiments with low fluid velocity are attributed to local concentration depletion in the electrode; such concentration depletion leads to diffusion limitation. A natural next step, then, is calculation of active species concentration down the channel in the electrode region.

It has been shown that the electrochemical performance and current distribution can be correlated to the hydrodynamics in the electrode. Development of a correlation between pressure drop and electrochemical performance is thus of interest, since overall pressure



(a)



(b)

Figure 3.5 Measured local current (a) and (b) normalized current distribution comparisons at 50% SOC, 30mL/min, 0.2V hold.

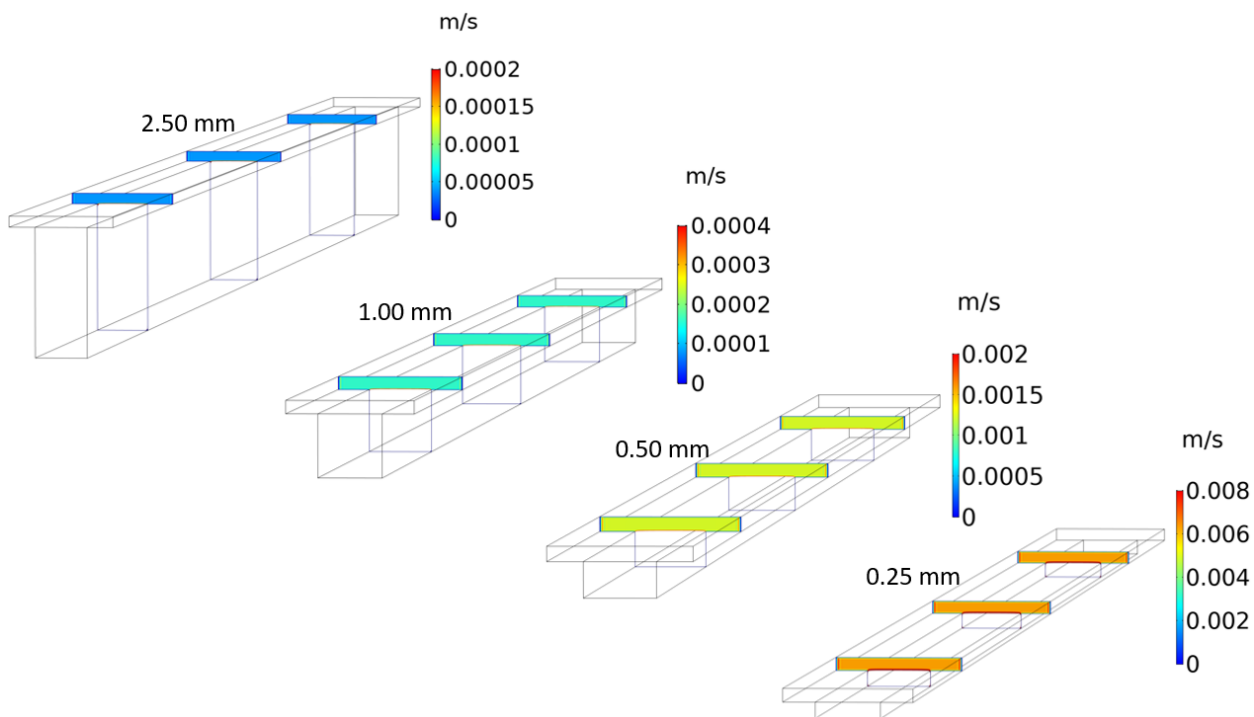


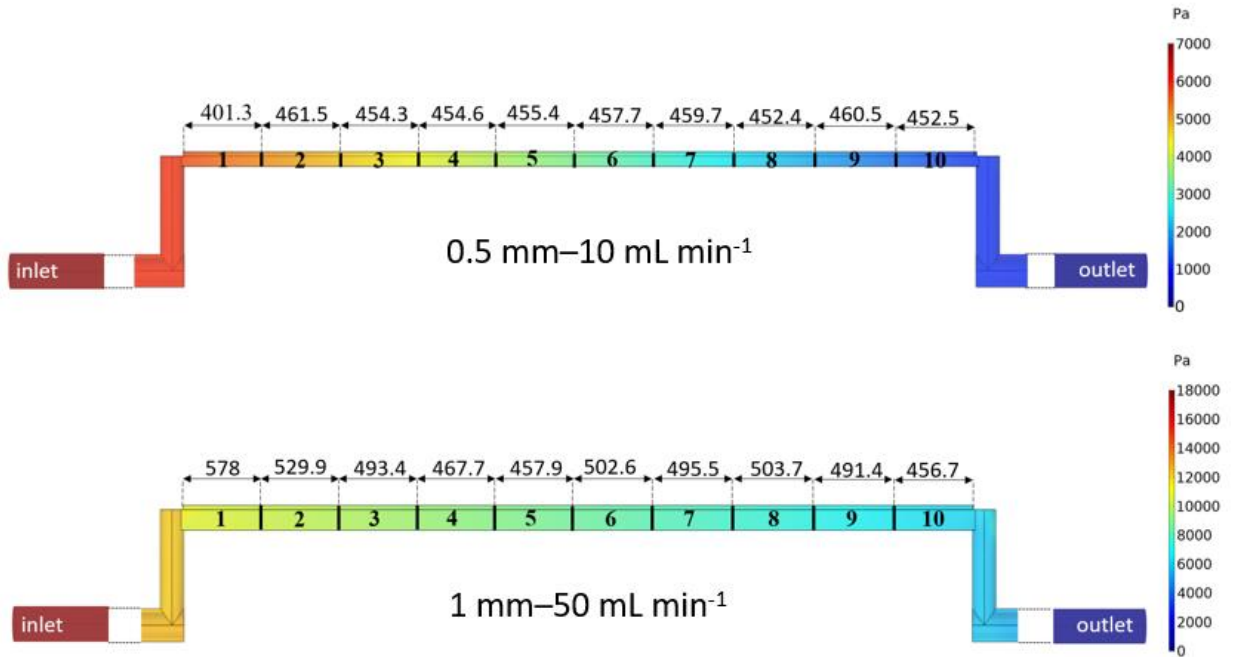
Figure 3.6 Predicted electrolyte velocity distribution at a cut plane through the electrode domain for all channel depths at 30 ml min^{-1} flow rate.

drop is the primary drawback to increased flow rates, which are known to enhance performance. Achieving enhanced velocity in the electrode (and thus mass transport via convection) with minimal increases in overall cell pressure drop is a potential avenue to greater overall efficiency. Understanding this correlation is essential to maximize net system efficiency due to the existence of parasitic pumping losses. Table 3.2 shows both experimentally measured maximum current densities and computationally predicted overall pressure drops for all channel depths and flow rates in this study. It can be noted that two configurations, 0.5 mm-10 mL min⁻¹ and 1.0 mm-50 mL min⁻¹, yielded very similar electrochemical performance. While the channel depths, flow rates, and predicted overall pressure drops (6,992 Pa and 17,917 Pa) were quite different, these two configurations yielded very similar electrode fluid velocity (1.26×10^{-4} m s⁻¹ and 1.71×10^{-4} m s⁻¹) and, as hypothesized, very similar current density (0.3638 and 0.3754 A cm⁻²) at the given condition. This result indicates that to some degree, performance can be enhanced while suffering a minimal pressure drop penalty using optimized architecture and operating parameters.

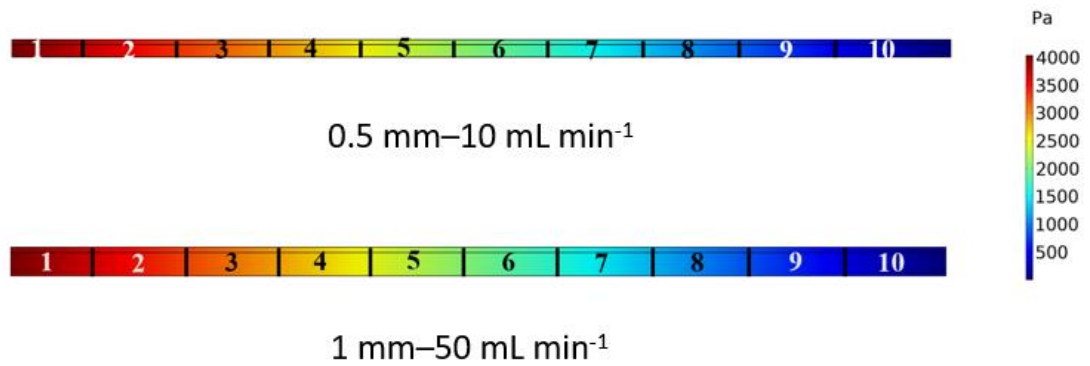
To investigate this pressure drop discrepancy and understand the relationship between pressure drop and electrochemical performance, computationally predicted pressure distributions for these configurations are compared in Figure 3.7. Figure 3.7a shows pressure distribution from inlet to outlet, including elbows and plumbing tubes. While the color code stands for the pressure gradient from inlet to outlet, arrows indicate the local pressure drop defined as the pressure drop through each individual segment down the channel. The pressure gradient for the configuration with 0.5 mm-10 mL min⁻¹ appears

qualitatively steeper than the pressure gradient for $1.0 \text{ mm-}50 \text{ mL min}^{-1}$ at the channel/electrode region. However, it should be noted that these configurations have different pressure scales. Local pressure drops indicate that the pressure gradient is very similar down the channel for these configurations. The average local pressure drop is predicted to be 436 Pa and 525 Pa for the configurations with $0.5 \text{ mm-}10 \text{ mL min}^{-1}$ and $1.0 \text{ mm-}50 \text{ mL min}^{-1}$, respectively. For another perspective on this behavior, CFD simulations were performed excluding the elbows and plumbing tubes, effectively capturing only the channel-electrode region, and called “simplified geometry” here. Figure 3.7b shows that the pressure gradient from channel inlet to outlet is identical for both configurations. Although the average local pressure drop for the simplified geometries is underpredicted (402 Pa and 414 Pa), it indicates that the local pressure drop in the complete system is primarily caused by a combination of flow rate and channel depth, as would be expected. The overall pressure drop discrepancy between the two configurations is thus attributed to pumping different flow rates (10 mL min^{-1} and 50 mL min^{-1}) through the same manifolding before and after the active area.

The local pressure drop (for simplified geometries) for all flow rates and channel depths are tabulated in Table 3.2. It is found that the local pressure drop is also directly proportional to the electrode velocity as seen in Figure 3.8a. This correlation indicates that the local pressure drop is the driving force for electrolyte to penetrate into the electrode region. It is also seen in Figure 3.8a that shallower channels instigate electrolyte penetration more effectively than deeper channels. Considering a fixed local pressure drop (e.g. 3×10^3 Pa) for all channel depths, it is possible to achieve three times greater electrode velocity by



(a)



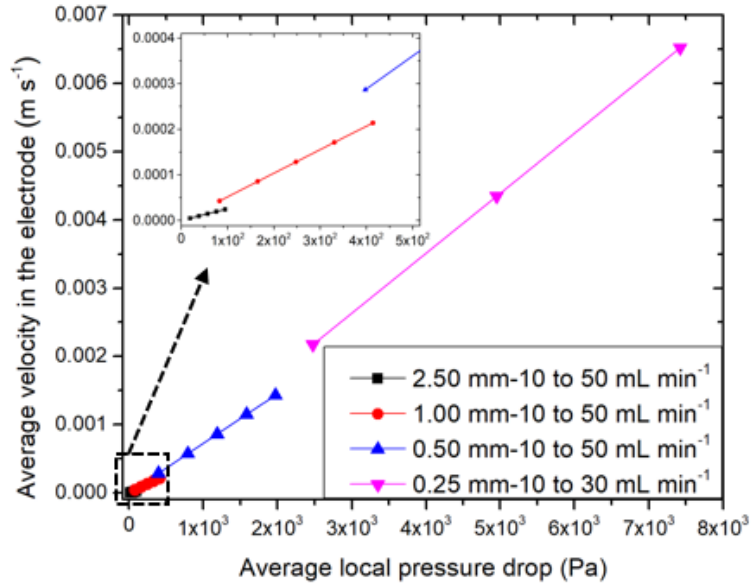
(b)

Figure 3.7 Predicted pressure drop distribution for (a) complex and (b) simplified geometries.

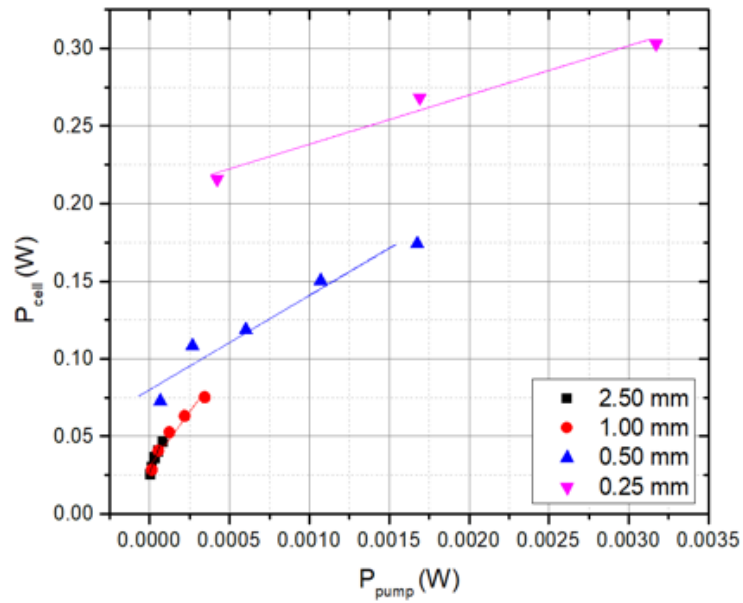
employing the shallowest channel configuration. This observation is more perceptible via the power analysis shown in Figure 3.8b. It is seen that shallower channels have higher cell power output with lower pumping power input. Again, considering the fixed pumping power input (0.0004 W) for all channel depths, 0.25 mm channel depth at 10 mL min^{-1} (with 0.215 W) shows approximately three times higher cell power output than the 1 mm depth at 50 mL min^{-1} (0.075 W). Calculated pump power input and cell power output for all strip cell configurations are tabulated in Table 3.3. A similar analysis has been conducted by others [27].

On the other hand, there is no direct relationship evident between local pressure drop and average channel velocity as seen in Figure 3.9a. Figure 3.9b and 3.9c show local pressure drop-current and overall pressure drop-current correlations, respectively. As expected, the local pressure drop-current correlation in Figure 3.9b is very similar to the average velocity-current correlation in Figure 3.4e. Figure 3.9c indicates that the pressure drop arising due to any fluid path outside the channel-electrode region (e.g. external plumbing) does not contribute to the current and must be minimized to improve overall system efficiency of the VRFB cell.

It can be concluded that improved VRFB electrochemical performance can be achieved by optimizing the tradeoff between pressure drop and in-electrode velocity of the electrolyte. Deeper channels are found to be less effective at increasing convection in the electrode, even at higher flow rates in the range studied here (up to 50 mL/min/cm^2). Additionally, the overall pressure drop needed to achieve high electrolyte penetration in the electrode is much greater for deeper channels than shallower channels. Considering the



(a)



(b)

Figure 3.8 Correlations between (a) local pressure drop and average channel velocity (b) Cell power output and pump power input comparison for all strip cell configurations.

Table 3.3 Calculated pump power input and cell power output for all strip cell configurations.

Channel depth (mm)	Flow rate (mL min⁻¹)	Pump power input, P_{pump} (W)	Cell power output, P_{cell} (W)
2.5	10	3.13334E-6	0.02582
	20	1.25667E-5	0.03056
	30	2.83001E-5	0.0365
	40	5.03334E-5	0.04088
	50	7.86668E-5	0.04674
1.00	10	1.38E-5	0.02838
	20	5.52001E-5	0.04088
	30	1.2415E-4	0.05266
	40	2.20734E-4	0.06322
	50	3.45084E-4	0.07508
0.50	10	6.70501E-5	0.07276
	20	2.67934E-4	0.10848
	30	6.02751E-4	0.11878
	40	0.00107	0.15026
	50	0.00168	0.17408
0.25	10	4.22851E-4	0.21582
	20	0.00169	0.2684
	30	0.00317	0.303

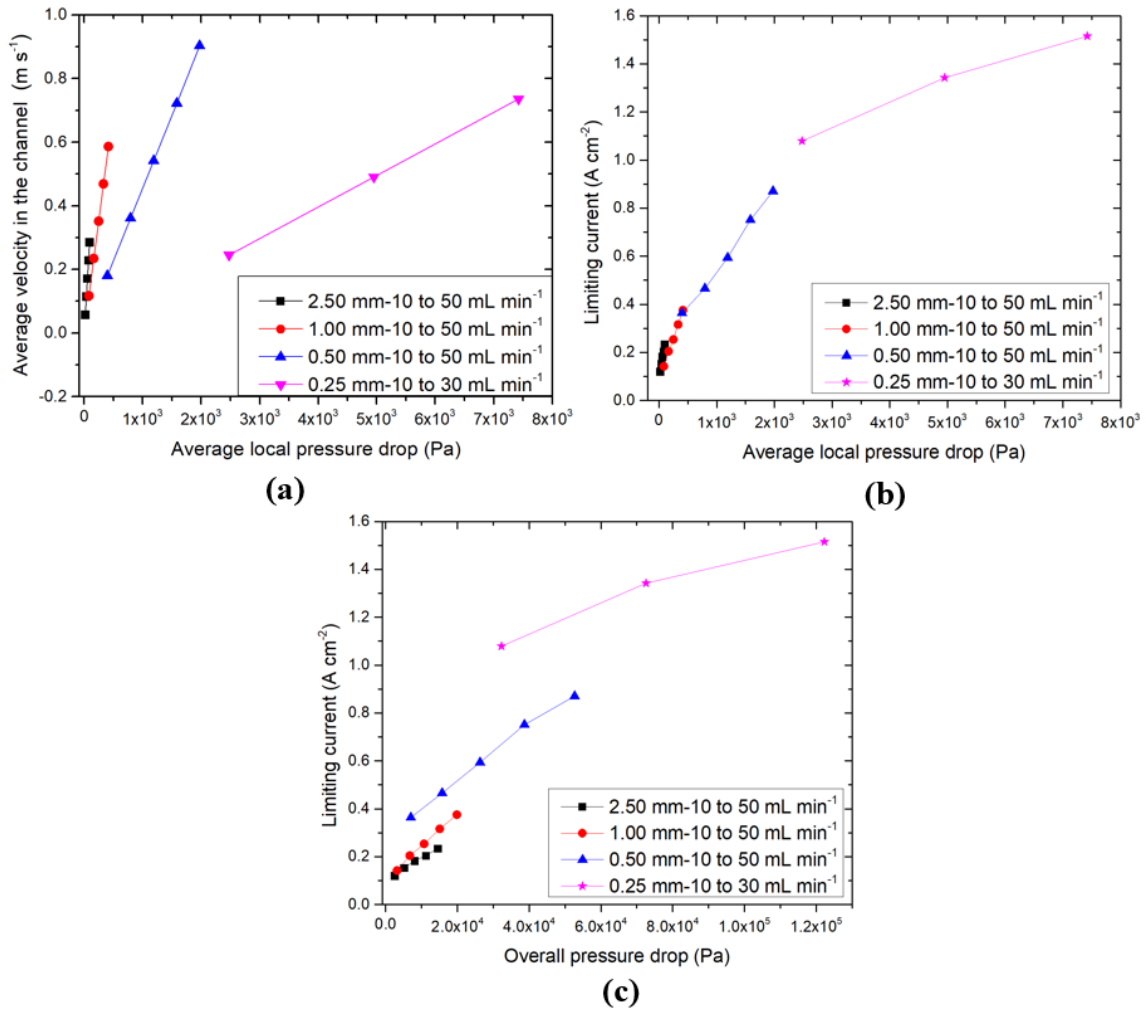


Figure 3.9 Correlations between (a) local pressure drop and average electrode velocity (b) average local pressure drop and limiting current (c) overall pressure drop and limiting current.

manifolding needed for VRFB stack application, operating at lower flow rates can significantly decrease parasitic pumping losses. It is also observed that the pressure drop suffered in the channel is effectively wasted because electrochemical performance is shown to not correlate to the channel velocity. Thus, flow fields and electrodes should be designed to enable maximum electrolyte velocity in the electrode with minimal overall pressure drop; shallow channels are one avenue to this goal.

3.4 Conclusions

Convection in the electrode is a critical mechanism for rapid transport of active species to/from the reaction surfaces in a high performance VRFB. Thus, the impact of convection on electrochemical performance and pressure drop must be understood to achieve enhanced electrochemical performance while minimizing pumping losses. The simple 1-D strip cell design employed for this study minimizes local pressure drop variations and achieves relatively uniform electrolyte velocity distribution down the channel, and is thus configured to provide precise benchmark data. A range of electrolyte velocities inside the cell was achieved by employing various channel depths (0.25, 0.5, 1, 2.5 mm) and flow rates (10-50 mL min⁻¹). Velocity and pressure drop distributions down the channel were predicted via CFD simulation while localized current distribution was measured. It was found that the experimentally-measured maximum current for each configuration scaled linearly with the predicted electrode-region average fluid velocity. However, there was no direct correlation seen between electrolyte velocity in the channel and the limiting current. Increasing local electrolyte velocity in the electrode facilitates active species transport, reducing the diffusion boundary layer thickness around the fiber

surfaces. This insight guides design for enhancing flow into the electrodes. Employing shallow channels is a practical way to improve convective flow in the electrode while suffering a comparatively moderate pressure drop penalty. It is demonstrated that there is a point where electrochemical current cannot be improved, which is likely due to the existence of diffusion resistance between the liquid electrolyte and the fiber surfaces at the pore level. Current distribution tests indicate that increased electrolyte velocity limits local mass transport limitations in the electrode, resulting in more current uniformity down the channel. Although the electrolyte velocity distribution in the electrode is homogeneous, high current deviations are observed from inlet to outlet for experiments with low fluid velocity. Local concentration depletion in the electrode is speculated to be responsible for these large current gradients. As a result of this work, prediction of electrolyte velocity in the electrode can be correlated with experimentally-measured current distribution; modeling work can thus focus on linking local properties in the electrode (e.g. concentration and fluid velocity) to electrochemical performance.

Chapter 4 Vanadium Flow Battery Electrochemistry and Fluid Dynamics Model in-situ Current Distribution Validation

Abstract

This chapter was presented at the 238th Electrochemical Society PRIME Meeting in 2020 [102]. The full paper will be submitted for publication under the same authorship.

Ertugrul, T. Y., Daugherty, M., Aaron, D., and Mench, M. M. “**Vanadium Flow Battery Electrochemistry and Fluid Dynamics Model with In-Situ Current Distribution Validation**” *ECS Meeting Abstracts* MA2020-01, no. 3 (2020): 473–473.
doi:10.1149/ma2020-013473mtgabs

My contribution to this work were, collection, reduction, and analysis of data as well as composition of the manuscript. Daugherty assisted with data collection. Aaron and Mench assisted in analysis of data and composition of the manuscript.

4.1 Introduction

The VRFB is a complex system with multiple interrelated parameters (especially mass transport and electrochemical reactions) affecting electrochemical cell performance; these interrelated parameters are difficult to disentangle experimentally. Comprehensive and suitably validated mathematical simulations can both help to understand complex phenomena inside VRFBs and provide practical knowledge for controlling and optimizing VRFB systems. In this study, a three dimensional, steady-state multi-physics model is developed for VRFBs with strip cell architecture under the dilute solution theory assumption. The simulation domain includes a central membrane, both electrodes, flow plates, and current collectors. Continuum relationships including conservation of mass, momentum, species and charge coupled with Butler-Volmer kinetics are employed.

Polarization curve analysis and fully segmented, printed circuit board (PCB)-based, localized current distribution measurements are employed to validate the mathematical

model. In-situ current distribution measurements is employed for validation for the first time in the VRFB literature. All tests are conducted with a simplified test bed with a segmented strip cell architecture, having only one straight channel and a total of 1 cm² active area. Strip cell architecture effectively eliminates higher-dimensional behaviors (e.g. channel hopping, bypass at channel switchbacks, and potential fluid short circuits) and provide straightforward systems for phenomenological as well as comparative and detailed model validation studies [2,103].

The impacts of various electrochemical and transport parameters on the electrochemical performance and current distribution are investigated. It is found that the electrode permeability and the diffusion coefficient of the vanadium species are the most influential parameters affecting both electrochemical performance and the current distribution along the channel. While the model successfully predicts both the charge-discharge polarization curve and the current distribution with the fitted diffusion coefficient parameter, computationally predicted current distribution fails for fitted permeability parameter. The diffusion coefficient of the vanadium species was found to be order of magnitude higher than the experimentally-measured values found in the literature [104].

4.2 Materials and methods

4.2.1 Experimental

4.2.2 Multiphysics model

Three dimensional, steady-state multi-physics model is developed for VRFB strip cell architecture under the dilute solution theory assumption. The simulation domain

includes membrane, electrodes, flow plates and current collectors as seen in Figure 4.1. Continuum equations: conservation of mass, momentum, species, and charge coupled with Butler-Volmer kinetics are employed.

Electrolyte flow in the channel and the electrode are described by the conservation of mass and momentum equations. Navier-Stokes equations (Eqs. 3.1) represent the fast flow in the channel and the Brinkman equations model the flow in porous media (Eqs. 3.2). No-slip boundary conditions were assigned for channels, porous media walls. While the outlet boundaries were held 0 kPa, a mass flow rate was specified (\dot{m}_{in}) at the inlets.

The ion flux and charge transport in the electrode is governed by the Nernst-Planck equations. Diffusion, migration and convection are the main mass transport mechanisms.

$$N_i = -D_i \nabla c_i - z_i u_{mob,i} F c_i \nabla \phi_l + c_i u \quad (4.1)$$

where c_i is the concentration, D_i is the diffusion coefficient, z_i is the species charge number, $u_{mob,i}$ is the species mobility, F is the Faraday's constant, (ϕ_l) is the electrolyte potential, u is the fluid velocity vector. Nernst-Planck equations are solved for species; V^{2+} , V^{3+} , H^+ at the negative electrode, VO_2^+ , VO^{2+} and H^+ at the positive electrode.

Bruggeman correlation is used to calculate effective diffusivity in the porous media. ε is the porosity of the electrode.

$$D_i^{eff} = D_i \varepsilon^{3/2} \quad (4.2)$$

The ionic mobility u_{mob} is evaluated by using Nernst-Einstein relation under the dilute solution approximation.

$$u_{mob,i} = \frac{D_i^{eff}}{RT} \quad (4.3)$$

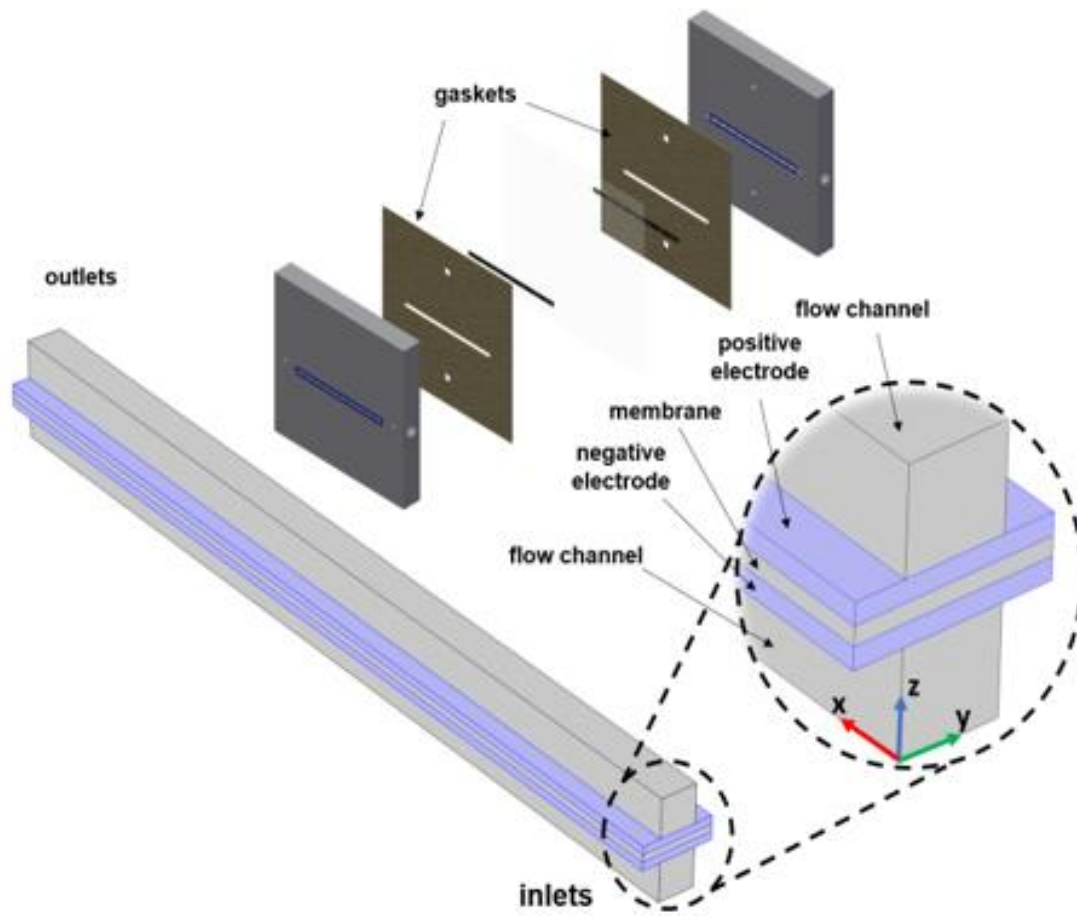


Figure 4.1 Simulation domains with channels, electrodes, and membrane

The liquid electrolyte (ionic) current density is calculated using Faraday's law by summing up the contributions from the molar fluxes, multiplied by the species charges. The convective term vanishes due to the electroneutrality condition.

$$i_l = F \sum_{i=1}^n z_i (-D_i^{eff} \nabla c_i - z_i u_{mob,i} F c_i \nabla \phi_l) \quad (4.4)$$

Ionic current at the liquid phase and electronic current at the solid phase are coupled through the conservation of charge:

$$\nabla \cdot i_l = -\nabla \cdot i_s = i \quad (4.5)$$

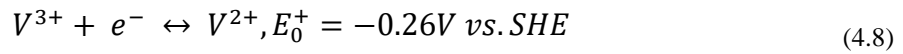
where i_l denotes ionic current at the liquid phase, i_s represents electronic current at the solid phase. The electronic potential ϕ_s is then calculated using the Ohm's law

$$i_s = \sigma_s^{eff} \phi_s \quad (4.6)$$

$$\sigma_s^{eff} = (1 - \varepsilon)^{3/2} \sigma_s \quad (4.7)$$

where σ_s is the solid material conductivity and σ_s^{eff} is the effective conductivity calculated using the Bruggeman correlation.

The negative electrolyte contains V^{3+} , V^{2+} , and H^+ ions and the negative electrode reaction is:



The equilibrium potential for this reaction is calculated using Nernst equation.

$$E_{eq,neg} = E_{0,neg} + \frac{RT}{F} \ln \left(\frac{c_{V^{3+}}}{c_{V^{2+}}} \right) \quad (4.9)$$

Considering the proton concentration at the negative side: [80]

$$E_{eq,neg} = E_{0,neg} + \frac{RT}{F} \ln \left(\frac{c_{V^{3+}} \cdot c_{H^+}^-}{c_{V^{2+}}} \right) \quad (4.10)$$

where $E_{0,neg}$ is the reference potential for the electrode reaction c_i is the concentration of the electroactive species i , R is the molar gas constant T is the temperature, and F is the Faraday's constant. A Butler-Volmer type of kinetics expression is used for the negative electrode reaction.

$$i_{neg} = A i_{0,neg} \left(e^{\frac{(1-\alpha_{neg})F\eta_{neg}}{RT}} - e^{-\frac{\alpha_{neg}F\eta_{neg}}{RT}} \right) \quad (4.11)$$

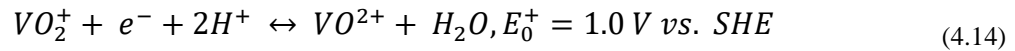
$$i_{0,neg} = F k_{neg} (\alpha_{V^{2+}})^{1-\alpha_{neg}} (\alpha_{V^{3+}})^{\alpha_{neg}} \quad (4.12)$$

where A is the specific surface area of the porous electrode, α_{neg} is the transfer coefficient, k_{neg} the rate constant. The overpotential, η_{neg} is defined as

$$\eta = \phi_s - \phi_l - E_{eq} \quad (4.13)$$

where ϕ_s is the solid phase electric potential of the electrode, ϕ_l is the liquid phase electrolyte potential. The positive electrolyte contains VO_2^+ , VO^{2+} and H^+ ions.

The positive electrode reaction is:



with the equilibrium potential calculated:

$$E_{eq,pos} = E_{0,pos} + \frac{RT}{F} \ln \left(\frac{c_{VO_2^+}}{c_{VO^{2+}}} \right) \quad (4.15)$$

Considering the proton concentration at the positive side: [80]

$$E_{eq,pos} = E_{0,pos} + \frac{RT}{F} \ln \left(\frac{c_{VO_2^+} \cdot (c_{H^+})^2 \cdot c_{H^+}}{c_{VO^{2+}}} \right) \quad (4.16)$$

$$i_{pos} = Ai_{0,pos} \left(e^{\frac{(1-\alpha_{pos})F\eta_{pos}}{RT}} - e^{\frac{-\alpha_{pos}F\eta_{pos}}{RT}} \right) \quad (4.17)$$

$$i_{0,pos} = Fk_{pos}(\alpha_{VO^{2+}})^{1-\alpha_{pos}}(\alpha_{VO_2^+})^{\alpha_{pos}} \quad (4.18)$$

4.3 Results and discussion

Computational simulations require some degree of validation and experimental open circuit voltage is a partial model validation in VRFB literature. To predict experimentally measured OCV, two versions of Nernst equation: the standard form of the Nernst equation (Eqs. 4.9 and 4.15) and the complete form of the Nernst equation (Eqs. 4.10 and 4.16) are employed in this study. The standard form of the Nernst equation considers the vanadium ions (V^{2+} , V^{3+} , VO_2^+ , VO^{2+}) as reduced and oxidized species. Figure 4.2 compares experimentally measured OCV and computationally predicted OCV as a function of state of charge (SoC). As seen, standard form of the Nernst Equation underestimates the experimental OCV with an average error of 12%. The discrepancy at 50% SOC is calculated as 173 mV. This discrepancy is attributed to the incomplete description of the electrochemical double layer [80]. The complete description of the Nernst equation incorporates proton activity at the positive electrode and unequal proton concentration across the membrane (Donan potential). Although, the complete Nernst equation estimates better than standard Nernst equation, it still deviates 86 mV from experimental OCV at 50% SOC. Since all tests are conducted at 50% SoC, fitting voltage (86 mV) is added to the predicted voltage outputs in order to account unknown discrepancies with the experimental data.

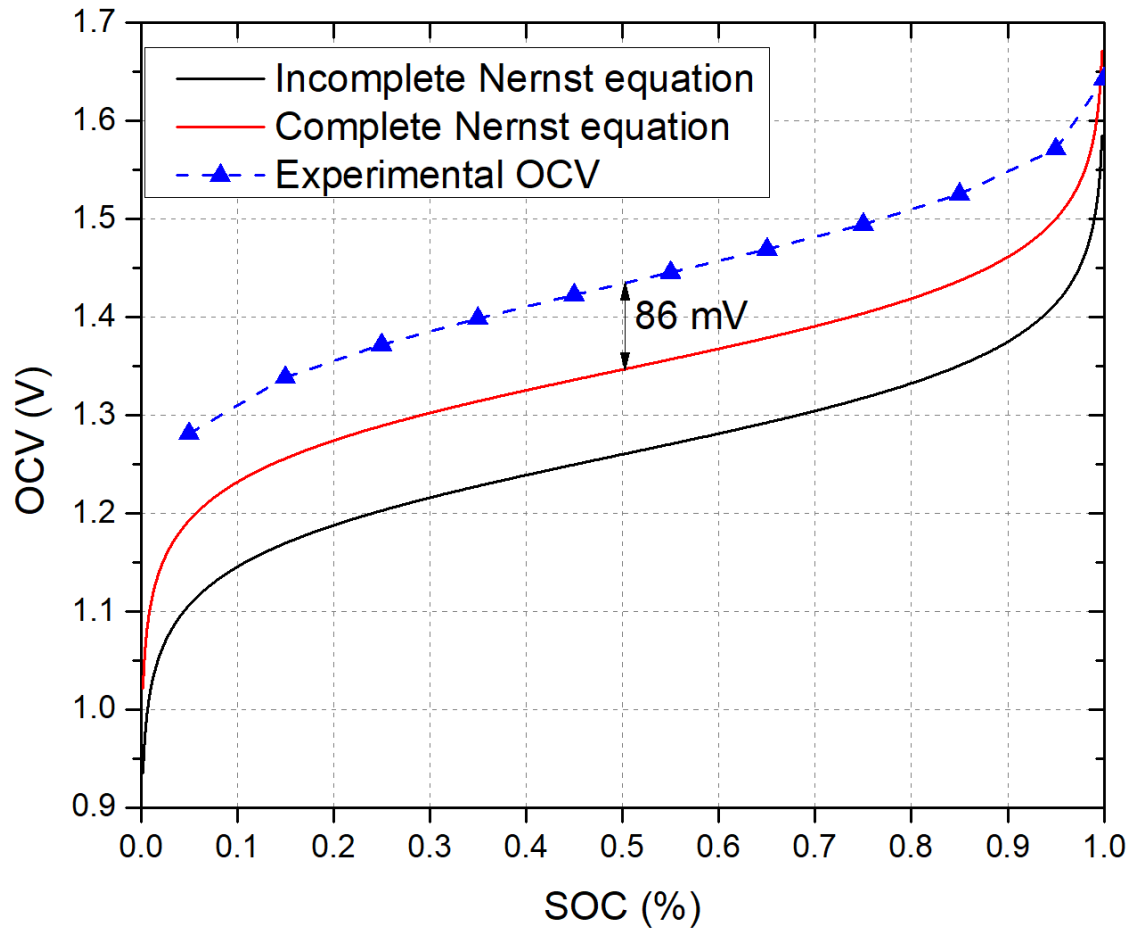


Figure 4.2 The comparison of experimentally measured and computationally predicted open circuit voltage (OCV) for

Polarization curve analysis is a common method to evaluate cell performance in electrochemical devices. In this study, polarization curve analysis is employed to validate numerical results. Polarization curve data for both experimental tests and mathematical simulations are obtained sweeping the cell voltage between 1.7 V to 0.2 V. However, converged solution below 0.6 V is not possible for simulations due to the numerical limitations. While the experimental data is obtained with 0.1 V voltage interval, simulation data is recorded with 0.05 V voltage interval. Figure 4.3 shows experimentally measured charge-discharge polarization curve and computationally predicted polarization curves for 1mm depth channel strip cell at 50% SOC and 30 mL min⁻¹ flow rate. The polarization curve shown with the red color and the circular shape represents the base model employing kinetic and transport parameters tabulated in Table 4.1 and Table 4.2. This model drastically underestimates experimentally measured polarization curve. Although, adding 86 mV fitting voltage, improves the prediction of the simulation (blue rectangular data), there is still huge discrepancy between experimentally measured and computationally predicted polarization curves. Predicted current density for all voltage points on the polarization curve is much less than experimentally measured current density. This is most likely due to the unsuccessful simulation of reaction kinetics or mass transport at the electrodes. To elucidate this, wide range of kinetic and mass transport parameters are investigated. It is found that electrode permeability and diffusion coefficient of vanadium are the most influential parameters impacting electrochemical performance and distribution.

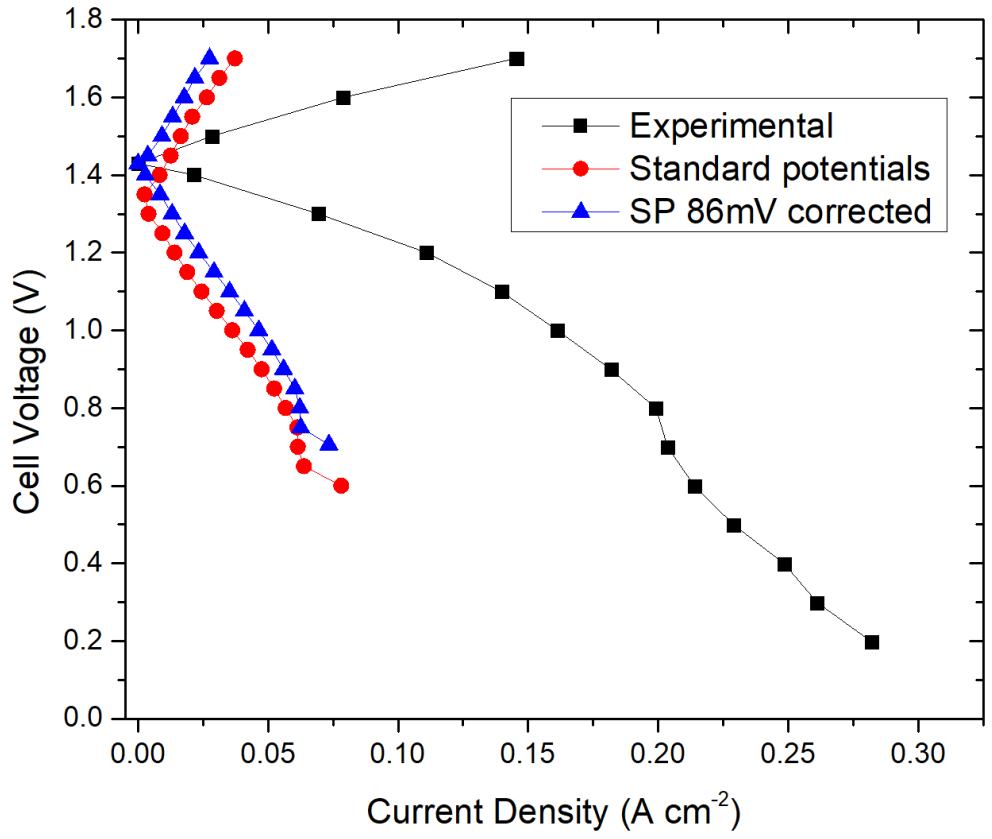


Figure 4.3 Experimentally measured and computationally predicted Polarization curves for 1 mm depth channel strip cell configuration at 50% SOC and 30 mL min⁻¹ flow rate.

Table 4.1 Geometric, material, and kinetic properties

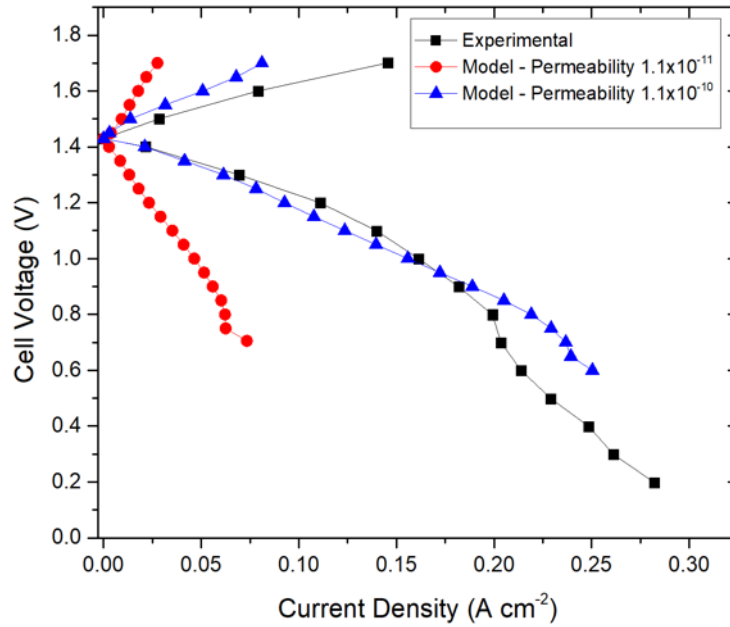
Parameter	Value	Reference
Channel, electrode, and membrane length (<i>mm</i>)	50	Chosen
Channel width/land (<i>mm</i>)	1	Chosen
Channel depth (<i>mm</i>)	1	Chosen
Electrode and membrane width (<i>mm</i>)	2	Chosen
Uncompressed electrode thickness (μm)	280	SGL [98]
Compressed electrode thickness (μm)	210	Chosen
Membrane thickness (μm)	183	[105]
Uncompressed electrode porosity (%)	89	SGL [98]
Compressed electrode porosity (%)	85	[99]
Uncompressed electrode permeability (m^2)	1.1×10^{-11}	SGL [98]
Positive electrode specific surface area ($m^2 m^{-3}$)	6.5×10^4	Measured
Negative electrode specific surface area ($m^2 m^{-3}$)	1.75×10^4	Measured
Positive electrode reaction rate constant ($m s^{-1}$)	5.7×10^{-6}	Measured
Negative electrode reaction rate constant ($m s^{-1}$)	5×10^{-7}	Measured
Electrode electronic conductivity ($S m^{-1}$)	450	SGL [98]
Membrane ionic conductivity ($S m^{-1}$)	10	[105]
Positive charge transfer coefficient (–)	0.55	[91]
Negative charge transfer coefficient (–)	0.45	[91]

Table 4.2 Electrolyte properties

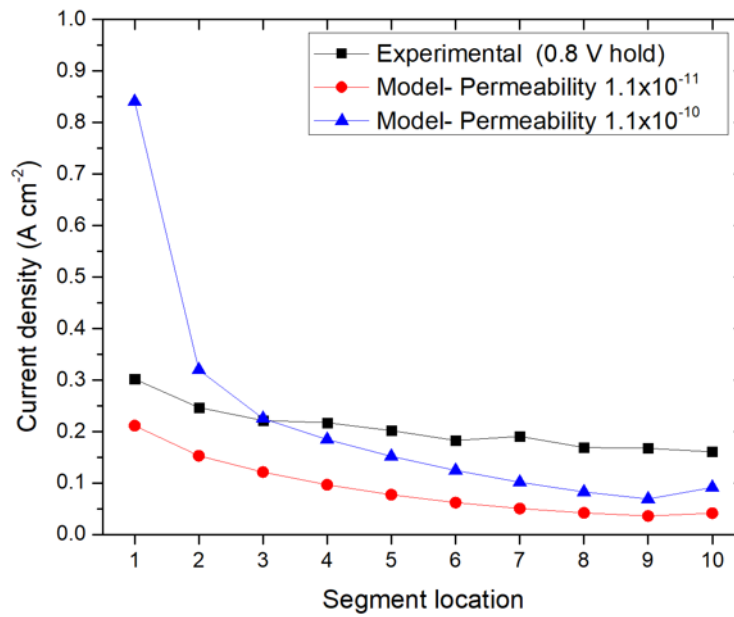
Parameter	Value	Reference
V(II) diffusion coefficient in the electrode ($m^2 s^{-1}$)	2.4×10^{-10}	[106]
V(III) diffusion coefficient in the electrode ($m^2 s^{-1}$)	2.4×10^{-10}	[106]
V(IV) diffusion coefficient in the electrode ($m^2 s^{-1}$)	3.9×10^{-10}	[106]
V(V) diffusion coefficient in the electrode ($m^2 s^{-1}$)	3.9×10^{-10}	[106]
H+ diffusion coefficient in the electrode ($m^2 s^{-1}$)	9.3×10^{-9}	[106]
Vanadium species initial concentration ($mol m^{-3}$)	750	Chosen
Negative electrolyte initial proton concentration ($mol m^{-3}$)	4800	Chosen
Positive electrolyte initial proton concentration ($mol m^{-3}$)	4050	Chosen
Electrolyte conductivity ($S m^{-1}$)	66.7	[91]
Negative electrolyte density ($kg m^{-3}$)	1300	Measured
Positive electrolyte density ($kg m^{-3}$)	1350	Measured
Negative electrolyte dynamic viscosity ($Pa s$)	0.0025	Measured
Positive electrolyte dynamic viscosity ($Pa s$)	0.005	Measured

Figure 4.4 shows electrode permeability parameter impact on the predicted polarization curve and current distribution. As seen in the Figure 4.4a, experimentally measured polarization curve is roughly predicted by fitting permeability parameter. The fitted permeability value here is order of magnitude higher than the manufacturer value. However, it has been reported in the literature that the permeability is inversely proportional to electrode compression [107]. Considering both negative and positive electrodes are compressed during cell assembly (approximately 25%), increase of permeability under compression is unphysical. In-situ current distribution measurement also supports this. As shown in Figure 4.4b, experimentally measured current distribution strongly disagrees with the computationally predicted current distribution. Model predicts very high currents at the inlet segments and relatively lower current densities at the outlet segments. Unrealistically high permeability allows large volume of electrolyte to penetrate into the electrode. As a result of this, high electrochemical performance is seen at the inlet region. Consuming vanadium active species very rapidly at the inlet region induces drastic concentration drop towards the outlet. These results indicate that permeability is a very influential parameter for VRFB model, and its exact value needs to be determined under compression. It is also found that the polarization curve analysis itself is not effective for verifying numerical results.

Diffusion coefficient of the vanadium active species is another influential mass transport parameter investigated in this study. Vanadium active species' diffusivities (Table 4.2) are experimentally measured by Yamamura et al. [106]. These values are broadly accepted in VRFB literature. However, VRFB model developed in this work



(a)



(b)

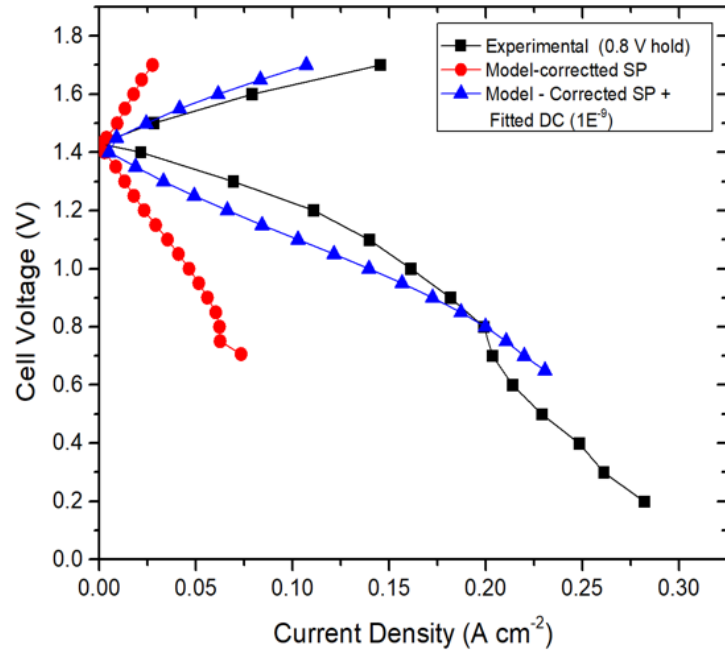
Figure 4.4 Electrode permeability parameter impact on computationally predicted (a) Polarization curves and (b) current distributions for 1 mm depth channel strip cell configuration at 50% SOC and 30 mL min⁻¹ flow rate.

predicts vanadium active species diffusion coefficients approximately order of magnitude higher than the literature. As seen in Figure 4.5 the model with fitted diffusion coefficients moderately well predicts both polarization curve and current distribution measurements. The Figure 4.5a shows that the model slightly underpredicts measured current densities for charging branch and most of the points for discharging branch on the polarization curve. It is observed that the model starts to overpredict measured current densities after the 0.8 V voltage. At the 0.8 V, predicted current density and measured current density is almost identical. Thus, experimentally measured and computationally predicted current density distributions are compared at the 0.8 V in Figure 4.5b. Current density distribution predictions from the fitted model show good agreement with the experimental data. While the maximum error (14%) is seen at the segment #1, average error for the rest of the segments is less than 10%.

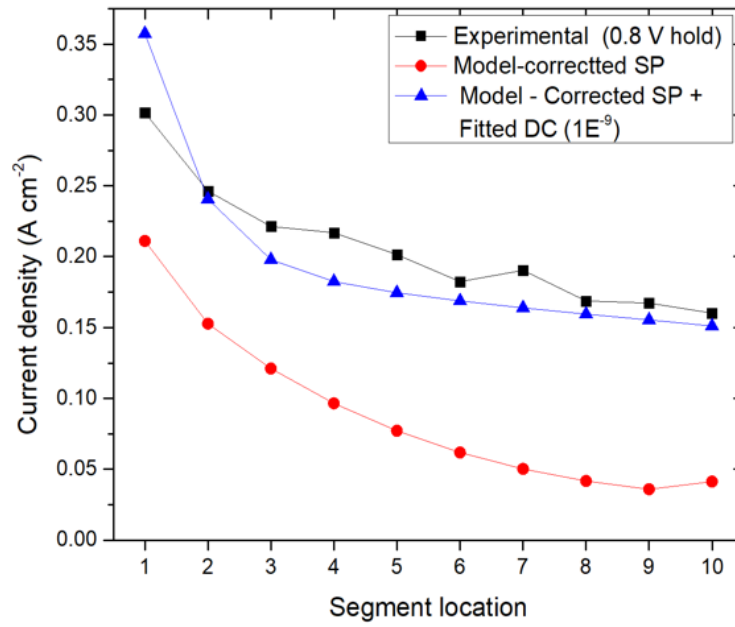
Among the input parameters tested, diffusion coefficient parameter is the only parameter, verified by the current distribution measurement. In-situ current distribution measurements are very powerful and unique technique to validate VRFB model, is employed in this study for the first time in VRFB literature. Therefore, it is speculated that the vanadium active species' diffusion coefficients could be higher than the literature around order of magnitude.

4.4 Conclusions

In this work, three-dimensional multiphysics model incorporating first-principle conservation equations and electrochemical kinetics is introduced. The computational



(a)



(b)

Figure 4.5 Diffusion coefficient of vanadium active species' impact on computationally predicted (a) Polarization curves and (b) current distributions for 1 mm depth channel strip cell configuration at 50% SOC and $30\ mL\ min^{-1}$ flow rate.

domain is created based on the strip cell architecture. Open circuit voltage, polarization curve and in-situ current distribution measurements are employed to validate computational results. Among wide range of parameters electrode permeability and the diffusion coefficient of vanadium active species are found to be the most influential mass transport parameters affecting electrochemical performance and distribution. The experimental measurements are successfully predicted fitting the diffusion coefficient of the vanadium active species. It is postulated that the diffusivity values for vanadium species could be ten times higher than the values reported in VRFB literature. Although the fitting permeability roughly predicts polarization curve, large discrepancy is obtained between the predicted current distribution and the measured values. It is concluded that the electrode compression should be considered to determine the effective permeability of the electrode.

Chapter 5 In-plane Liquid Electrolyte Permeability of Porous Electrode in Vanadium Flow Battery

Abstract

This chapter was presented at the 239th Electrochemical Society Digital Meeting in 2021.

The full paper will be submitted for publication under the same authorship below.

Ertugrul, T. Y., Daugherty, M., Aaron, D., Ekici K., and Mench, M. M. “**In-plane Liquid Electrolyte Permeability of Porous Electrode in Vanadium Flow Battery**” *ECS Meeting Abstracts* (2021)

My contribution to this work was collection, reduction, and analysis of data as well as composition of the manuscript. Daugherty assisted with building the algorithm. Ekici introduced the LBM technique. Aaron and Mench assisted in analysis of data and composition of the manuscript.

5.1 Introduction

Electrode permeability is an important mass transport parameter and is defined as the ability of the electrode to allow fluid transport. The permeability parameter is reported by the manufacturer for uncompressed carbon paper electrode (39AA) [98]. However, during VRFB cell assembly, the electrode is compressed and its morphological properties change under compression. In general, VRFB electrode is compressed 20-30% of nominal thickness to minimize contact resistances between electrode-channel and electrode-membrane interfaces. Therefore, electrode compression should be considered to evaluate effective permeability. In this study, both experimental and computational approaches are employed to determine in-plane liquid electrolyte permeability of porous electrodes in vanadium redox flow battery.

5.2 Materials and methods

5.2.1 Lattice Boltzmann model (LBM)

A three-dimensional single-relaxation-time (SRT) LBM is employed (utilizing the Palabos library written in C++) to simulate the liquid electrolyte in the porous electrode [108]. Pressure-driven flow in porous media is achieved by imposing a constant pressure at the inlet and a constant, lower pressure at the outlet. A computational domain (up to 300 x 300 x 300 lattice unit) created within Python (Porespy module) [109] consists of randomly-generated fibers, having uniform diameter (4, 6, 8, 10 lattice unit) to simulate the carbon paper electrode pore structure as seen in Figure 5.1. Porosity of the unit structure is achieved by controlling the number of fibers in the domain. Figure 5.2 shows Randomly-generated carbon paper macropore structures with different porosities. Permeability parameters are calculated for generated pore structures as functions of the electrode porosity.

Rather than using the Navier-Stokes equations, LB method uses the Boltzmann transport equation, which is

$$\frac{\partial f}{\partial t} + e \cdot \nabla f = \Omega(x, t) \quad (5.1)$$

where $f(x, t)$ is the particle distribution function, e is the particle velocity, and $\Omega(f)$ is the collision operator. Boltzmann equation is discretized in time, space, and velocity to get Lattice Boltzmann equation.

$$f_i(x + e_i \Delta t, t + \Delta t) = f_i(x, t) + \Omega(x, t) \quad (5.2)$$

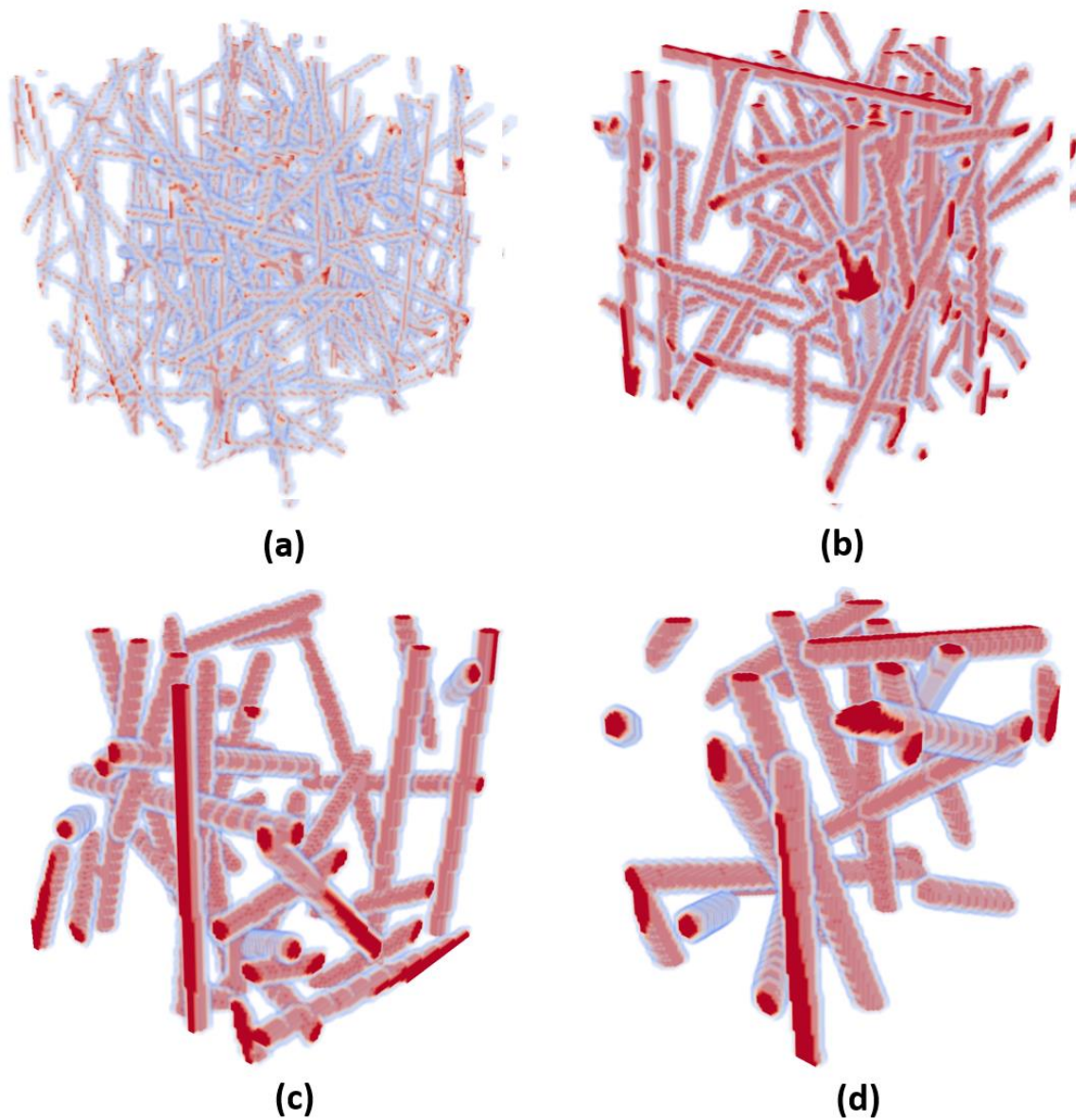


Figure 5.1 Carbon paper electrode macropore structure artificially generated in Python (a) $r = 2$ lu, Number of cylinders = 188, (b) $r = 3$ lu, Number of cylinders = 76, (c) $r = 4$ lu, Number of cylinders = 39, (d) $r = 5$ lu, Number of cylinders = 27

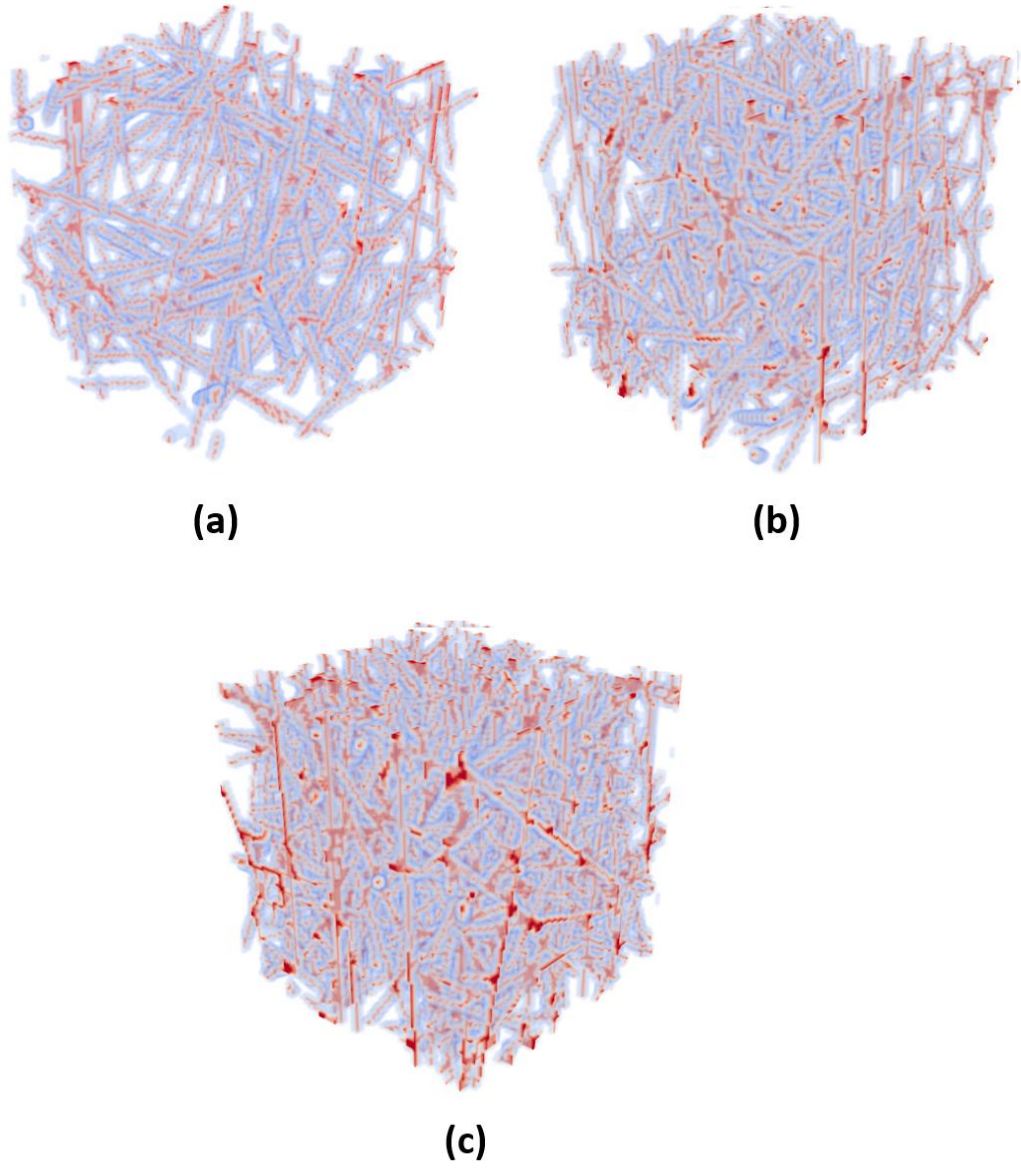


Figure 5.2 Randomly-generated carbon paper macropore structures with different porosities (a) 89% porosity, (b) 82.7 % porosity, (c) 69.7 % porosity.

This equation expresses that the particle $f_i(x, t)$ in the i_{th} direction moves with e_i velocity to next lattice point $x + e_i\Delta t$ in time step Δt . Among collision operators, single-relaxation time Bhatnagar-Gross-Krook (BGK) is the simplest operator which can be used for Navier-Stokes equation.

$$\Omega(x, t) = - \frac{[f_i(x, t) - f_i^{eq}(x, t)]}{\tau} \quad (5.3)$$

Thus, the Lattice Boltzmann equation is obtained as

$$f_i(x + e_i\Delta t, t + \Delta t) - f_i(x, t) = - \frac{[f_i(x, t) - f_i^{eq}(x, t)]}{\tau} \quad (5.4)$$

where f_i^{eq} is the equilibrium distribution, τ is the relaxation time. While the right side of the equation represents the collision (relaxation) step, the left side of the equation represents the streaming (propagation) step, The equilibrium distribution is defined as

$$f_i^{eq}(x, t) = w_i\rho(x) \left[1 + \frac{e_i \cdot u}{c^2} + \frac{(e_i \cdot u)^2}{2c^4} - \frac{u^2}{2c^2} \right] \quad (5.5)$$

where w_i is the weighting factor, c is the lattice speed of sound, which is usually $\frac{1}{\sqrt{3}}$. The three-dimensional cubic lattice is discretized using eighteen particle velocity directions (D3Q19) as seen in Figure 5.2. The discrete velocities and weighting factors for D3Q19 are given as

$$e_i = \begin{cases} (0,0,0); & a = 0 \\ (\pm 1,0,0), (0, \pm 1,0), (0,0, \pm 1); & i = 1,2, \dots, 6 \\ (\pm 1, \pm 1,0), (\pm 1,0, \pm 1), (0, \pm 1, \pm 1); & i = 7,8, \dots, 18 \end{cases} \quad (5.6)$$

$$w_i = \begin{cases} \frac{1}{3}, & i = 0; \\ \frac{1}{18}, & i = 1, 2, \dots, 6; \\ \frac{1}{36}, & i = 7, 8, \dots, 18; \end{cases} \quad (5.7)$$

To recover conservation of mass and momentum equation (Navier-Stokes'), macroscopic density and velocity of the electrolyte are defined by Chapman-Enskog expansion as

$$\rho(x, t) = \sum_{i=0}^{N=18} f_i(x, t) \quad (5.8)$$

$$u(x, t) = \frac{1}{\rho} \sum_{i=0}^{N=18} e_i f_i(x, t) \quad (5.9)$$

Electrolyte viscosity and the pressure are also defined as

$$\nu = c^2 \left(\tau - \frac{1}{2} \right) \frac{\Delta x^2}{\Delta t} \quad (5.10)$$

$$P = c^2 \rho \quad (5.11)$$

5.2.2 In-plane permeability experimental setup

The sample electrode was placed between two plates as shown in Figure 5.3a. The end plates were secured by eight bolts to a torque of 10 N-m each to ensure uniform compression and tight sealing. Various electrode thicknesses were tested using an incompressible PTFE gasket. The electrode thickness during compression was converted to porosity employing Eq. 5.12 [99].

$$\phi^{eff} = 1 - \frac{1 - \phi}{1 - \delta} \quad (5.12)$$

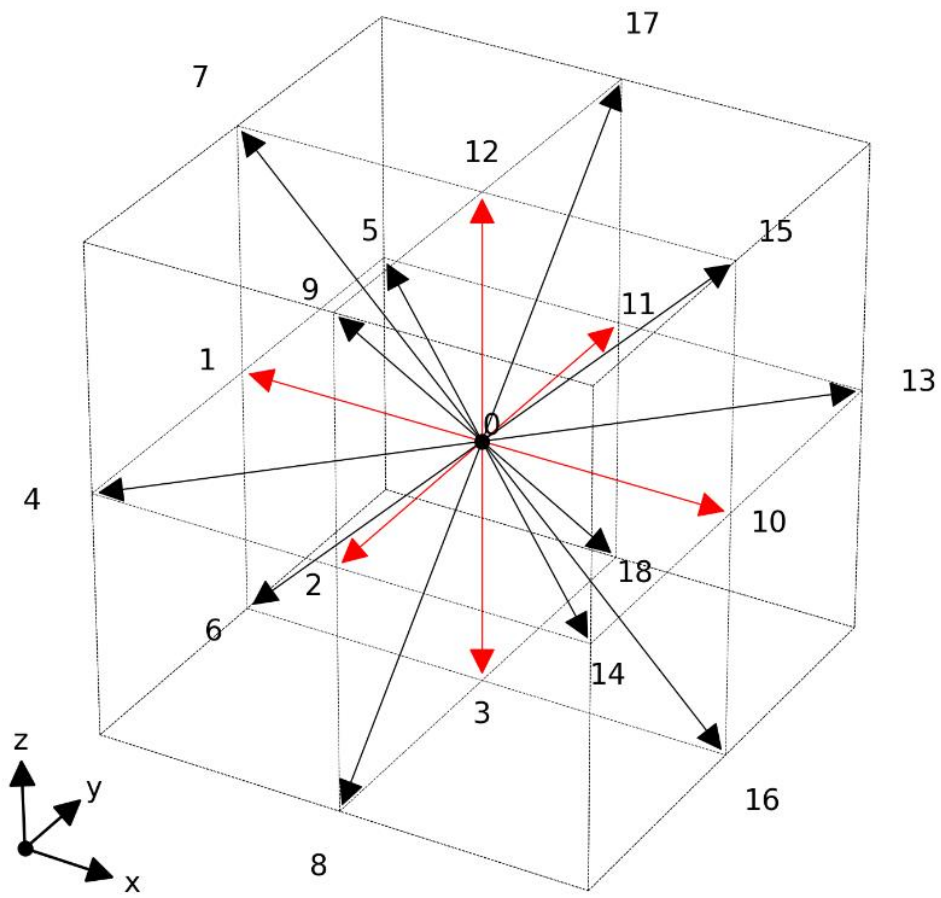


Figure 5.3 D3Q19 x, y, and z velocity components.

$$\delta = \frac{t - t^*}{t}$$

where ϕ is the uncompressed porosity, ϕ^{eff} is the effective compressed porosity, δ is the fractional strain, t is the uncompressed thickness, and t^* is the compressed thickness. Effective porosities as a function of electrode thicknesses are tabulated in Table 5.1. The inlet pressure was measured via pressure transducer (Omega Engineering Inc, 0-50 psi, $\pm 0.25\%$ accuracy, Norwalk, CT, USA) for a range of flow rates from 10 mL min^{-1} up to 50 mL min^{-1} at each electrode thickness. The permeability was then calculated using Darcy's law (Eq. 5.13) for incompressible fluid flow.

$$-\frac{dP}{dx} = \frac{\mu}{k} v \quad (5.13)$$

where P is the pressure, x is the position coordinate, μ is the viscosity, k is the permeability, and v is the velocity of the electrolyte. Electrode microstructure images (Figure 5.4) were taken and fiber diameters were measured using a digital microscope (VHX-6000, Keyence, Tokyo). Carbon paper electrode fiber diameters were measured to be in the range of $7 - 9 \mu\text{m}$ as seen in Figure 5.5. An average of $8 \mu\text{m}$ was chosen for carbon paper fiber diameter. Lattice permeabilities were converted to physical permeability based on the ratio between physical fiber diameter and lattice unit cylinder diameter. This conversion is defined by the Eq.5.14.

$$K_{physical} = K_{lattice\ unit} \left(\frac{D_{physical}}{D_{lattice\ unit}} \right)^2 [m^2] \quad (5.14)$$

Table 5.1 Electrode thicknesses during compression and corresponding porosities

Electrode thickness (μm)	Compression ratio (%)	Calculated porosity
279.4	0	0.89
254	9	0.879
228.6	18.1	0.8656
203.2	27.2	0.8488
177.8	36.3	0.8271
152.4	45.4	0.7983
127	54.5	0.758
101.6	63.6	0.6975

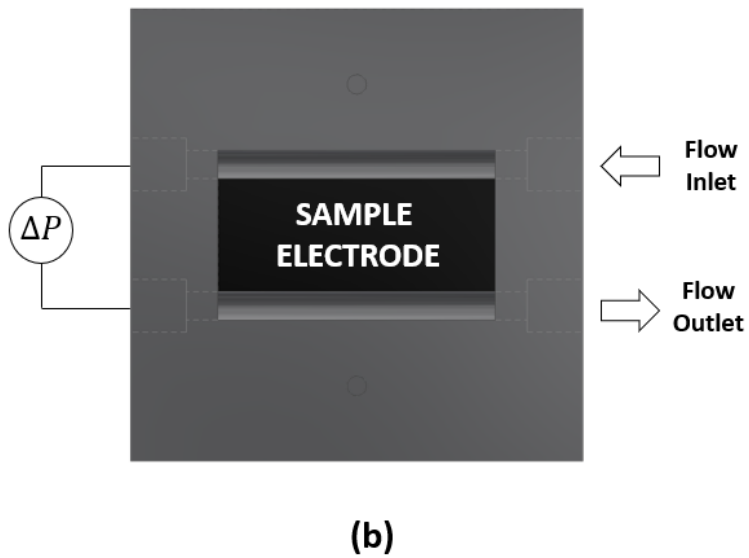
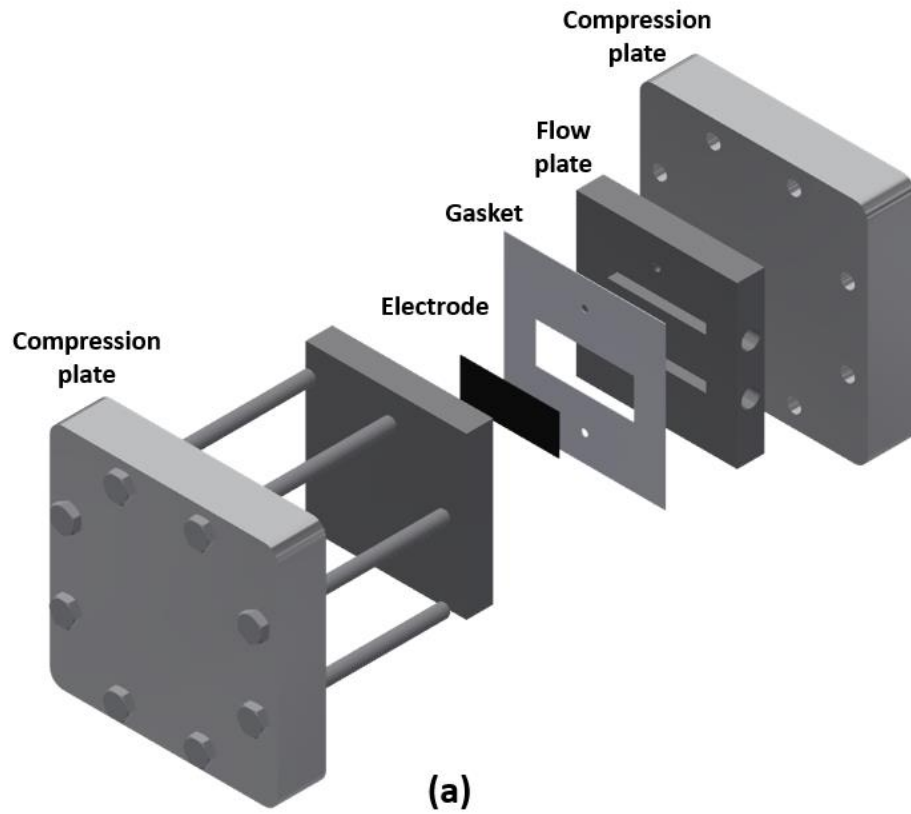


Figure 5.4 Exploded view of in-plane permeability measurement experimental setup.

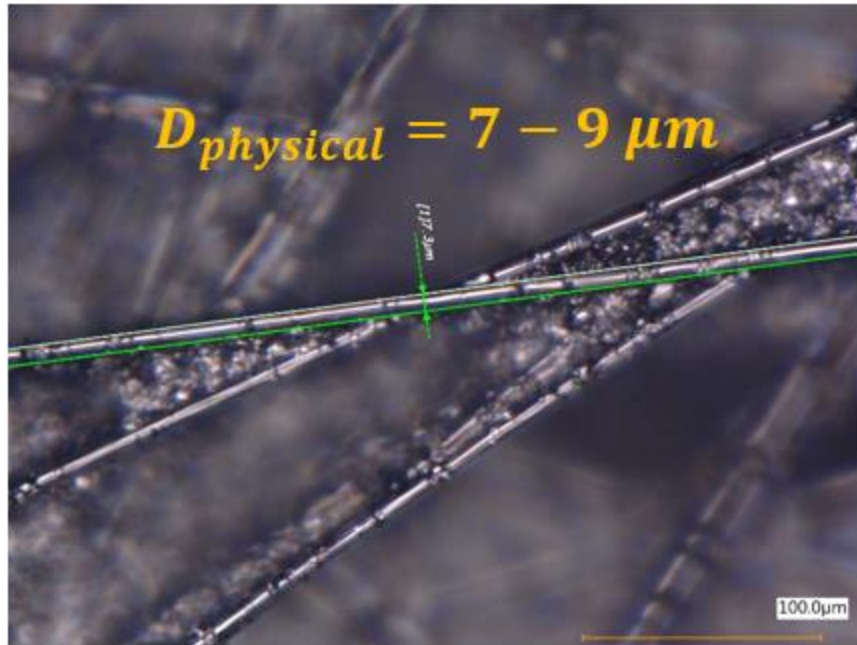


Figure 5.5 An image of carbon paper electrode macropore structure under optical microscope

5.3 Results and discussion

Experimental measurements were carried out employing the permeability cell experimental setup shown in Figure 5.4. The idea behind this setup is based on determining hydraulic losses as a function of electrode compression to determine permeability. Figure 5.6 shows pressure drop per length as a function of porosity for the electrolyte flow rate from 10 to 50 mL min⁻¹. Since pressure drop data show a linear relationship with flow rate for all porosities, 1D Darcy's equation for incompressible flow is fitted to experimental data to calculate electrode effective permeability.

Initial simulations were performed for four different fiber radii ($r = 2, 3, 4,$ and 5 lattice unit) for the same domain resolution $100 \times 100 \times 100$ lattice unit. Figure 5.7 compares experimentally-measured and computationally-predicted permeabilities for various porosities (0.89, 0.879, 0.8656, 0.8488, 0.8271, 0.7983, 0.758, 0.6975) and fiber radii. Experimental measurements show that the permeability is directly proportional to the porosity as expected [107]. The LB model successfully predicted experimental measurements for low porosities (0.758, 0.6975), the electrodes under $> 50\%$ compression. However, as porosity increased ($< 50\%$ compression), computationally-predicted permeabilities deviated from experimentally measured. Results were consistently similar for all fiber radii. It is also seen from the Figure 5.7 that the computational simulations were performed ten times, generating ten different random domains for each porosity. Due to the randomness of the generated computational domain, there is some variability in calculated permeabilities. Variability tended to increase as fiber radius increased. This behavior is attributed to insufficient computational domain resolution.

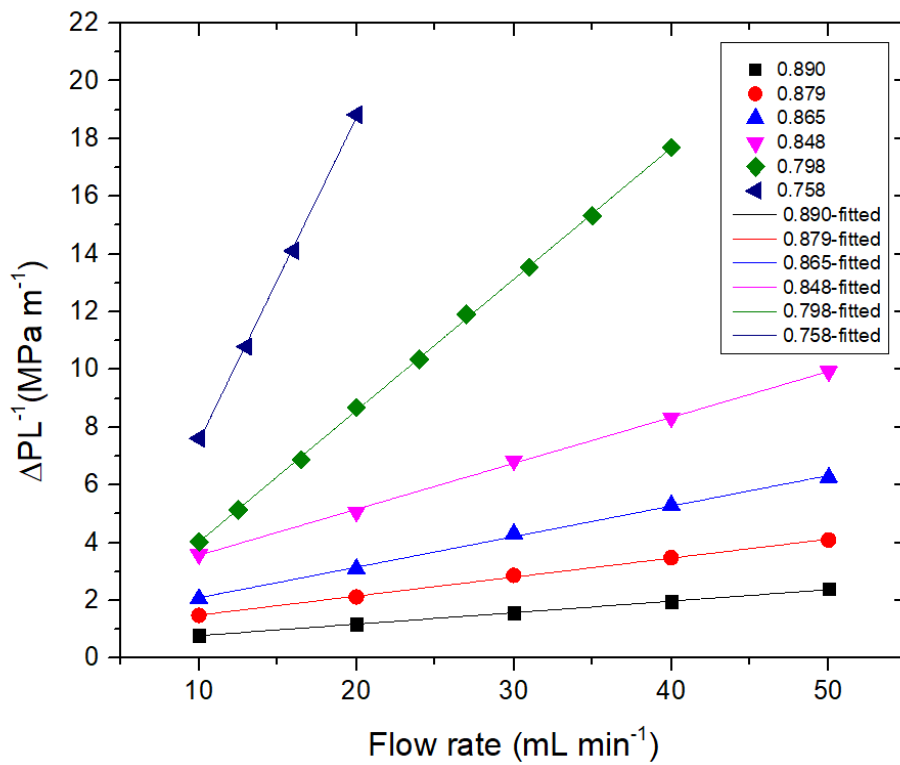


Figure 5.6 Pressure drop per length as a function of flow rate for various carbon paper electrode porosities showing experimental data and fitting using the Darcy's equation.

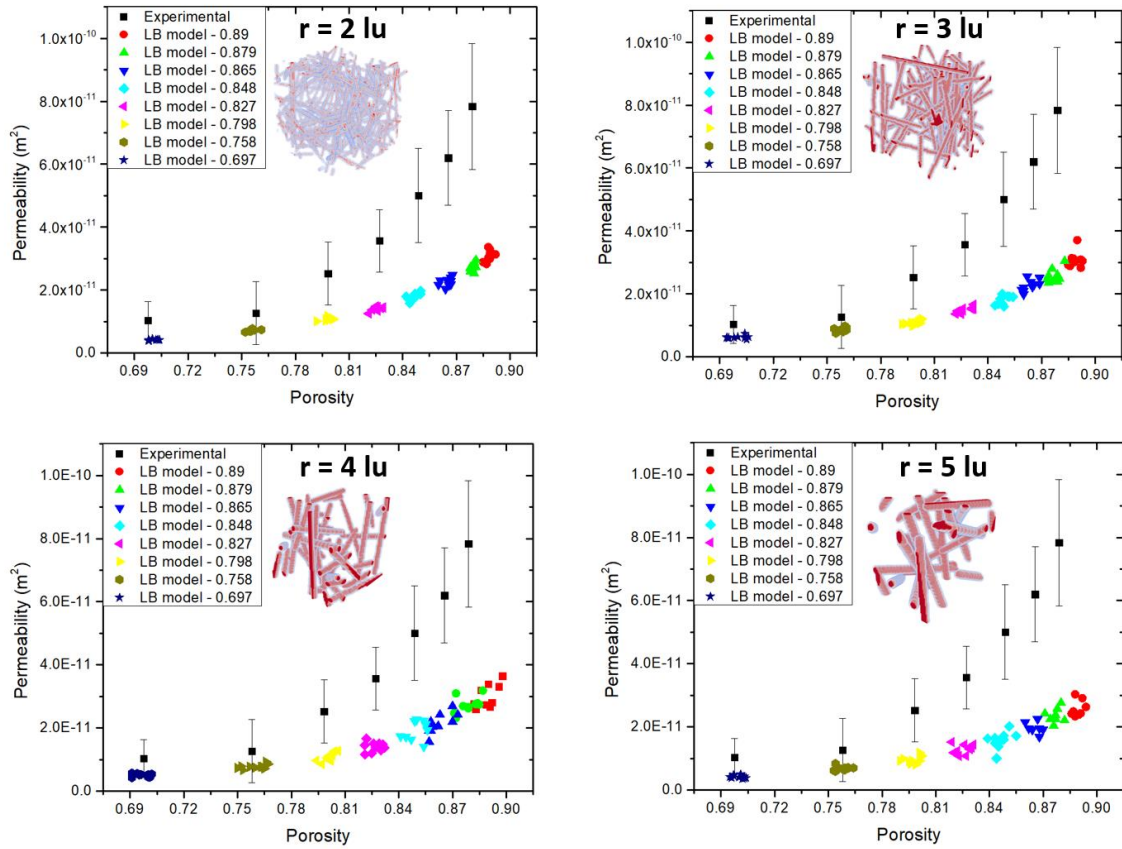


Figure 5.7 Experimentally measured permeabilities vs. Computationally predicted permeabilities as a function porosity for various fiber radiuses.

The impact of computational domain resolution on the predicted permeabilities is shown in Figure 5.8. While the domain resolution was varied, fiber radius was kept constant at two lattice unit for these simulations. As seen, increasing domain resolution noticeably reduced variability in predicted permeabilities. For the 300x300x300 lattice unit domain resolution, almost no variability was achieved. However, increasing resolution significantly increased the computational costs. Exponential growth in simulation time was observed once the resolution was tripled. Considering the computational cost and variability in results, the 200x200x200 lattice unit domain resolution provides sufficient accuracy with reasonable computation time. Although increased domain resolution provided better accuracy, the discrepancy between experimental measurements and computational predictions persisted. LB model still radically underpredicted experimentally-measured permeabilities for higher porosities. This is most likely due to the simulation domain not accurately representing the real arrangement of fibers. Simulating carbon paper electrode macropore structure via randomly generated cylinders may not be an accurate approach.

Figure 5.9a shows an image of carbon paper electrode macropore structure under digital microscope. As seen, it is composed of carbonized fibers and filler materials. Thus, modeling carbon paper electrode macropore structure must consider both the fibers and the filler material. Motivated by this observation, a composite domain simulating both carbon fiber and filler material was developed. Three different composite domains (70% fiber vs. 30% filler, 50% fiber vs. 50% filler, 30% fiber vs. 70% filler), shown in Figure 5.9, varying carbon fiber and filler material solid content were investigated. It should be noted that all

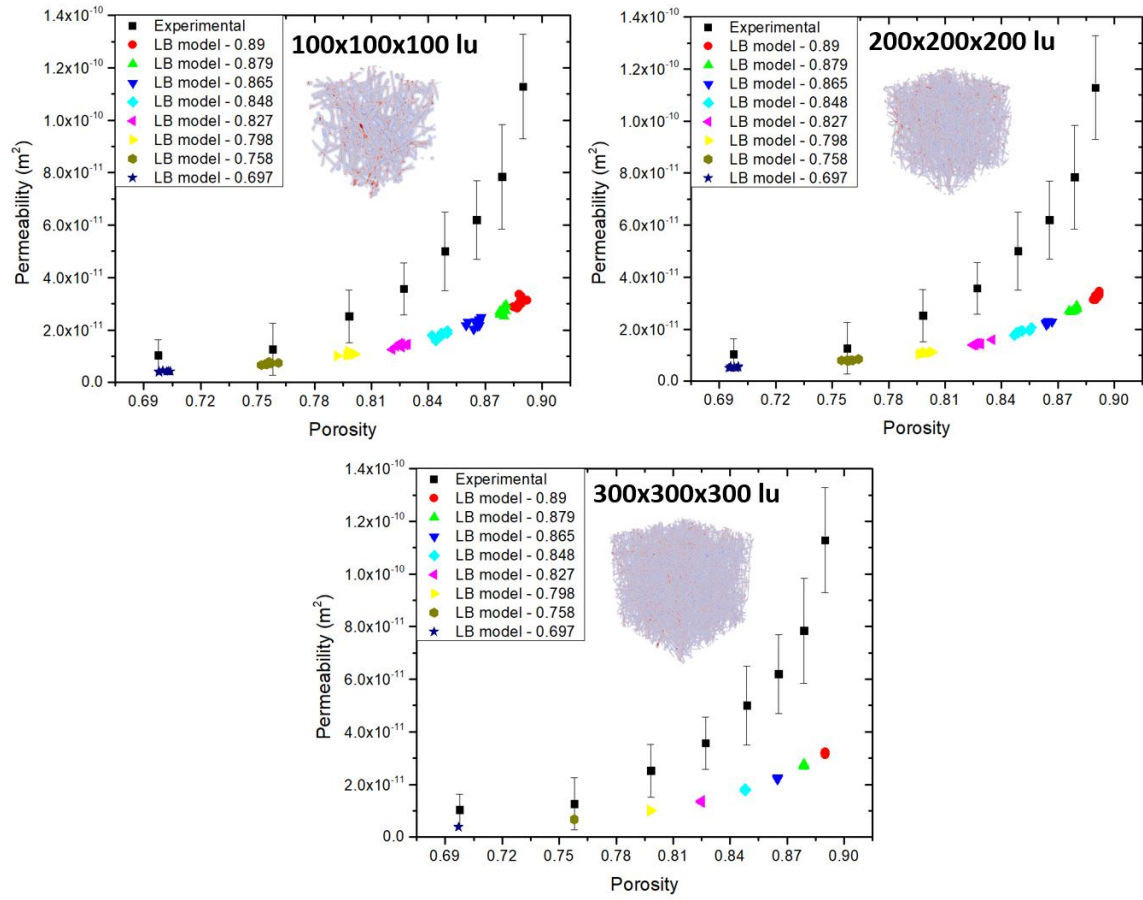
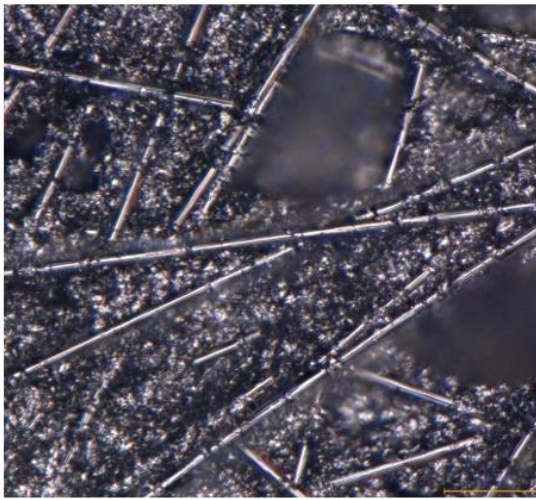
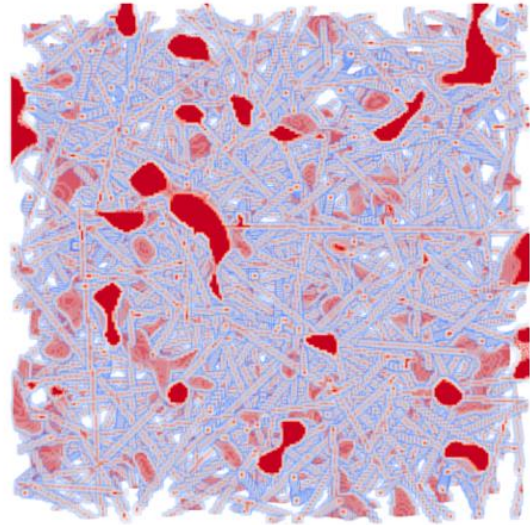


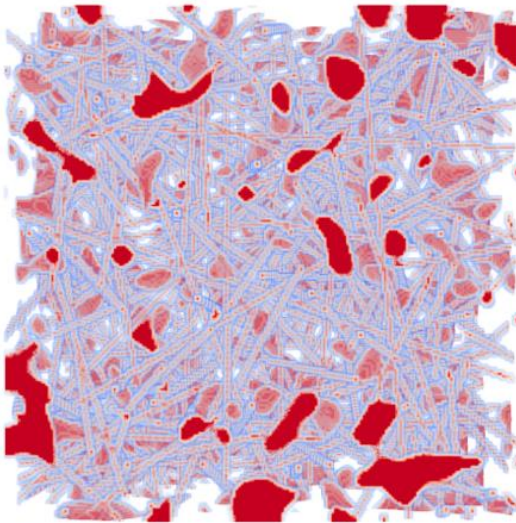
Figure 5.8 Experimentally measured permeabilities vs. Computationally predicted permeabilities as a function porosity for various lattice resolutions



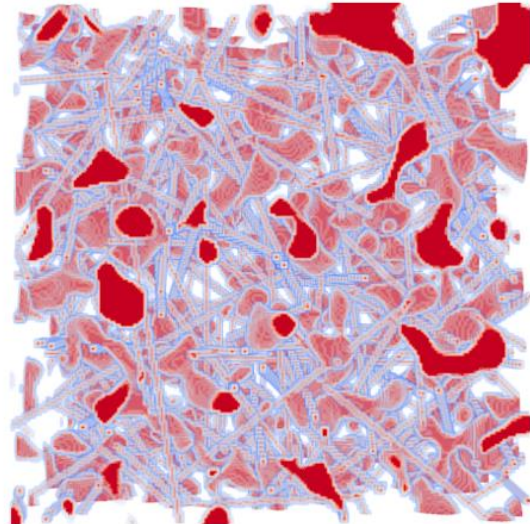
(a)



(b)



(c)



(d)

Figure 5.9 (a) An image of carbon paper electrode macropore structure under optical microscope and randomly generated composite domain (b) 70% fiber, 30% filler (c) 50% fiber, 50% filler (d) 30% fiber, 70% filler.

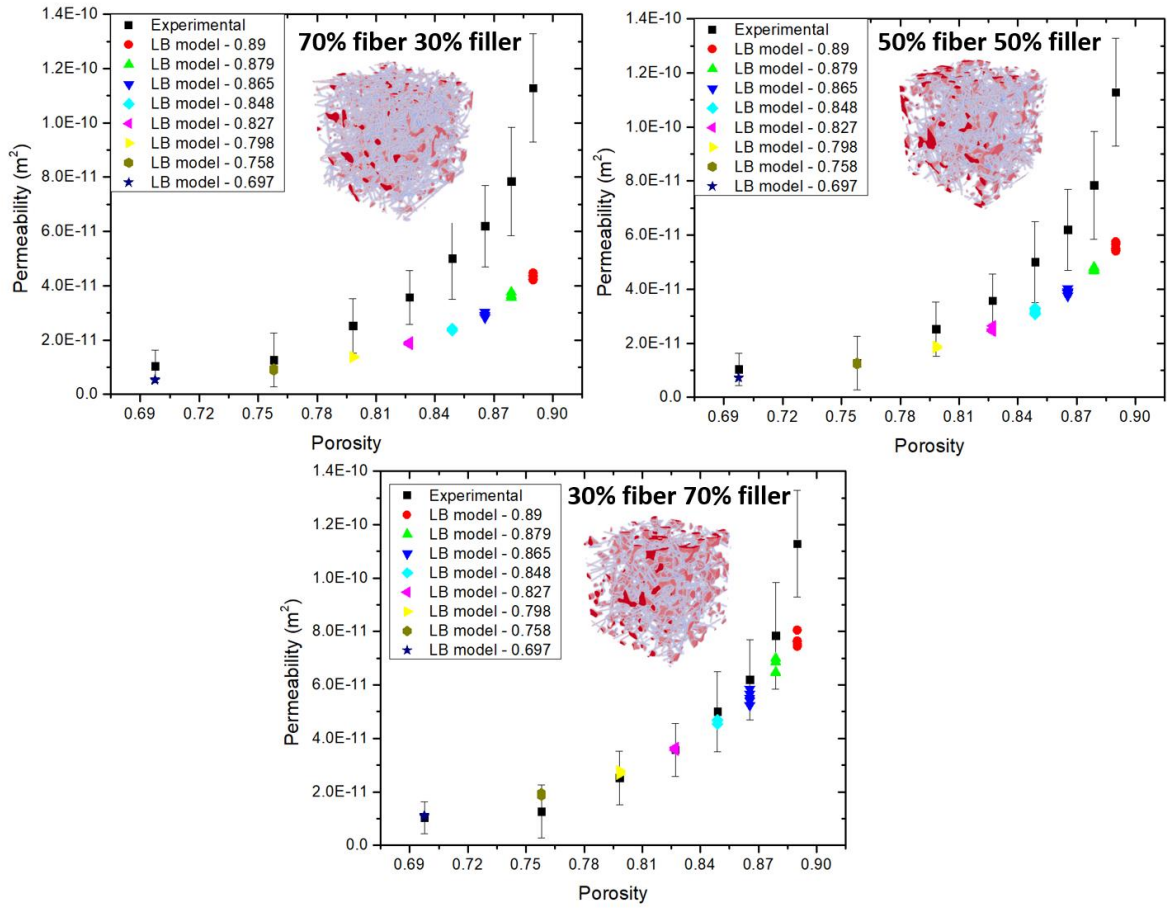


Figure 5.10 Experimentally measured permeabilities vs. Computationally predicted permeabilities as a function porosity for various composite domains.

these computational domains have the same porosity or volume of solid material; only the composition of the solid domain was varied. A domain resolution of 200x200x200 lattice units was chosen for these simulations due to the accuracy and computational cost.

Predicted permeabilities for composite domain are shown in Figure 5.10. Composite domain shows very promising results compared to the domain consisting only of fibers. The composite domain clearly simulates the carbon paper macropore structure more accurately. As the ratio of filler material solid content increased, model prediction approaches to the experimentally measured. It was found that 30% fiber and 70% filler material solid content ratio closely matched the composite domain, based on permeability measurement.

5.4 Conclusions

Electrode permeability is an important mass transport parameter affecting electrochemical performance and distribution in VRFBs. Its precise value is needed for mathematical modelling of realistic VRFB performance characterization and analysis under different operating conditions. In this study, electrode permeability as a function of electrode compression was investigated both experimentally and computationally. While the permeability cell experimental setup was designed to measure in-plane liquid electrolyte permeability of the electrode, LB method is employed to predict permeabilities for randomly-generated porous domain. It was demonstrated that the randomly-generated porous domain can simulate carbon paper electrode macropore structure. While the LB model considering only the fibers does not predict experimentally measured permeabilities for higher electrode porosities, composite domain considering both fibers and filler

materials successfully simulated carbon paper electrode macropore structure. Carbon paper electrode macropore structure also varies depending on the plane direction of the electrode. Experimental measurements reported in this work considers only transport in the in-plane direction. Permeability measurements on the through-plane direction should also be considered to validate LBM model predictions.

Chapter 6 Conclusion and recommendations

6.1 Conclusions

Vanadium redox flow batteries (VRFBs) are a promising candidate among grid-scale energy storage technologies. However, relatively low energy and power density compared to other electrochemical energy storage devices are significant obstacles for VRFB commercialization. At the cell level, mass transport losses are one of the major contributors to performance losses. Thus, investigating mass transport mechanisms in the porous electrode and determining related mass transport parameters is crucial to understanding pathways to achieve optimal performance and a higher depth of discharge for VRFBs. The VRFB porous electrode is a highly complex structure where electrochemical reactions and electroactive species transport occur simultaneously. Understanding these intricately connected phenomena requires advanced experimental measurement techniques and powerful multiscale numerical tools.

Several experimental techniques and numerical tools are employed in this work. Polarization curve analysis and in-situ current distribution measurements are implemented to investigate mass transport mechanisms, mainly reported in Chapters 2, 3 and 4. Chapter 3 includes CFD analysis along with in-situ current distribution results to investigate convection impacts on VRFB electrochemical performance and distribution. A multiphysics model incorporating polarization curve and current distribution measurements is utilized to investigate influential mass transport parameters, introduced in Chapter 4. Chapter 5 explains microscopic pore level modelling effort: Lattice Boltzmann method for investigating effective electrode permeability. The permeability cell

experimental setup is also introduced for measuring in-plane liquid electrolyte permeability of porous electrode in Chapter 5.

The main framework of this research is based on the strip cell architecture which has only one straight channel and 1 cm^2 active area. Unlike conventional flow field designs (e.g. parallel, interdigitated and serpentine) the strip cell is a simple architecture. Eliminating higher-dimensional behaviors (e.g. channel hopping, bypass at channel switchbacks, and potential fluid short circuits) provides relatively uniform electrolyte distribution both in the channel and electrode. All experimental measurements including polarization curves, pressure drops, and in-situ current distribution measurements are implemented on the strip cell architecture. Strip cell architecture is highly suitable for in-situ current distribution measurement. It is carefully machined to have electronically isolated, individual segments so that the distributed current can be evaluated along the channel. Cell level numerical simulations are also constructed based on the strip cell architecture. Modelling the strip cell is straightforward and computationally inexpensive. Because of that it is well-suited for comparative and detailed model validation studies.

Chapter 2 explores convection and diffusion mass transport mechanisms in the electrode and their impact on the electrochemical performance and distribution. While large current gradients from inlet to outlet are an indicator of concentration-driven mass transport, relatively uniform current distribution is a distinct characteristic of convection dominated mass transport in the electrode. Ultimately, electrochemical performance and distribution directly correlated to the velocity of convective flow in the electrode. This correlation is comprehensively discussed in Chapter 3.

The prominent finding in Chapter 3 is the direct correlation between electrolyte velocity in the electrode and the limiting current. However, there is no meaningful correlation is detected between the channel velocity and the limiting current. It is also found that there is a point where maximum achievable current cannot be improved due to the diffusion mass transport resistance between the liquid electrolyte and the electrode surfaces at the pore level. Considering this point, parasitic pumping losses can be optimized with enhanced convective flow in the electrode. Computational results have shown that the convective flow in the electrode is driven by the local pressure drop in the channel. The pressure drop arising due to any fluid path outside the channel-electrode region does not contribute to the current and must be minimized to improve overall system efficiency of the VRFB cell.

Chapter 4 introduces comprehensive cell level macroscopic model for VRFBs. A three-dimensional multiphysics model was constructed based on the strip cell architecture. It solves fundamental conservation equations (conservation of mass, momentum, species, charge) and Butler-Volmer electrochemical kinetics. Computational predictions are verified using open circuit voltage, polarization curve, and in-situ current distribution measurements. In-situ current distribution measurement is used to validate numerical prediction for the first time in the VRFB literature. Electrode permeability and diffusion coefficient of vanadium active species are found to be the most influential mass transport parameters. It is speculated that the vanadium active species' diffusion coefficients could be around order of magnitude higher than the literature. However, permeability parameter is

not verified by in-situ current distribution measurement. Motivated by this result, electrode permeability is comprehensively investigated in Chapter 5.

In Chapter 5, both experimental and numerical approaches (pore level modelling) are utilized to investigate electrode permeability as function of electrode porosity. The Lattice Boltzmann model is a powerful pore level numerical method employed to predict electrode permeability; a permeability cell experimental setup is designed to measure in-plane electrolyte permeability of porous electrode. Carbon paper electrode is simulated using randomly-generated porous domains. A solid domain composed only of randomly-oriented fibers did not enable accurate simulation of permeability compared to experimental measurements. However, a composite domain was formulated which more accurately represents the solid domain of carbon paper; this composite domain includes both solid fibers and solid filler material. The composite domain developed in this study successfully captures experimentally measured permeabilities.

6.2 Intellectual merit and broader impacts of the work

This work reports a significant advance in the fundamental understanding of mass transport mechanisms in the VRFB electrode. It is expected contribute to VRFB literature in multiple ways.

The strip cell architecture developed and fabricated in this work is a simple and novel design approach allows relatively uniform velocity distribution by suppressing complex flow behaviors in the VRFB cell. Thus, the effect of individual transport parameters is investigated more fundamentally than is present in the literature. This simple design approach is applicable not only for VRFBs, but also other redox flow battery (RFB)

chemistries and fuel cell technologies. Such an approach can enable deeper understanding in most flowing electrochemical systems.

The multiphysics model based on the strip cell architecture developed in this work is the most comprehensive (among published studies) cell level macroscopic model for VRFBs. It provides very detailed information including velocity, pressure, concentration, potential, and current distribution in the VRFB cell during operation. In addition, it is straightforward and computationally inexpensive due to the simple geometry. This computationally comprehensive but geometrically simple modelling approach is expected to serve as an effective numerical tool for the development and optimization of VRFB systems.

This research shows that model validation is critically important and polarization curve analysis alone is not effective for verifying numerical results. In-situ current distribution measurement is a powerful and unique technique employed in this research to verify numerical results for the first time in VRFB literature. This verification has led us to investigate and determine individual mass transport parameters in the electrode.

Key hydrodynamic relations (electrolyte velocity, pressure drop), both in the channel and electrode, reported in this work will provide guidance to improve convective flow in the electrode while suffering a comparatively moderate pressure drop penalty with better design. These findings are directly relevant to improving electrolyte utilization and overall system efficiency of the VRFB cell.

This work has also demonstrated that the electrode permeability and diffusion coefficient of the vanadium active species are highly influential mass transport parameters

in the VRFB electrode. Meticulously measured in-plane electrolyte permeability of the carbon paper porous electrode will provide benchmark data for VRFB literature.

6.3 Recommendations

The findings of this work shed light into many potential research avenues for further investigation. Following are recommendations that can be considered as viable extensions of this research.

The multiphysics model developed in this work can be further improved by including side reaction in the electrode and crossover in the membrane. Additionally, using concentrated solution theory, which includes interactions among all chemical species present in the solution, can better approximate transport phenomena in the VRFB electrode. There are also many electrochemical and transport parameters (e.g. electrochemical rate constant, surface area, charge transfer coefficient, conductivity, viscosity) impacting electrochemical performance and current distribution; these should be investigated for achieving more realistic VRFB simulations. Ultimately, the multiphysics model can be scaled up to evaluate more complex flow field designs for commercial VRFB cell applications. Employing this kind of comprehensive model would provide invaluable data to controlling and optimizing VRFB systems.

Although the LB model predictions and experimental measurements for permeability parameter show very good agreement, there is still some discrepancy for 89% porosity; this discrepancy may be alleviated with finer tuning of the composition and/or filler characteristics. In addition to that, the permeability cell experimental setup can be redesigned to measure through-plane liquid electrolyte permeability of a porous electrode

to consider uncertainties arising from anisotropic fiber arrangement. Three-dimensional, high resolution computed microtomography electrode images are also a potential research avenue for predicting permeability parameter via LB method. Depending on the employed resolution, CT scanned images can better represent porous electrode macropore structure than the randomly generated porous domain. This kind of study would be a very useful verification of fidelity of the randomly generated porous domains.

The liquid electrolyte viscosity impact on the electrochemical performance is negligibly small for the multiphysics model. However, the permeability is directly proportional to viscosity based on the Darcy equation. Due to this relationship, viscosity is also an important parameter that indirectly impacts electrochemical performance. The liquid electrolyte viscosity can be investigated under various conditions: state of charge (SOC), electrolyte concentration, and temperature for better approximation of the permeability parameter.

Future studies can also be extended to measure vanadium active species' diffusion coefficient. Bulk diffusion coefficient of the vanadium active species have already been reported in the VRFB literature. However, determining effective diffusivities for a porous electrode is highly challenging. Rotating disk electrode (RDE) voltammetry equipped with special design apparatus including porous electrode on the tip can help to overcome this challenge.

References

- [1] T.Y. Ertugrul, J.T. Clement, Y.A. Gandomi, D.S. Aaron, M.M. Mench, In-situ current distribution and mass transport analysis via strip cell architecture for a vanadium redox flow battery, *J. Power Sources*. 437 (2019) 226920. doi:10.1016/j.jpowsour.2019.226920.
- [2] T.Y. Ertugrul, M.C. Daugherty, J.R. Houser, D.S. Aaron, M.M. Mench, Computational and Experimental Study of Convection in a Vanadium Redox Flow Battery Strip Cell Architecture, *Energies*. 13 (2020) 4767. doi:10.3390/en13184767.
- [3] T.Y. Ertugrul, J.R. Houser, M.C. Daugherty, D.S. Aaron and M.M. Mench, Understanding the Interplay between Electrolyte Velocity Distribution and Current Distribution in Vanadium Flow Battery Electrode, in: ECS Meet. Abstr., The Electrochemical Society, 2019. doi:10.1149/ma2019-02/1/14.
- [4] T.Y. Ertugrul, J.T. Clement, Y.A. Gandomi, D. Aaron, Isolation of Mass Transport and Current Distribution in Vanadium Flow Batteries Via Segmented Strip Cell, ECS Meet. Abstr. (2019) 10–13. doi:10.1149/ma2019-01/3/437.
- [5] J. Novacheck, G. Brinkman, G. Porro, Operational Analysis of the Eastern Interconnection at Very High Renewable Penetrations, (2018).
- [6] U.S. Department of Energy, Grid Energy Storage Report, (2013) 67. [http://energy.gov/sites/prod/files/2014/09/f18/Grid Energy Storage December 2013.pdf](http://energy.gov/sites/prod/files/2014/09/f18/Grid_Energy_Storage_December_2013.pdf).
- [7] V. Viswanathan, A. Crawford, D. Stephenson, S. Kim, W. Wang, B. Li, G. Coffey, E. Thomsen, G. Graff, P. Balducci, M. Kintner-Meyer, V. Sprenkle, Cost and performance model for redox flow batteries, *J. Power Sources*. 247 (2014) 1040–1051. doi:10.1016/j.jpowsour.2012.12.023.
- [8] A. Crawford, V. Viswanathan, D. Stephenson, W. Wang, E. Thomsen, D. Reed, B. Li, P. Balducci, M. Kintner-Meyer, V. Sprenkle, Comparative analysis for various redox flow batteries chemistries using a cost performance model, *J. Power*

- Sources. 293 (2015) 388–399. doi:10.1016/j.jpowsour.2015.05.066.
- [9] S. Kim, E. Thomsen, G. Xia, Z. Nie, J. Bao, K. Recknagle, W. Wang, V. Viswanathan, Q. Luo, X. Wei, A. Crawford, G. Coffey, G. Maupin, V. Sprenkle, 1 kW/1 kWh advanced vanadium redox flow battery utilizing mixed acid electrolytes, *J. Power Sources*. 237 (2013) 300–309. doi:10.1016/j.jpowsour.2013.02.045.
- [10] S. Roe, C. Menictas, M. Skyllas-Kazacos, A High Energy Density Vanadium Redox Flow Battery with 3 M Vanadium Electrolyte, *J. Electrochem. Soc.* 163 (2016) A5023–A5028. doi:10.1149/2.0041601jes.
- [11] M. Skyllas-Kazacos, L. Cao, M. Kazacos, N. Kausar, A. Mousa, Vanadium Electrolyte Studies for the Vanadium Redox Battery—A Review, *ChemSusChem*. 9 (2016) 1521–1543. doi:10.1002/cssc.201600102.
- [12] C. Choi, S.S. Kim, R. Kim, Y. Choi, S.S. Kim, H. young Jung, J.H. Yang, H.T. Kim, A review of vanadium electrolytes for vanadium redox flow batteries, *Renew. Sustain. Energy Rev.* 69 (2017) 263–274. doi:10.1016/j.rser.2016.11.188.
- [13] Y. Ashraf Gandomi, D.S. Aaron, M.M. Mench, Coupled Membrane Transport Parameters for Ionic Species in All-Vanadium Redox Flow Batteries, *Electrochim. Acta*. 218 (2016) 174–190. doi:10.1016/j.electacta.2016.09.087.
- [14] Y. Ashraf Gandomi, D.S. Aaron, M.M. Mench, Influence of membrane equivalent weight and reinforcement on ionic species crossover in all-vanadium redox flow batteries, *Membranes (Basel)*. 7 (2017) 29. doi:10.3390/membranes7020029.
- [15] Y.A. Gandomi, D.S. Aaron, T.A. Zawodzinski, M.M. Mench, In situ potential distribution measurement and validated model for all-vanadium redox flow battery, *J. Electrochem. Soc.* 163 (2016) A5188–A5201. doi:10.1149/2.0211601jes.
- [16] E. Agar, K.W. Knehr, D. Chen, M.A. Hickner, E.C. Kumbur, Species transport mechanisms governing capacity loss in vanadium flow batteries: Comparing Nafion?? and sulfonated Radel membranes, *Electrochim. Acta*. 98 (2013) 66–74. doi:10.1016/j.electacta.2013.03.030.
- [17] E. Agar, Species Transport Mechanisms Governing Crossover and Capacity Loss

- in Vanadium Redox Flow Batteries A Thesis Submitted to the Faculty of requirements for the degree of, (2014).
- [18] K.W. Knehr, E. Agar, C.R. Dennison, A.R. Kalidindi, E.C. Kumbur, A transient vanadium flow battery model incorporating vanadium crossover and water transport through the membrane, *J. Electrochem. Soc.* 159 (2012) A1446–A1459. doi:10.1149/2.017209jes.
- [19] E. Agar, A. Benjamin, C.R. Dennison, D. Chen, M.A. Hickner, E.C. Kumbur, Reducing capacity fade in vanadium redox flow batteries by altering charging and discharging currents, *J. Power Sources.* 246 (2014) 767–774. doi:10.1016/j.jpowsour.2013.08.023.
- [20] E. Agar, K.W. Knehr, C.R. Dennison, E.C. Kumbur, Simulating Performance and Species Crossover in a Vanadium Redox Flow Battery using COMSOL Multiphysics Vanadium Redox Flow Battery, *Power.* (2011). www.mem.drexel.edu/energy.
- [21] D.K. Kim, S.J. Yoon, S. Kim, Transport phenomena associated with capacity loss of all-vanadium redox flow battery, *Int. J. Heat Mass Transf.* 148 (2020) 119040. doi:10.1016/j.ijheatmasstransfer.2019.119040.
- [22] A.M. Pezeshki, Z.J. Tang, C.C. Fujimoto, C.-N.N. Sun, M.M. Mench, T.A. Zawodzinski Jr., T.A. Zawodzinski, T.A. Zawodzinski Jr., T.A. Zawodzinski, Full Cell Study of Diels Alder Poly(phenylene) Anion and Cation Exchange Membranes in Vanadium Redox Flow Batteries, *J. Electrochem. Soc.* 163 (2015) A5154–A5162. doi:10.1149/2.0201601jes.
- [23] A.M. Pezeshki, J.T. Clement, G.M. Veith, T.A. Zawodzinski, M.M. Mench, High performance electrodes in vanadium redox flow batteries through oxygen-enriched thermal activation, *J. Power Sources.* 294 (2015) 333–338. doi:10.1016/j.jpowsour.2015.05.118.
- [24] A.M. Pezeshki, R.L. Sacci, G.M. Veith, T.A. Zawodzinski, M.M. Mench, The cell-in-series method: A technique for accelerated electrode degradation in redox flow batteries, *J. Electrochem. Soc.* 163 (2016) A5202–5210. doi:10.1149/2.0251601jes.
- [25] A.M. Pezeshki, R.L. Sacci, F.M. Delnick, D.S.D.S. Aaron, M.M. Mench,

- Elucidating effects of cell architecture, electrode material, and solution composition on overpotentials in redox flow batteries, *Electrochim. Acta.* 229 (2017) 261–270. doi:10.1016/j.electacta.2017.01.056.
- [26] J. Houser, J. Clement, A. Pezeshki, M.M. Mench, Influence of architecture and material properties on vanadium redox flow battery performance, *J. Power Sources.* 302 (2016) 369–377. doi:10.1016/j.jpowsour.2015.09.095.
- [27] J. Houser, A. Pezeshki, J.T. Clement, D. Aaron, M.M. Mench, Architecture for improved mass transport and system performance in redox flow batteries, *J. Power Sources.* 351 (2017) 96–105. doi:10.1016/j.jpowsour.2017.03.083.
- [28] I. Mayrhuber, C.R. Dennison, V. Kalra, E.C. Kumbur, Laser-perforated carbon paper electrodes for improved mass-transport in high power density vanadium redox flow batteries, *J. Power Sources.* 260 (2014) 251–258. doi:10.1016/j.jpowsour.2014.03.007.
- [29] D.S. Aaron, Q. Liu, Z. Tang, G.M. Grim, A.B. Papandrew, A. Turhan, T.A. Zawodzinski, M.M. Mench, Dramatic performance gains in vanadium redox flow batteries through modified cell architecture, *J. Power Sources.* 206 (2012) 450–453. doi:10.1016/j.jpowsour.2011.12.026.
- [30] F. Rahman, M. Skyllas-Kazacos, Solubility of vanadyl sulfate in concentrated sulfuric acid solutions, *J. Power Sources.* 72 (1998) 105–110. doi:10.1016/S0378-7753(97)02692-X.
- [31] X. Ma, H. Zhang, C. Sun, Y. Zou, T. Zhang, An optimal strategy of electrolyte flow rate for vanadium redox flow battery, *J. Power Sources.* 203 (2012) 153–158. doi:10.1016/j.jpowsour.2011.11.036.
- [32] A. Tang, J. Bao, M. Skyllas-Kazacos, Studies on pressure losses and flow rate optimization in vanadium redox flow battery, *J. Power Sources.* 248 (2014) 154–162. doi:10.1016/j.jpowsour.2013.09.071.
- [33] A. Khazaeli, A. Vatani, N. Tahouni, M.H. Panjeshahi, Numerical investigation and thermodynamic analysis of the effect of electrolyte flow rate on performance of all vanadium redox flow batteries, *J. Power Sources.* 293 (2015) 599–612. doi:10.1016/j.jpowsour.2015.05.100.

- [34] S. K??nig, M.R. Suriyah, T. Leibfried, Innovative model-based flow rate optimization for vanadium redox flow batteries, *J. Power Sources*. 333 (2016) 134–144. doi:10.1016/j.jpowsour.2016.09.147.
- [35] D.K. Kim, S.J. Yoon, J. Lee, S. Kim, Parametric study and flow rate optimization of all-vanadium redox flow batteries, *Appl. Energy*. 228 (2018) 891–901. doi:10.1016/j.apenergy.2018.06.094.
- [36] T. Wang, J. Fu, M. Zheng, Z. Yu, Dynamic control strategy for the electrolyte flow rate of vanadium redox flow batteries, *Appl. Energy*. 227 (2017) 613–623. doi:10.1016/j.apenergy.2017.07.065.
- [37] B. Akuzum, Y.C. Alparslan, N.C. Robinson, E. Agar, E.C. Kumbur, Obstructed flow field designs for improved performance in vanadium redox flow batteries, *J. Appl. Electrochem*. 49 (2019) 551–561. doi:10.1007/s10800-019-01306-1.
- [38] Q. Xu, T.S. Zhao, P.K. Leung, Numerical investigations of flow field designs for vanadium redox flow batteries, *Appl. Energy*. 105 (2013) 47–56. doi:10.1016/j.apenergy.2012.12.041.
- [39] R.M. Darling, M.L. Perry, The Influence of Electrode and Channel Configurations on Flow Battery Performance, *J. Electrochem. Soc*. 161 (2014) A1381–A1387. doi:10.1149/2.0941409jes.
- [40] T. Jyothi Latha, S. Jayanti, Hydrodynamic analysis of flow fields for redox flow battery applications Batteries, *J. Appl. Electrochem*. 44 (2014) 995–1006. doi:10.1007/s10800-014-0720-0.
- [41] X. Ke, J.I.D. Alexander, J.M. Prah, R.F. Savinell, Flow distribution and maximum current density studies in redox flow batteries with a single passage of the serpentine flow channel, *J. Power Sources*. 270 (2014) 646–657. doi:10.1016/j.jpowsour.2014.07.155.
- [42] E. Knudsen, P. Albertus, K.T.T. Cho, A.Z.Z. Weber, A. Kojic, Flow simulation and analysis of high-power flow batteries, *J. Power Sources*. 299 (2015) 617–628. doi:10.1016/j.jpowsour.2015.08.041.
- [43] K.M. Lisboa, J. Marschewski, N. Ebejer, P. Ruch, R.M. Cotta, B. Michel, D. Poulidakos, Mass transport enhancement in redox flow batteries with corrugated

- fluidic networks, *J. Power Sources*. 359 (2017) 322–331.
doi:10.1016/j.jpowsour.2017.05.038.
- [44] X. Ke, J.M. Prah, J.I.D. Alexander, R.F. Savinell, Redox flow batteries with serpentine flow fields: Distributions of electrolyte flow reactant penetration into the porous carbon electrodes and effects on performance, *J. Power Sources*. 384 (2018) 295–302. doi:10.1016/j.jpowsour.2018.03.001.
- [45] S. Maurya, P.T. Nguyen, Y.S. Kim, Q. Kang, R. Mukundan, Effect of flow field geometry on operating current density, capacity and performance of vanadium redox flow battery, *J. Power Sources*. 404 (2018) 20–27.
doi:10.1016/j.jpowsour.2018.09.093.
- [46] M. Al-Yasiri, J. Park, Study on channel geometry of all-vanadium redox flow batteries, *J. Electrochem. Soc.* 164 (2017) A1970–A1982.
doi:10.1149/2.0861709jes.
- [47] R. Gundlapalli, S. Jayanti, Performance characteristics of several variants of interdigitated flow fields for flow battery applications, *J. Power Sources*. 467 (2020) 228225. doi:10.1016/j.jpowsour.2020.228225.
- [48] C.R. Dennison, E. Agar, B. Akuzum, E.C. Kumbur, Enhancing Mass Transport in Redox Flow Batteries by Tailoring Flow Field and Electrode Design, *J. Electrochem. Soc.* 163 (2015) A5163–A5169. doi:10.1149/2.0231601jes.
- [49] M.D.R. Kok, A. Khalifa, J.T. Gostick, Multiphysics Simulation of the Flow Battery Cathode: Cell Architecture and Electrode Optimization, *J. Electrochem. Soc.* 163 (2016) A1408–A1419. doi:10.1149/2.1281607jes.
- [50] W. Chen, J. Kang, Optimization of electrolyte flow and vanadium ions conversion by utilizing variable porosity electrodes in vanadium redox flow batteries, *Chem. Phys.* 529 (2020) 110577. doi:10.1016/j.chemphys.2019.110577.
- [51] S. Tsushima, T. Suzuki, Modeling and Simulation of Vanadium Redox Flow Battery with Interdigitated Flow Field for Optimizing Electrode Architecture, *J. Electrochem. Soc.* 167 (2020) 020553. doi:10.1149/1945-7111/ab6dd0.
- [52] C.H. Lin, Y. De Zhuang, D.G. Tsai, H.J. Wei, T.Y. Liu, Performance enhancement of vanadium redox flow battery by treated carbon felt electrodes of

- polyacrylonitrile using atmospheric pressure plasma, *Polymers (Basel)*. 12 (2020). doi:10.3390/polym12061372.
- [53] L.C. Pérez, L. Brandão, J.M. Sousa, A. Mendes, Segmented polymer electrolyte membrane fuel cells-A review, *Renew. Sustain. Energy Rev.* 15 (2011) 169–185. doi:10.1016/j.rser.2010.08.024.
- [54] J.T. Clement, D.S. Aaron, M.M. Mench, In Situ Localized Current Distribution Measurements in All-Vanadium Redox Flow Batteries, *J. Electrochem. Soc.* 163 (2016) A5220–A5228. doi:10.1149/2.029305jes.
- [55] M.M. Mench, C.Y. Wang, An in situ method for determination of current distribution in PEM fuel cells applied to a direct methanol fuel cell, *J. Electrochem. Soc.* 150 (2003). doi:10.1149/1.1526108.
- [56] M. Noponen, T. Mennola, M. Mikkola, T. Hottinen, P. Lund, Measurement of current distribution in a free-breathing PEMFC, *J. Power Sources*. 106 (2002) 304–312. doi:10.1016/S0378-7753(01)01063-1.
- [57] W.-Y.Y. Hsieh, C.-H.H. Leu, C.-H.H. Wu, Y.-S.S. Chen, Measurement of local current density of all-vanadium redox flow batteries, *J. Power Sources*. 271 (2014) 245–251. doi:10.1016/j.jpowsour.2014.06.081.
- [58] M. Becker, N. Bredemeyer, N. Tenhumberg, T. Turek, Polarization curve measurements combined with potential probe sensing for determining current density distribution in vanadium redox-flow batteries, *J. Power Sources*. 307 (2016) 826–833. doi:10.1016/j.jpowsour.2016.01.011.
- [59] S.J.C. Cleghorn, C.R. Derouin, M.S. Wilson, S. Gottesfeld, A printed circuit board approach to measuring current distribution in a fuel cell, *J. Appl. Electrochem.* 28 (1998) 663–672. doi:10.1023/A:1003206513954.
- [60] J.J. Gagliardo, J.P. Owejan, T.A. Trabold, T.W. Tighe, Neutron radiography characterization of an operating proton exchange membrane fuel cell with localized current distribution measurements, *Nucl. Instruments Methods Phys. Res. Sect. A Accel. Spectrometers, Detect. Assoc. Equip.* 605 (2009) 115–118. doi:10.1016/j.nima.2009.01.145.
- [61] E.C.S. Transactions, T.E. Society, J.T. Clement, T.A. Zawodzinski, M.M. Mench,

- E.C.S. Transactions, T.E. Society, J.T. Clement, T.A. Zawodzinski, M.M. Mench, E.C.S. Transactions, T.E. Society, Measurement of Localized Current Distribution in a Vanadium Redox Flow Battery J. T. Clement, ECS Trans. 58 (2014) 9–16. doi:10.1149/05837.0009ecst.
- [62] R. Eckl, R. Grinzinger, W. Lehnert, Current distribution mapping in polymer electrolyte fuel cells—A finite element analysis of measurement uncertainty imposed by lateral currents, J. Power Sources. 154 (2006) 171–179. doi:10.1016/j.jpowsour.2005.04.004.
- [63] A.B. Geiger, R. Eckl, A. Wokaun, G.G. Scherer, An approach to measuring locally resolved currents in polymer electrolyte fuel cells, J. Electrochem. Soc. 151 (2004) A394. doi:10.1149/1.1646147.
- [64] Q. Zheng, X. Li, Y. Cheng, G. Ning, F. Xing, H. Zhang, Development and perspective in vanadium flow battery modeling, Appl. Energy. 132 (2014) 254–266. doi:10.1016/j.apenergy.2014.06.077.
- [65] G. Qiu, A.S. Joshi, C.R. Dennison, K.W. Knehr, E.C. Kumbur, Y. Sun, 3-D pore-scale resolved model for coupled species/charge/fluid transport in a vanadium redox flow battery, Electrochim. Acta. 64 (2012) 46–64. doi:10.1016/j.electacta.2011.12.065.
- [66] T. Kruger, The Lattice Method Boltzmann Principles and Practice, 2004.
- [67] Lattice Boltzmann Modeling, Sukop and Thorne (This book has content on Multi-phase Modeling, (n.d.).
- [68] M. Li, T. Hikiyara, A Coupled Dynamical Model of Redox Flow Battery Based on Chemical Reaction, Fluid Flow and Electrical Circuit, Inst. Electron. Inf. an Commun. Eng. E91 (2008) 1741–1747. doi:10.1093/ietfec/e91-a.7.1741.
- [69] A.A. Shah, M.J. Watt-Smith, F.C. Walsh, A dynamic performance model for redox-flow batteries involving soluble species, Electrochim. Acta. 53 (2008) 8087–8100. doi:10.1016/j.electacta.2008.05.067.
- [70] D. You, H. Zhang, J. Chen, A simple model for the vanadium redox battery, Electrochim. Acta. 54 (2009) 6827–6836. doi:10.1016/j.electacta.2009.06.086.
- [71] H. Al-Fetlawi, A.A. Shah, F.C. Walsh, Non-isothermal modelling of the all-

- vanadium redox flow battery, *Electrochim. Acta.* 55 (2009) 78–89.
doi:10.1016/j.electacta.2009.08.009.
- [72] A. Tang, S. Ting, J. Bao, M. Skyllas-Kazacos, Thermal modelling and simulation of the all-vanadium redox flow battery, *J. Power Sources.* 203 (2012) 165–176.
doi:10.1016/j.jpowsour.2011.11.079.
- [73] A. Tang, J. Bao, M. Skyllas-Kazacos, Thermal modelling of battery configuration and self-discharge reactions in vanadium redox flow battery, *J. Power Sources.* 216 (2012) 489–501. doi:10.1016/j.jpowsour.2012.06.052.
- [74] C.N. Sun, F.M. Delnick, L. Baggetto, G.M. Veith, T.A. Zawodzinski, Hydrogen evolution at the negative electrode of the all-vanadium redox flow batteries, *J. Power Sources.* 248 (2014) 560–564. doi:10.1016/j.jpowsour.2013.09.125.
- [75] H. Al-Fetlawi, A.A. Shah, F.C. Walsh, Modelling the effects of oxygen evolution in the all-vanadium redox flow battery, *Electrochim. Acta.* 55 (2010) 3192–3205.
doi:10.1016/j.electacta.2009.12.085.
- [76] X. Ma, H. Zhang, F. Xing, A three-dimensional model for negative half cell of the vanadium redox flow battery, *Electrochim. Acta.* 58 (2011) 238–246.
doi:10.1016/j.electacta.2011.09.042.
- [77] Y. Wang, S.C. Cho, Analysis and Three-Dimensional Modeling of Vanadium Flow Batteries, *J. Electrochem. Soc.* 161 (2014) A1200--A1212.
doi:10.1149/2.0061409jes.
- [78] Q. Zheng, H. Zhang, F. Xing, X. Ma, X. Li, G. Ning, A three-dimensional model for thermal analysis in a vanadium flow battery, *Appl. Energy.* 113 (2014) 1675–1685. doi:10.1016/j.apenergy.2013.09.021.
- [79] K. Oh, H. Yoo, J. Ko, S. Won, H. Ju, Three-dimensional, transient, nonisothermal model of all-vanadium redox flow batteries, *Energy.* 81 (2015) 3–14.
doi:10.1016/j.energy.2014.05.020.
- [80] K.W. Knehr, E.C. Kumbur, Open circuit voltage of vanadium redox flow batteries: Discrepancy between models and experiments, *Electrochem. Commun.* 13 (2011) 342–345. doi:10.1016/j.elecom.2011.01.020.
- [81] V. Yu, D. Chen, Dynamic Model of a Vanadium Redox Flow Battery for System

- Performance Control, *J. Sol. Energy Eng.* 136 (2013) 021005.
doi:10.1115/1.4024928.
- [82] R. Badrinarayanan, J. Zhao, K.J. Tseng, M. Skyllas-Kazacos, Extended dynamic model for ion diffusion in all-vanadium redox flow battery including the effects of temperature and bulk electrolyte transfer, *J. Power Sources.* 270 (2014) 576–586.
doi:10.1016/j.jpowsour.2014.07.128.
- [83] M. Vynnycky, Analysis of a model for the operation of a vanadium redox battery, *Energy.* 36 (2011) 2242–2256. doi:10.1016/j.energy.2010.03.060.
- [84] C.L. Chen, H.K. Yeoh, M.H. Chakrabarti, An enhancement to Vynnycky's model for the all-vanadium redox flow battery, *Electrochim. Acta.* 120 (2014) 167–179.
doi:10.1016/j.electacta.2013.12.074.
- [85] X. Ke, J.M. Prah, J.I.D. Alexander, R.F. Savinell, Mathematical Modeling of Electrolyte Flow in a Segment of Flow Channel over Porous Electrode Layered System in Vanadium Flow Battery with Flow Field Design, *Electrochim. Acta.* 223 (2017) 124–134. doi:10.1016/j.electacta.2016.12.017.
- [86] X. You, Q. Ye, P. Cheng, The dependence of mass transfer coefficient on the electrolyte velocity in carbon felt electrodes: determination and validation, *J. Electrochem. Soc.* 164 (2017) E3386–E3394. doi:10.1149/2.0401711jes.
- [87] R. Gundlapalli, S. Jayanti, Effect of electrolyte convection velocity in the electrode on the performance of vanadium redox flow battery cells with serpentine flow fields, 30 (2020). doi:10.1016/j.est.2020.101516.
- [88] N. Gurieff, D.F. Keogh, M. Baldry, V. Timchenko, D. Green, I. Koskinen, C. Menictas, Mass transport optimization for redox flow battery design, *Appl. Sci.* 10 (2020). doi:10.3390/APP10082801.
- [89] A.Z. Weber, M.M. Mench, J.P. Meyers, P.N. Ross, J.T. Gostick, Q. Liu, Redox flow batteries: A review, *J. Appl. Electrochem.* 41 (2011) 1137–1164.
doi:10.1007/s10800-011-0348-2.
- [90] J.M. Lamanna, S. Chakraborty, J.J. Gagliardo, M.M. Mench, Isolation of transport mechanisms in PEFCs using high resolution neutron imaging, *Int. J. Hydrogen Energy.* 39 (2014) 3387–3396. doi:10.1016/j.ijhydene.2013.12.021.

- [91] K.W. Knehr, E. Agar, C.R. Dennison, A.R. Kalidindi, E.C. Kumbur, A Transient Vanadium Flow Battery Model Incorporating Vanadium Crossover and Water Transport through the Membrane, *J. Electrochem. Soc.* 159 (2012) 1446–1459. doi:10.1149/2.017209jes.
- [92] K. Oh, S. Won, H. Ju, A comparative study of species migration and diffusion mechanisms in all-vanadium redox flow batteries, *Electrochim. Acta.* 181 (2015) 238–247. doi:10.1016/j.electacta.2015.03.012.
- [93] R.M. Darling, A.Z. Weber, M.C. Tucker, M.L. Perry, The influence of electric field on crossover in redox-flow batteries, *J. Electrochem. Soc.* 163 (2015) A5014–A5022. doi:10.1149/2.0031601jes.
- [94] J.D. Milshtein, K.M. Tenny, J.L. Barton, J. Drake, R.M. Darling, F.R. Brushett, Quantifying mass transfer rates in redox flow batteries, *J. Electrochem. Soc.* 164 (2017) E3265–E3275. doi:10.1149/2.0201711jes.
- [95] Q. Xu, T.S.S. Zhao, Determination of the mass-transport properties of vanadium ions through the porous electrodes of vanadium redox flow batteries, *Phys. Chem. Chem. Phys.* 15 (2013) 10841. doi:10.1039/c3cp51944a.
- [96] COMSOL Multiphysics® v. 5.4. www.comsol.com. COMSOL AB, Stockholm, Sweden., (2019).
- [97] D.A. Nield, A. Bejan, *Mechanics of Fluid Flow through a Porous Medium*. In: *Convection in Porous Media*, Springer, New York, NY, 2006. doi:https://doi.org/10.1007/0-387-33431-9_1.
- [98] R. Schweiss, C. Meiser, T. Damjanovic, I. Galbiati, N. Haak, WHITE PAPER SIGRACET® Gas Diffusion Layers for PEM Fuel Cells, Electrolyzers and Batteries, SGL Gr. (2016) 1–10.
- [99] M.M. Mench, *Fuel Cell Engines*, 2008. doi:10.1002/9780470209769.
- [100] G. Oriji, Y. Katayama, T. Miura, Investigation on V(IV)/V(V) species in a vanadium redox flow battery, *Electrochim. Acta.* 49 (2004) 3091–3095. doi:10.1016/j.electacta.2004.02.020.
- [101] S. Kumar, S. Jayanti, Effect of electrode intrusion on pressure drop and electrochemical performance of an all-vanadium redox flow battery, *J. Power*

- Sources. 360 (2017) 548–558. doi:10.1016/j.jpowsour.2017.06.045.
- [102] T.Y. Ertugrul, M. Daugherty, D. Aaron, M.M. Mench, Vanadium Flow Battery Electrochemistry and Fluid Dynamics Model with in-Situ Current Distribution Validation, ECS Meet. Abstr. MA2020-01 (2020) 473–473. doi:10.1149/ma2020-013473mtgabs.
- [103] T.Y. Ertugrul, J.T. Clement, Y.A. Gandomi, D.S. Aaron, M.M. Mench, In-situ current distribution and mass transport analysis via strip cell architecture for a vanadium redox flow battery, *J. Power Sources*. 437 (2019) 226920. doi:10.1016/j.jpowsour.2019.226920.
- [104] T. Yamamura, N. Watanabe, T. Yano, Y. Shiokawa, Electron-transfer kinetics of $\text{Np}^{3+}/\text{Np}^{4+}$, $\text{NpO}_2^{2+}/\text{NpO}_2^{2+}$, $\text{V}^{2+}/\text{V}^{3+}$, and $\text{VO}_2^{+}/\text{VO}_2^{+}$ at carbon electrodes, *J. Electrochem. Soc.* 152 (2005). doi:10.1149/1.1870794.
- [105] FuelCellStore, Nafion N115, N117, N1110, Catálogos. (2019) 1–3. www.fuelcellstore.com.
- [106] T. Yamamura, N. Watanabe, T. Yano, Y. Shiokawa, Electron-Transfer Kinetics of $\text{Np}^{3+}/\text{Np}^{4+}$, $\text{NpO}_2^{2+}/\text{NpO}_2^{2+}$, $\text{V}^{2+}/\text{V}^{3+}$, and $\text{VO}_2^{+}/\text{VO}_2^{+}$ at Carbon Electrodes, *J. Electrochem. Soc.* 152 (2005) A830. doi:10.1149/1.1870794.
- [107] J.T. Gostick, M.W. Fowler, M.D. Pritzker, M.A. Ioannidis, L.M. Behra, In-plane and through-plane gas permeability of carbon fiber electrode backing layers, *J. Power Sources*. 162 (2006) 228–238. doi:10.1016/j.jpowsour.2006.06.096.
- [108] J.L. and O.M. and D.K. and A.P. and D.L. and F.B. and M.B.B. and Y.T. and S.L. and S.L. and F.M. and J.L. and C.K. Chopard, Palabos: Parallel Lattice Boltzmann Solver, *Comput. Math. with Appl.* (2020). doi:<https://doi.org/10.1016/j.camwa.2020.03.022>.
- [109] J.R. Gostick J, Khan ZA, Tranter TG, Kok MDR, Agnaou M, Sadeghi MA, A Python Toolkit for Quantitative Analysis of Porous Media Images. *Journal of Open Source Software*, (2019). doi:10.5281/zenodo.2633284.

VITA

Tugrul Y. Ertugrul was born in Aksehir, Konya, Turkey. Tugrul received his Bachelor and Master of Science degrees in Mechanical Engineering from the Nigde Omer Halisdemir University. He was awarded a Scholarship by State of Turkish Republic and Sponsored by Ministry of Education of Turkey for Ph.D studies in the U.S. He attended the University of Tennessee, Knoxville to pursue his PhD in Mechanical Engineering under Dr. Matthew Mench's supervision in 2016. Tugrul is received his PhD degree as well as his second Master's and Computational Science minor degrees from the University of Tennessee in the Summer 2021.